UNIVERSITY OF SOUTHAMPTON

FACULTY OF NATURAL AND ENVIRONMENTAL SCIENCES

School of Ocean and Earth Science

Oceanographic conditions beneath Fimbul Ice Shelf, Antarctica

by

Einar Povl Abrahamsen

Thesis for the degree of Doctor of Philosophy

January 2012

UNIVERSITY OF SOUTHAMPTON

ABSTRACT

FACULTY OF NATURAL AND ENVIRONMENTAL SCIENCES
SCHOOL OF OCEAN AND EARTH SCIENCE

Doctor of Philosophy

OCEANOGRAPHIC CONDITIONS BENEATH FIMBUL ICE SHELF, ANTARCTICA

by Einar Povl Abrahamsen

Antarctic ice shelves play a key role in the global climate system, acting as important sites for the cooling of shelf waters, thereby facilitating deep and bottom water formation. Many of the processes that take place under large ice shelves can be observed more conveniently beneath smaller ice shelves such as Fimbul Ice Shelf, an ice shelf in the eastern Weddell Sea. Fimbul Ice Shelf and nearby ice shelves might also play a significant regional role: although no bottom water is produced in this area, it is thought that Fimbul Ice Shelf and nearby ice shelves precondition the shelf waters that ultimately are converted to Weddell Sea Deep Water (WSDW) in the southern Weddell Sea. Using the first data ever to be collected beneath an ice shelf from an autonomous underwater vehicle (AUV), as well as data from the vicinity of the ice shelf using traditional oceanographic methods, this thesis discusses the circulation and processes occurring beneath the ice shelf. This has been supplemented by using a coupled ice shelf/ocean model, POLAIR, to simulate the circulation, melting, and tides under Fimbul Ice Shelf and in the surrounding area. Data from the ice shelf cavity show relatively large variability in temperatures, but all within approx. 0.25 °C of the freezing point. Melt rates are found to be lower than some previous model studies, but in better agreement with observations and glaciological models. The base of the ice shelf was found to be rough in places, corresponding to ‘flow traces’ visible in satellite imagery. This could have implications for mixing beneath the ice shelf, at least in these limited areas. The Autosub AUV was found to be a useful platform for measuring hydrography and ice shelf cavity geometry with spatial coverage and resolution not available from surface measurements.

“Outside of a dog, a book is a man’s best friend. Inside a dog it’s too dark to read.”

—Groucho Marx

Contents

Abstract iii

Table of Contents vii

List of Figures ix

List of Tables xi

Declaration of Authorship xiii

Thesis insert xv

Acknowledgements xvii

Abbreviations xviii

Preface xxi

1 Introduction **1**
- 1.1 Ice shelves 3
- 1.2 The Antarctic Slope Front 6
- 1.3 What influences ice shelf–ocean interaction? 9
- 1.4 Measurements beneath various ice shelves 10
  - 1.4.1 Ross Ice Shelf 10
  - 1.4.2 Pine Island Glacier 10
  - 1.4.3 Ronne-Filchner Ice Shelf 11
- 1.5 Eastern Weddell ice shelves 12
- 1.6 Fimbul Ice Shelf 16
  - 1.6.1 Bathymetry 17
  - 1.6.2 Glaciology 17
- 1.7 Oceanography of the Eastern Weddell Sea 18

2 Jutulgryta **21**
- 2.1 Instruments and methods 22
  - 2.1.1 CTD casts 22
  - 2.1.2 IFIX mooring 23
- 2.2 Results 25

3 Observations from Fimbul Ice Shelf: JR097 31
3.1 Instruments and methods . . . 33
3.1.1 Shipborne CTD . . . 33
3.1.2 Autosub . . . 34
3.2 Water masses . . . 37
3.2.1 Shipborne CTD . . . 37
3.2.2 Autosub . . . 40
3.2.3 Discussion . . . 43
3.3 Currents and tides . . . 44
3.3.1 Tidal model . . . 44
3.3.2 ADCP measurements . . . 46
3.4 Water samples . . . 48
3.4.1 d18O data . . . 48
3.4.2 CFC samples . . . 48
3.5 Ice shelf base . . . 52
3.6 Mooring . . . 55

4 Modeling using POLAIR 59
4.1 Model description . . . 60
4.1.1 Coupler . . . 61
4.1.2 Atmosphere model . . . 61
4.1.3 Glacier (ice shelf) model . . . 62
4.1.4 Sea ice model . . . 63
4.1.5 Ocean model . . . 63
4.1.6 Domain/bathymetry . . . 66
4.1.7 Forcing . . . 67
4.1.8 Distribution of water masses across layers . . . 69
4.2 Model runs . . . 72
4.3 Modeling results . . . 72
4.3.1 LHS2006 forcing . . . 72
4.3.2 NCEP forcing . . . 74
4.3.3 Fluxes across 70° S and WDW fraction under ice . . . 84
4.3.4 Sensitivity to tides . . . 86
4.4 Modeling discussion . . . 87
4.4.1 What influences the melt rate? . . . 87
4.4.2 Level of "warm" water in cavity vs. reality . . . 90
4.4.3 Outflow pathways of ISW . . . 91
4.4.4 Is Fimbul Ice Shelf melting? . . . 92
4.5 Modeling conclusions . . . 95

5 Conclusions 97

A Bathymetry around and beneath Fimbul Ice Shelf 99

B Details of modeling work 103

References 111

List of Figures

1.1 Map of Antarctica with ice shelves indicated. 2
1.2 Diagram of idealized ice shelf 4
1.3 θ/S diagram from the southwestern Weddell Sea 5
1.4 Diagram of the Antarctic Slope Front 7
1.5 Historical WDW interface depths, plotted by year and month 8
1.6 Temperature data from Filchner Depression 12
1.7 MODIS satellite image of Fimbul Ice Shelf 14
1.8 Bathymetry beneath Fimbul Ice Shelf 15
1.9 Hydrographic section along $2^\circ\,40'\,$E 19

2.1 Diagram of sub-ice shelf mooring 22
2.2 CTD data from Jutulgryta 27
2.3 Mooring and CTD temperatures from Jutulgryta 28
2.4 Near-surface measurements at Jutulgryta 29

3.1 Map of CTD stations and ship track near Fimbul Ice Shelf 32
3.2 Schematic of Autosub-2 35
3.3 Map of CTD sections 37
3.4 Temperature and salinity sections from JR097 38
3.5 Hydrographic data from Autosub mission 382 42
3.6 θ/S diagram from CTD stations near Fimbul Ice Shelf 43
3.7 Tidal currents during mission 382 47
3.8 CFC concentrations along the Fimbul Ice Shelf ice front 49
3.9 Surface CFC saturations 51
3.10 Sub-ice shelf topography beneath Fimbul Ice Shelf from Autosub 53
3.11 Aster satellite image, with ice shelf drafts from Autosub superimposed . . 54
3.12 Mooring data near the main sill of Fimbul Ice Shelf 56
3.13 CTD data from the ‘yoyo’ stations near Fimbul Ice Shelf 58

4.1 Diagram of the POLAIR modeling system 61
4.2 Time stepping scheme used in the MICOM implementation in POLAIR. . 63
4.3 Map of the POLAIR model bathymetry 67
4.4 Density coordinates from POLAIR model runs 70
4.5 Distribution of layers in POLAIR model runs 71
4.6 Fraction of WDW under ice shelf in model runs 73
4.7 Annual cycle of sea surface salinity in POLAIR model 75
4.8 Monthly ice concentrations from the POLAIR model and climatology . . 77
4.9 Modeled fluxes across $70^\circ\,$S in POLAIR 78

4.10 Average monthly currents in POLAIR 79
4.11 Modeled melt rate maps from NCEP and LHS2006 runs 80
4.12 Month of minimum average mixed layer salinity, without tides enabled. . 83
4.13 Fractions of WDW beneath the ice shelf cavity 85
4.14 Modeled circulation beneath the ice shelf 87
4.15 Response of model to variations in wind forcing 91
4.16 Satellite image of Fimbul Ice Shelf, with ice fronts from 1997–2006 93

A.1 Bathymetry around Fimbul Ice Shelf from ship-borne multibeam sonar and Autosub 100

List of Tables

2.1 Instruments deployed at Jutulgryta 24

3.1 Misfits between measured and modeled tidal data 45
3.2 CFC saturations and ratios for water masses around Fimbul Ice Shelf . . 50

4.1 Basal melt rates from model runs 74

B.1 Parameters used in model runs 103
B.2 Density coordinates used in model runs 106
B.3 Numbering scheme for model runs 106
B.4 List of POLAIR model runs 107
B.5 Partial list of corrections, observations, and additions to the model code. . 108

Declaration of Authorship

I, Einar Povl Abrahamsen, declare that this thesis titled 'Oceanographic conditions beneath Fimbul Ice Shelf, Antarctica' and the work presented in it are my own and have been generated by me as the result of my own original research.
I confirm that:

1. This work was done wholly or mainly while in candidature for a research degree at this University;
2. Where any part of this thesis has previously been submitted for a degree or any other qualification at this University or any other institution, this has been clearly stated;
3. Where I have consulted the published work of others, this is always clearly attributed;
4. Where I have quoted from the work of others, the source is always given. With the exception of such quotations, this thesis is entirely my own work;
5. I have acknowledged all main sources of help;
6. Where the thesis is based on work done by myself jointly with others, I have made clear exactly what was done by others and what I have contributed myself;
7. Parts of this work have been published as:
    - Nicholls *et al.* (2006)
    - Nicholls *et al.* (2008)

Signed: ____________________________________

Date: ____________________________________

Graduate School of the National Oceanography Centre, Southampton

This PhD dissertation by
Einar Povl Abrahamsen
has been produced under the supervision of the following persons

Supervisors:

- Dr. Keith Nicholls (British Antarctic Survey)
- Dr. Kate Stansfield
- Prof. Harry L. Bryden

Chair of Advisory Panel:

- Prof. Andreas Oschlies (Oct. 2004–Oct. 2006)
- Prof. Ian S. Robinson (Nov. 2006 onward)

Acknowledgements

I would like to thank my supervisors, Keith Nicholls, Kate Stansfield, and Harry Bryden, for useful comments and discussions on this thesis, and for their support (and the occasional useful bit of nagging) during its preparation. The examiners, Ole Anders Nøst and Neil Wells, provided many helpful comments and suggestions that have greatly improved this thesis.

Svein Østerhus and Ole Anders Nøst kindly provided the data from Jutulgryta, as well as field notes and other useful information. In addition, Ole Anders Nøst provided his ice shelf and ocean cavity thickness measurements from Fimbul Ice Shelf. Thanks are due to all of the scientists, engineers, officers, and crew on JR097, especially the Autosub team, for their efforts on the cruise. Nick Hughes and Jeremy Wilkinson provided sea ice observations from the cruise, and Jeremy Wilkinson and Arthur Kaletzky helped extract and process the multi-beam data from Autosub. The CFC samples from the cruise were analyzed by Bill Smethie at Lamont-Doherty Earth Observatory, Columbia University. Angelika Humbert provided some of the remote sensing data used here, as well as helpful discussions on the glaciology of Fimbul Ice Shelf. Lars-Henrik Smedsrud kindly provided his model code and configuration files for using POLAIR on Fimbul Ice Shelf. Todd Arbetter, Paul Holland, and Malte Thoma were all instrumental to getting the model running at BAS, and provided useful input to the various modifications I made to the code. David Holland provided access to various computing clusters in New York before the HADES cluster was completed, and both he and Adrian Jenkins provided useful help with and information about the POLAIR model itself.

Finally, I'd like to thank everyone at BAS for their encouragement and support over the last seven years, as well as countless interesting — and occasionally useful — discussions during smoko. And I am indebted to Cambridge Canoe Club and the Huntingdonshire Philharmonic Society for helping to distract me from finishing this thesis for so long.

Abbreviations

ADCP	**A**coustic **D**oppler **C**urrent **P**rofiler
ADD	**A**ntarctic **D**igital **D**atabase
AUI	**A**utosub **U**nder **I**ce
AUV	**A**utonomous **U**nderwater **V**ehicle
AWI	**A**lfred-**W**egener-**I**nstitut für Polar- und Meeresforschung (Alfred Wegener Institute for Polar and Marine Research)
BAS	**B**ritish **A**ntarctic **S**urvey
CATS	**C**ircum-**A**ntarctic **T**idal **S**imulation
CDW	**C**ircumpolar **D**eep **W**ater
CFC	**C**hloro-**F**luoro-**C**arbon
CTD	**C**onductivity **T**emperature **D**epth
DSU	**D**ata **S**torage **U**nit
FRIS	**F**ilchner-**R**onne **I**ce **S**helf
FS-AU	**F**ull-**S**pectrum Chirp Processor for **AU**Vs
HSSW	**H**igh-**S**alinity **S**helf **W**ater
HYCOM	**HY**ybrid **C**oordinate **O**cean **M**odel
ISW	**I**ce **S**helf **W**ater
JR097	RRS **J**ames Clark **R**oss cruise no. 97
LADCP	**L**owered **A**coustic **D**oppler **C**urrent **P**rofiler
MAB	**M**eters **A**bove **B**ottom
MAMM	RADARSAT-1 **M**odified **A**ntarctic **M**apping **M**ission
ME	**M**eerestechnik **E**lektronik
MICOM	**M**iami **I**sopycnic **C**oordinate **O**cean **M**odel
MWDW	**M**odified **W**arm **D**eep **W**ater
NARE	**N**orwegian **A**ntarctic **R**esearch **E**xpedition
NCEP	**N**ational **C**enters for **E**nvironmental **P**rediction (part of NOAA)

OTIS	**O**regon **T**idal **I**nversion **S**ystem
PHINS	**Ph**otonic **I**nertial **N**avigation **S**ystem
PIG	**P**ine **I**sland **G**lacier
POLAIR	**P**olar **O**cean, **L**and, **A**tmosphere, and **I**ce **R**egional modeling system
PSU	**P**ractical **S**alinity **U**nit
RAMP	**R**ADARSAT-1 **A**ntarctic **M**apping **P**roject
RDI	**RD** **I**nstruments (now “Teledyne RDI”)
RIS	**R**oss **I**ce **S**helf
SAR	**S**ynthetic **A**perture **R**adar
SBE	**S**ea-**B**ird **E**lectronics, Inc.
TKE	**T**urbulent **K**inetic **E**nergy
UEA	**U**niversity of **E**ast **A**nglia
WDW	**W**arm **D**eep **W**ater
WLR	**W**ater **L**evel **R**ecorder
WSBW	**W**eddell **S**ea **B**ottom **W**ater
WSDW	**W**eddell **S**ea **D**eep **W**ater
WW	**W**inter **W**ater

Preface

This thesis is organized as follows: The motivation behind this thesis and some background to the oceanography of the eastern Weddell Sea and previous work in the region are provided in the introduction, Chapter 1. Then data from the Norwegian Antarctic Research Expedition 1990–1991 are presented in Chapter 2, and data from cruise JR097 to Fimbul Ice Shelf in 2005 are shown in Chapter 3. Modeling work using the POLAIR model is described in Chapter 4, and finally the conclusions are summarized in Chapter 5. A brief discussion of the bathymetry around and beneath Fimbul Ice Shelf is given in Appendix A, and details of the modeling work are provided in Appendix B.

Chapter 1

Introduction

This study originated from the OPRIS (Oceanographic conditions and processes beneath Ronne Ice Shelf) project, part of the Autosub Under Ice programme. The original aim of the project was to send the Autosub AUV beneath Filchner-Ronne Ice Shelf to measure hydrographic conditions there, in order to improve our understanding of the processes and circulation beneath the second-largest ice shelf — and arguably the most important for the formation of Antarctic Bottom Water (Orsi *et al.*, 1999). The main cruise of this project, JR097, took place in February–March 2005. Unfortunately sea ice conditions prevented the ship from reaching Filchner-Ronne Ice Shelf, so instead the cruise was held near Fimbul Ice Shelf, a smaller ice shelf farther to the east. While it is not as directly implicated in the production of AABW, this ice shelf plays a role in preconditioning the water that flows into the southern Weddell Sea (Fahrbach *et al.*, 1994), and has previously been estimated to have very high melt rates (Hellmer, 2004, Smedsrud *et al.*, 2006). However, there were very few measurements beneath the ice shelf: the Norwegian Antarctic Research Expeditions (NARE) visited the ice shelf in 1989/90 and 1991/92, and respectively deployed and recovered moored instruments from one location on the shelf (Orheim *et al.*, 1990, Østerhus and Orheim, 1994), but subsequently little was done with these data. In addition, Nøst (2004) measured the ice and water thicknesses during NARE 2000/01, so the geometry of the ice shelf cavity was relatively well-known (a distinct advantage when sending an AUV beneath the ice).

So while part of the reason for visiting this ice shelf was because of logistical constraints, there were several interesting questions to be answered, including estimating the melt rates beneath the ice shelf, and deducing the inflow and outflow areas and

Figure 1.1: Map of Antarctica; the ice shelves are shaded gray.

general circulation beneath the ice shelf. Using an AUV to sample beneath the ice shelf gives good spatial, but poor temporal coverage, complementing the previous (and more recent) use of moorings beneath the ice, which in turn give good temporal and poor spatial coverage. Even though the data presented here do provide interesting insights into the sub-ice shelf circulation, they are still very sparse, so a numerical model, which includes both good spatial and temporal coverage, was also used to help interpret features in the measurements. Knowing the circulation pattern beneath the ice shelf, and especially which water masses can access the ice shelf cavity and be modified there, is important for evaluating the effect of the ice shelf on the coastal current, which in turn influences the production of precursors of Antarctic Bottom Water.

1.1 Ice shelves

Ice shelves are the floating extensions of the Antarctic Ice Sheet. The map in Figure 1.1 shows an overview of Antarctica, with the most important ice shelves (and those discussed in this thesis) labeled. Ice shelves make up more than 10% of the “solid” surface of Antarctica, and occupy more than a third of the continental shelf (Domack, 2007). The processes that occur beneath some ice shelves play an important role in the creation of Antarctic Bottom Water, the water mass that occupies the bottom of a large part of the World Ocean (Orsi *et al.*, 1999).

The importance of ice shelves in the climate is twofold. Physically the ice shelves are thought to hold back the flow of ice streams into the ocean (Dupont and Alley, 2005). Thus, if ice shelves thin or disintegrate, the flow of glaciers and ice streams can increase, causing sea-level rise. Assuming that ice shelves themselves are in hydrostatic balance, the breakup of an ice shelf won’t in itself cause any direct rise in sea level, except through the steric effect. In addition, the water mass transformations that occur beneath ice shelves can, either directly or indirectly, contribute to the formation of bottom water around the margins of Antarctica. One of the most important sites is in the Weddell Sea, where the densest bottom water is formed (Orsi *et al.*, 1999). The ice shelves in the southern Weddell Sea, such as the Ronne-Filchner and perhaps the Larsen, produce Ice Shelf Water (ISW) that contributes toward the formation of Weddell Sea Bottom Water (WSBW). And the ice shelves upstream, in the eastern Weddell Sea, may play an important role in preconditioning the water that flows into the southern Weddell Sea (Fahrbach *et al.*, 1992).

We can roughly divide the environment of ice shelves into two categories, warm and cold. An example of a warm regime ice shelf is Pine Island Glacier, in the Amundsen Sea. Here, water significantly above the surface freezing point has access to the base of the ice shelf, causing melting everywhere beneath the ice shelf (e.g., Shepherd *et al.*, 2004). Thus, the net effect of the ice shelf is to cool and freshen the warm shelf waters, but without bringing them down to the freezing point to produce ISW. In contrast, beneath cold regime ice shelves shelf water is cooled to below the surface freezing point, possibly causing refreezing beneath the ice shelf when the meltwater rises such that its temperature decreases below the ambient freezing point (Nøst and Foldvik, 1994). This thesis will only discuss cold regime ice shelves, such as the Ronne-Filchner and Fimbul Ice Shelves.

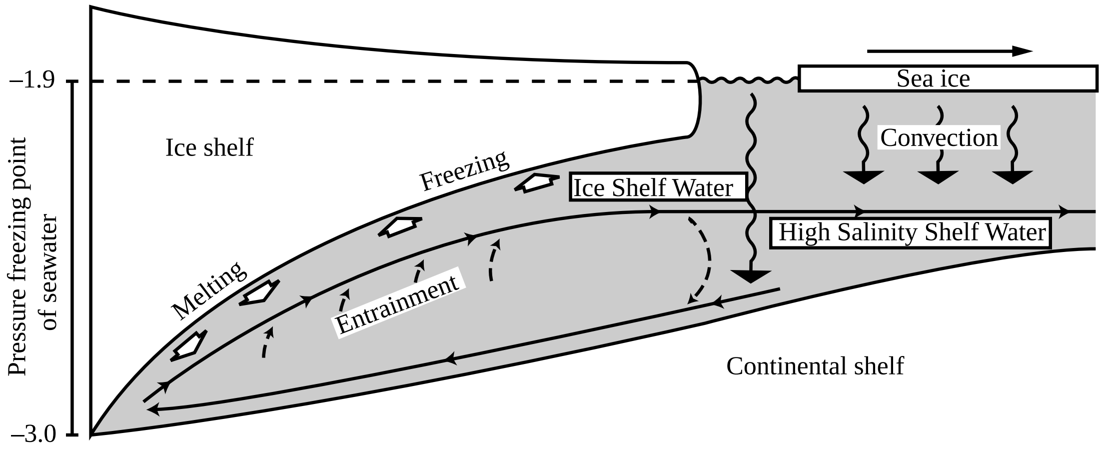

Figure 1.2: Schematic of an idealized ice shelf and continental shelf, with the processes that occur there (from Holland and Feltham, 2005).

Figure 1.2 shows the cross-section of an idealized cold ice shelf, with some of the processes that take place there. On the continental shelf, sea ice is moved offshore by predominantly offshore winds, creating a polynya where enhanced freezing and convection take place. The resulting High-Salinity Shelf Water (HSSW) accumulates on the shelf and flows beneath the ice, where the freezing point is depressed by the increased pressure. The magnitude of this depression is $7.53 \times 10^{-4}\,^\circ\mathrm{C}\,\mathrm{dbar}^{-1}$, so at a depth of 1500 m the freezing point is depressed to around $-3\,^\circ$C (Millero, 1978). This means that the water that was at the surface freezing point is now substantially warmer than the local freezing point, and melts ice off the base of the ice shelf.

As the water comes in contact with the ice, it is both cooled and freshened, causing a transformation that is approximately linear in T/S space (see Section 1.3). Turbulence at the ice–ocean boundary causes mixing, which counteracts the formation of a stable boundary layer that otherwise would form when the water is freshened by the ice. The boundary layer is locally buoyant and will rise until it reaches the point where the local freezing point is the same as its temperature. At this point the water becomes supercooled, and frazil ice crystals grow and are deposited on the base of the ice shelf as marine ice. The water that eventually leaves the sub-ice shelf cavity is still below the surface freezing point, and is termed ice shelf water (ISW). In this thesis, this definition is used to cover any water mass with a potential temperature below the surface freezing point (Jacobs *et al.*, 1970). The overall process described above is called an ice pump (Lewis and Perkin, 1986).

One theory for the formation of WSBW is that it is formed by the mixing of HSSW, sometimes called Western Shelf Water (WSW), with Modified Warm Deep

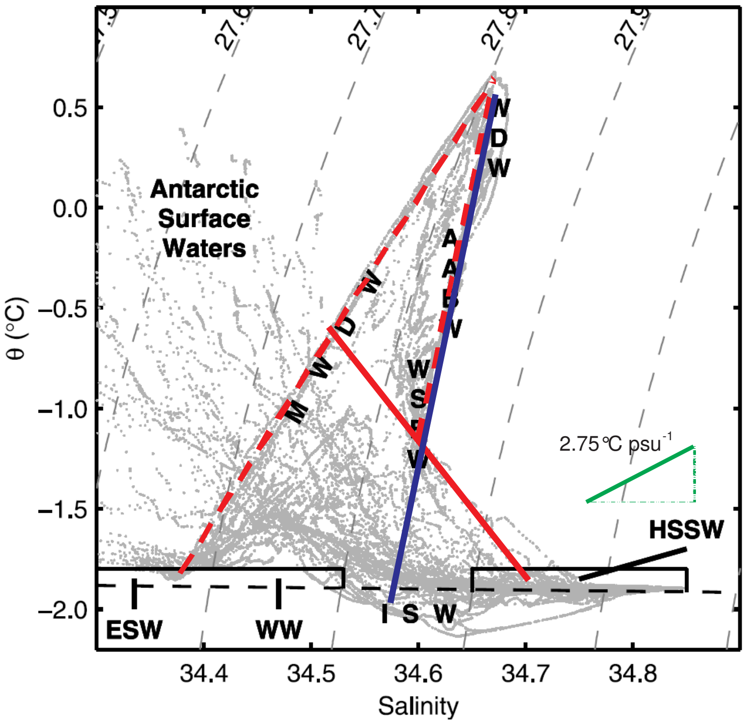

Figure 1.3: θ/S diagram from the southwestern Weddell Sea (from Nicholls *et al.*, 2003). Conceptual mixing lines for the formation of WSBW according to Foster and Carmack (1976) and Foldvik *et al.* (1985a) are shown in red and blue, respectively. The green line indicates a slope of $2.75\,^{\circ}\mathrm{C\,psu}^{-1}$.

Water (MWDW) near the shelf break (Gill, 1973, Foster and Carmack, 1976). However, another process involves ISW (Foldvik and Kvinge, 1974, Foldvik *et al.*, 1985a, Lewis and Perkin, 1986). ISW is the coldest water mass in the World Ocean; with decreasing temperatures, the compressibility of seawater is enhanced, so ISW may be dense enough to flow down the continental slope in a plume reaching supercritical speeds (greater than the phase speed of internal waves on the interface), allowing it to reach great depths before mixing with the overlying Warm Deep Water (WDW) to form WSBW (Foldvik *et al.*, 2004).

Both of these theories are shown on a θ/S diagram in Figure 1.3, superimposed on CTD data from the southwestern Weddell Sea (Nicholls *et al.*, 2003), with water mass definitions following Foldvik *et al.* (1985a). Eastern Shelf Water (ESW) is, as the name implies, found primarily on the eastern part of the continental shelf of the southern Weddell Sea, and is differentiated from HSSW by having salinities below 34.6. Salinities above this threshold are necessary for shelf water to be able to form bottom water by mixing with WDW (Fofonoff, 1956, Foster and Carmack, 1976). This process, cabbeling, relies on the non-linearity of the equation of state of seawater: a mixture between ISW or the most saline WW and WDW would be denser than either source water mass, letting it sink below these water masses. This is different from the Carmack-Foster process, in which mixing takes place between HSSW and MWDW (Carmack, 1977). According to Fahrbach *et al.* (1992, 1994) ESW is freshened by inflow from the Antarctic Coastal Current; Fahrbach *et al.* (1992) specifically mention meltwater from ice shelves as a contributing source. In the southern Weddell Sea, this meltwater is transported via the coastal current from the Eastern Weddell ice shelves (EWIS). Thus processes under EWIS play an important role in preconditioning water that contributes to bottom water formation in the southern Weddell Sea.

Winter Water (WW) is the remnant of the previous winter's mixed layer — essentially ESW that has been modified by the annual freezing and convection cycle, entraining some MWDW and cooling it down to near the surface freezing point; brine rejection from the formation of sea ice increases its salinity slightly compared with ESW.

1.2 The Antarctic Slope Front

One persistent dynamic feature found throughout the Weddell Sea is the Antarctic Slope Front, which separates the Atlantic-derived WDW from the colder surface waters. A diagram of this feature is shown in Figure 1.4. The front is set up as a response to Ekman forcing caused by prevailing easterly winds (Sverdrup, 1953): the induced southward current causes downwelling. In addition, the increased sea surface elevation toward the coast drives the geostrophic alongshore coastal current. Another process that can lower the isopycnals near the coast is convection in polynyas near the shelf break (Fahrbach *et al.*, 1992). However, this process seems unlikely to be significant in the eastern parts of the Weddell Sea, where the shelf is too narrow to produce a significant amount of convection. Opposing the front are two mechanisms: melting under the ice shelf will cause a reversed overturning, and the slope front itself will be subject to baroclinic instability, where it will spin off eddies, whose kinetic energy is drawn from a loss of potential energy, reducing the gradient of the front (Nøst *et al.*, 2011). These eddies can also transport warmer water onto the shelf, and may play a part in driving the reversed undercurrent that can be found beneath much of the coastal current (Chavanne *et al.*, 2010, Nøst *et al.*, 2011).

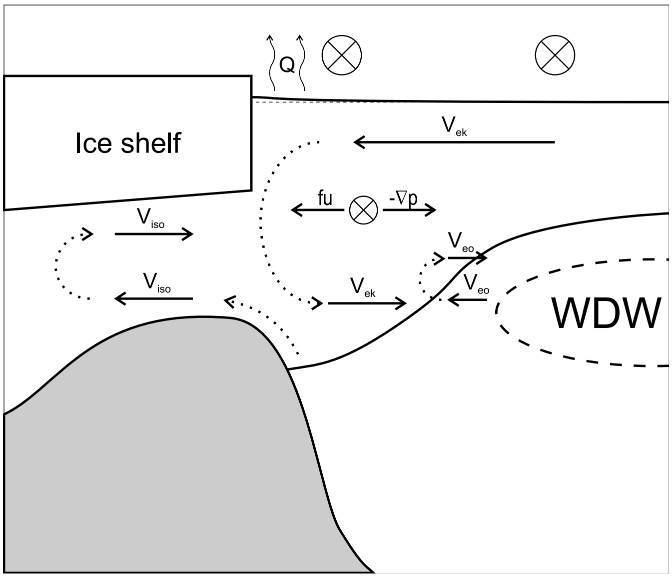

Figure 1.4: Diagram of the Antarctic Slope Front. The indicated overturning velocities are V_{ek}, the Ekman velocity V_{iso}, the ice shelf overturning velocity, and V_{eo}, the eddy overturning velocity. Q is heat loss to the atmosphere, leading to buoyancy loss. Based on a diagram in Nøst *et al.* (2011)

Price *et al.* (2008) looked at differences in the depth of the 0 °C isotherm between JR097 (the Autosub Under Ice cruise in 2005, which is described in more detail in Chapter 3) and climatological temperature fields from Klatt *et al.* (2005), which are averages of five CTD sections from between 1992 and 2000. However, in their final two sentences, they erroneously state that the depth of the 0 °C isotherm was at 1500 m depth in historical data from Klatt *et al.* (2005); since the observations from JR097 show the isotherm around 800 m, they conclude that "warm deep water may have had easier access to the continental shelf during 2005, and may be increasingly able to melt the ice shelf". However, the isotherm in Klatt's data was in fact around 800 m; the depth of the 0 °C isotherm *below* the WDW layer was just below 1500 m. As shown in Figure 1.5, the isotherm depths from JR097 are not significantly different from past data, though the observations do extend farther south onto the shelf than most previous datasets. So with our data from JR097 we cannot conclude that Fimbul Ice Shelf was melting more rapidly in 2005 than previously.

Historical depths of the 0 °C isotherm above the WDW layer from stations in the World Ocean Database (Boyer *et al.*, 2006) between 3° W and 3° E are plotted in Figure 1.5 (excluding data from before 1980), with additional data from Norwegian Antarctic Research Expeditions (e.g. O'Dwyer *et al.*, 2002), and data from JR097. The deepest interface depth is at 945 m, and is from *Polarstern* cruise ANT X/4 (Lemke,

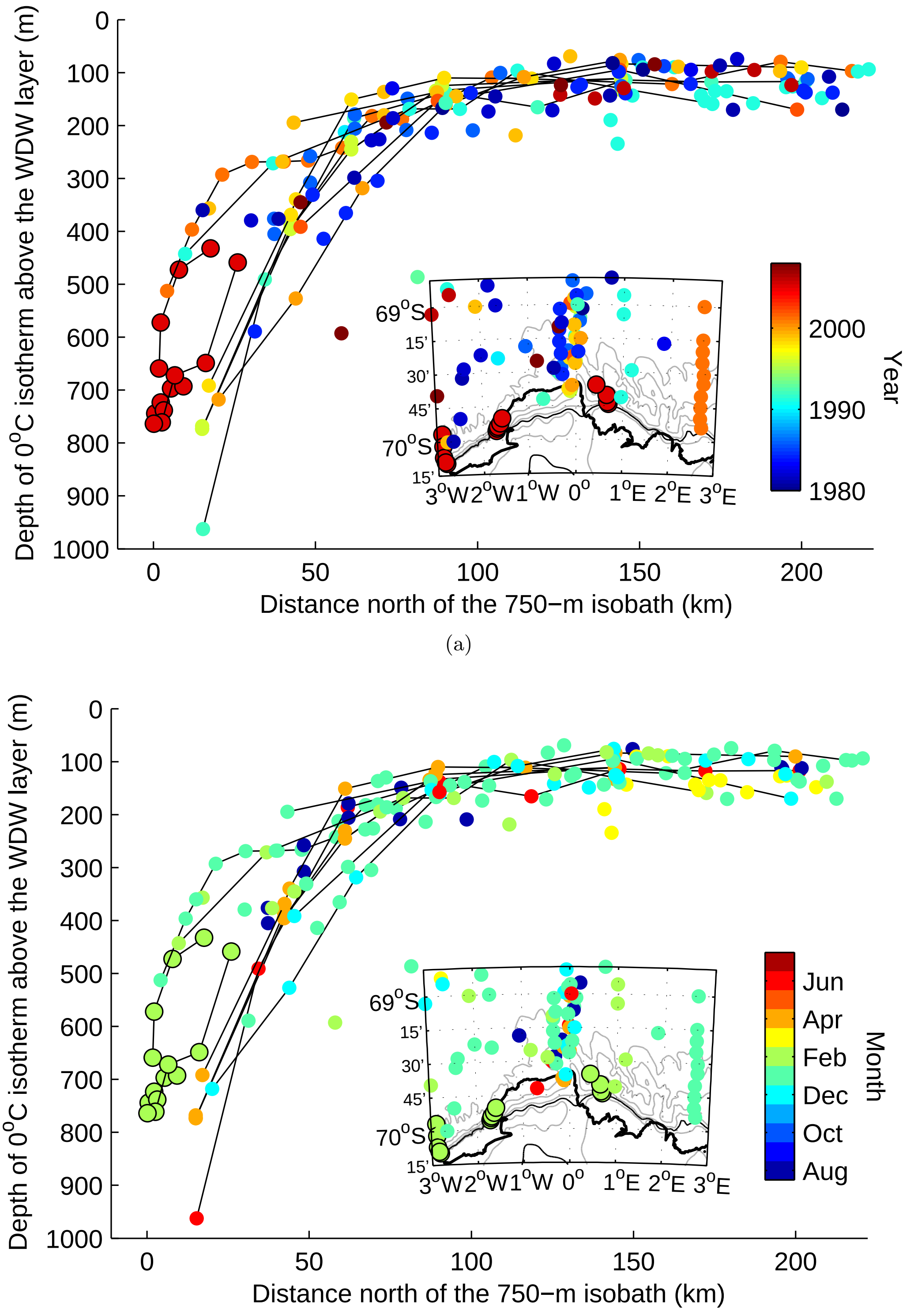

(a)

(b)

Figure 1.5: Depth of the 0 °C isotherm from historical cruises around Fimbul Ice Shelf, plotted against distance north of the 750-m isobath. Data from approximately 100 profiles from between 3° W and 3° E are plotted, colored by (a) year and (b) month of acquisition. Data from JR097 are highlighted with a black border; the interface depths from some contiguous cross-shelf sections have been connected with lines. The ice front in 2005 is shown with a thick black line on the map; the 750-m isobath is shown with a thin black line.

1994), in June 1992. This is the only cruise conducted in the middle of winter; other deep interface depths near the shelf break are found in April, suggesting that interface depths generally could be deepest in autumn and winter. No WDW has been observed at depths much shallower than 750 m depth. There are some historical data that could indicate the presence of WDW on the shelf, but these are most likely artifacts caused by XBTs hitting the bottom (J. Lutjeharms, pers. comm., 2009).

1.3 What influences ice shelf–ocean interaction?

The water mass transformations that take place beneath ice shelves are described by Nøst and Foldvik (1994) and Gade (1979). These processes modify both the temperature and the salinity of the water, as well as other properties such as the δ^{18}O ratio (Gade, 1979, Schlosser *et al.*, 1990).

The melt rate depends on several different factors including the draft, basal roughness, and interior temperature of the ice shelf and the speed and temperature of the water. The draft of the ice shelf will determine the in-situ freezing point of the water (through increased pressure at depth). The actual energy transfer between the water and the ice is controlled by turbulent transport in the boundary layer and by the formation and deposition of frazil ice on the base of the ice shelf (Lewis and Perkin, 1986, Smedsrud and Jenkins, 2004, Holland and Feltham, 2005). The roughness of the base of the ice shelf will influence the boundary layer, but this has not yet been quantified for ice shelves, as few data are available (Lewis and Perkin, 1986, Nicholls *et al.*, 2006).

The results of melting of ice into the ocean can be seen as a line in T/S space (Gade, 1979). The slope of this line, passing through the point (T_0, S_0) is

$$\frac{(T_0 - T_f) + (T_f - T_i)c_i/c_w + L/c_w}{S_0}$$

where T_0 and S_0 are the far-field temperature and salinity, T_f is the temperature at the interface (usually the freezing point of seawater at the basal pressure), T_i is the far-field temperature of the ice shelf, L is the latent heat of ice, and c_i and c_w are the specific heats of ice and water. This assumes that the ice shelf is near steady-state conditions, which is generally true. Typical values of the slope in T/S space for the cavity beneath Filchner-Ronne Ice Shelf (FRIS) are around 2.4–2.75 $^\circ\mathrm{C\,psu}^{-1}$; they may be slightly higher for Ross Ice Shelf. According to Nicholls *et al.* (2001) the first term is small compared with the others and can be ignored; the second term is one order of magnitude smaller than the third, but is significant. The main varying factors are the source water mass (T_0, S_0), and the draft and interior temperature of the ice shelf; the source salinity is more important than temperature in determining the slope of the line.

1.4 Measurements beneath various ice shelves

1.4.1 Ross Ice Shelf

Although a hole was drilled most of the way through Ross Ice Shelf during IGY in 1957–8, the first direct measurements under an ice shelf were made in 1977, as part of the Ross Ice Shelf Project (Clough and Hansen, 1979). A hole at station 'J9', 475 km from the ice front, was drilled using a flame drill, and kept open for three weeks. Various instruments were lowered through this hole including water samplers, reversing thermometers, a recording temperature/pressure profiler, and cameras and traps to observe the seabed and the animals living there. Along with the data from the borehole, CTD data from the ice front indicated that there was net melting at the base of the ice shelf (Jacobs *et al.*, 1979).

Drilling, both to retrieve sediment and to deploy oceanographic instrumentation beneath McMurdo Ice Shelf, took place as part of the Andrill program before and during IPY 2007–2008 (Robinson, 2004, Robinson *et al.*, 2010).

Several ocean circulation models have also been applied to the Ross Ice Shelf, including POLAIR (Holland *et al.*, 2003) and a version of the ROMS ocean model, modified to include sub-ice shelf cavities (Dinniman *et al.*, 2007).

1.4.2 Pine Island Glacier

Pine Island Glacier, a name used both for the glacier and its floating ice shelf, is a fairly small ice shelf in the Amundsen Sea. However, it has received much attention in recent years for its very rapid acceleration and thinning (Joughin *et al.*, 2003, Wingham *et al.*, 2009), which could even play a major role in global sea level rise (Joughin *et al.*, 2010), and has been called the "weak underbelly of the West Antarctic Ice Sheet"

(Hughes, 1981). While much of the floating ice shelf is heavily crevassed, making in-situ measurements difficult, measurements have been made along the ice front from ships (e.g., Jacobs, 2009). In addition, in early 2009 the Autosub-3 AUV was deployed from RVIB Nathaniel B. Palmer, performing six under-ice missions, giving vital new information about the hydrography and especially the topography beneath the ice shelf (Jenkins *et al.*, 2010). This work can be considered an extension of the earlier missions using Autosub-2 beneath Fimbul Ice Shelf, as described in Chapter 3.

1.4.3 Ronne-Filchner Ice Shelf

The Weddell Sea plays a particularly important role in the climate system, since a large part of Antarctic Bottom Water (AABW) is derived from WSDW (Broecker *et al.*, 1998). As the largest ice shelf in the Weddell Sea, the oceanography of FRIS and the surrounding continental shelf has been extensively studied since 1968, when the first multi-year mooring was deployed on the Filchner Sill, a key outflow region north of Filchner Ice Shelf. Since then more than 20 moorings have been deployed in this area (Foldvik *et al.*, 2004), and several moorings have been deployed through the ice shelf (Nicholls and Makinson, 1998, Nicholls and Østerhus, 2004). Several of the moorings deployed through holes drilled in the ice shelves have yielded multi-year time series, giving clues to the general circulation (Nicholls *et al.*, 2001) and ventilation timescales (Nicholls and Østerhus, 2004) under the ice shelf.

In addition to field data, the ice shelf has been studied using the POLAIR model (Jenkins and Holland, 2002, Jenkins *et al.*, 2004). The latter paper simulates the ventilation of the ice shelf cavity, and then compares it with the data from under the ice shelf. The ocean cavity beneath FRIS is the most studied and probably the most well-constrained in Antarctica.

The continental shelf north of Filchner-Ronne Ice Shelf is several hundred kilometers wide; this differentiates the ice shelf from many of the smaller ice shelves upstream, which are only a few kilometers, if that, from the shelf break. There are many measurements on the shelf around Filchner Depression, both hydrographic surveys (e.g., Foldvik *et al.*, 1985b) and multi-year moorings (Foldvik *et al.*, 2004). Many different processes occur on the shelf, including freezing, resulting in the production of brine that goes into forming HSSW. But in addition, there are most likely shelf waves at the shelf break (Middleton *et al.*, 1982, Darelius *et al.*, 2009), and there are many

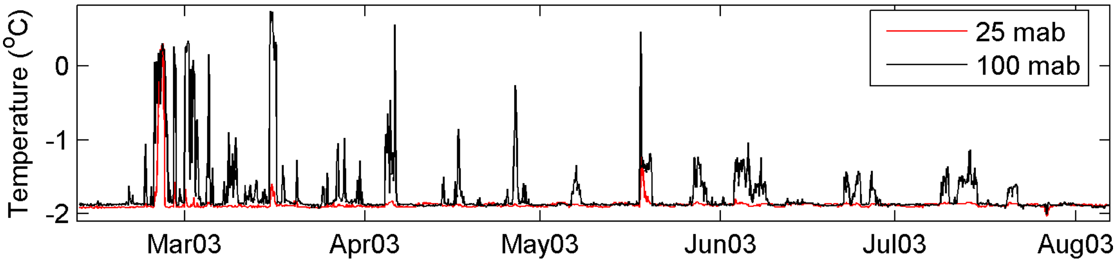

Figure 1.6: Temperature variations from current meters 100 m and 25 m above the bottom in the west side of Filchner Depression (site "S2", 74° 40′ S 33° 27′ W; unpublished data).

observations of intrusions of MWDW onto the shelf (e.g. Foldvik *et al.*, 1985b). The spatial structure of these intrusions is very irregular, and there also appears to be high temporal variability, with some evidence of diurnal tidal cycles, as well as longer pulses of warm water flowing onto the shelf. Figure 12 of Foldvik *et al.* (1985b, not shown here) shows two months of data from a mooring on the west side of Filchner Depression, where pulses of warm water are clearly visible. A mooring at this location has been in place since 2003, and data from this more recent deployment, shown in Figure 1.6, also show pulses of warm water, most visible at 100 mab, but occasionally visible at 25 mab.

While direct measurements of mixing using microstructure profilers have not yet been published (a survey took place in Jan.–Mar. 2009), indirect inferences of eddy diffusivities have been made by Daae *et al.* (2009). These measurements indicate that a thick bottom boundary layer is present on the continental shelf, most probably enhanced by the proximity to the critical latitude for M_2 tides, where enhanced mixing rates are found.

1.5 Eastern Weddell ice shelves

Fahrbach *et al.* (1994) discuss the importance of the Eastern Weddell ice shelves (EWIS) to the Weddell Sea in general. They found that the narrow width of the continental shelf suppresses the local formation of bottom water, as very little of the salt released by freezing in polynyas (discussed in more detail by Markus *et al.*, 1998) accumulates on the shelf. Thus no HSSW is produced around EWIS. The narrow shelf also allows more WDW and MWDW to reach the ice shelves, causing more melting. The melt water in turn stabilizes the water column, further suppressing deep water formation. Fahrbach *et al.* (1994) deployed three moorings near Vestkapp, west of Fimbul

Ice Shelf; one of these was on the slope, one was on the shelf, and one was directly in front of the ice front, under the fast ice. All of these moorings measured water that was significantly above the freezing point; the slope mooring measured temperatures up to 0.6 °C. The warm events seem to begin from the bottom, spreading upward, a signal consistent with WDW flowing up the slope (unlike observations from a short-term mooring that was deployed near Fimbul Ice Shelf as part of this project, and is described in Section 3.6). If unmodified WDW can flow onto the continental shelf and melt the base of the ice shelves, this will reduce the salinity of the surrounding water faster than brine release from sea-ice production in polynyas can increase it, since the continental shelf is so narrow.

Hellmer (2004) studied the melt rates of Antarctic ice shelves in BRIOS, a coarse-resolution circum-Antarctic model, and found that the EWIS, including Fimbul Ice Shelf, supplied a disproportionately large amount of melt water. Some of this is probably caused by the resolution of the model grid, which does not resolve the continental slope, allowing WDW to access the ice shelves too easily, thereby overestimating the melt rates. However, evidence from several other models, as well as observations, also points toward high melt rates beneath these ice shelves.

Nicolaus and Grosfeld (2004) applied a model with around 5 km resolution to Ekstrømisen, and performed various sensitivity studies to see how the melt rates depend on the width of the continental shelf. By widening the shelf by two grid points (11 km) the basal melt rates were reduced by a third. Another interesting feature of this model is that the coldest ISW, which was found in the vicinity of the deepest ice streams near the south of the cavity, recirculates extensively within the cavity, leading to a long residence time. In contrast, the ISW formed at shallower depths is flushed out of the cavity much sooner.

Another model that has been applied to EWIS is Rombax (Thoma *et al.*, 2006), which uses a slightly finer grid. Again the conclusions are that the oceanographic impact of EWIS is extremely sensitive to changes in the inflowing water as well as to changes in the ice shelves themselves. In a scenario where the ice shelves are removed entirely, convection takes place on the newly exposed shelf area, producing much higher salinity shelf waters, and the water column is generally less stable.

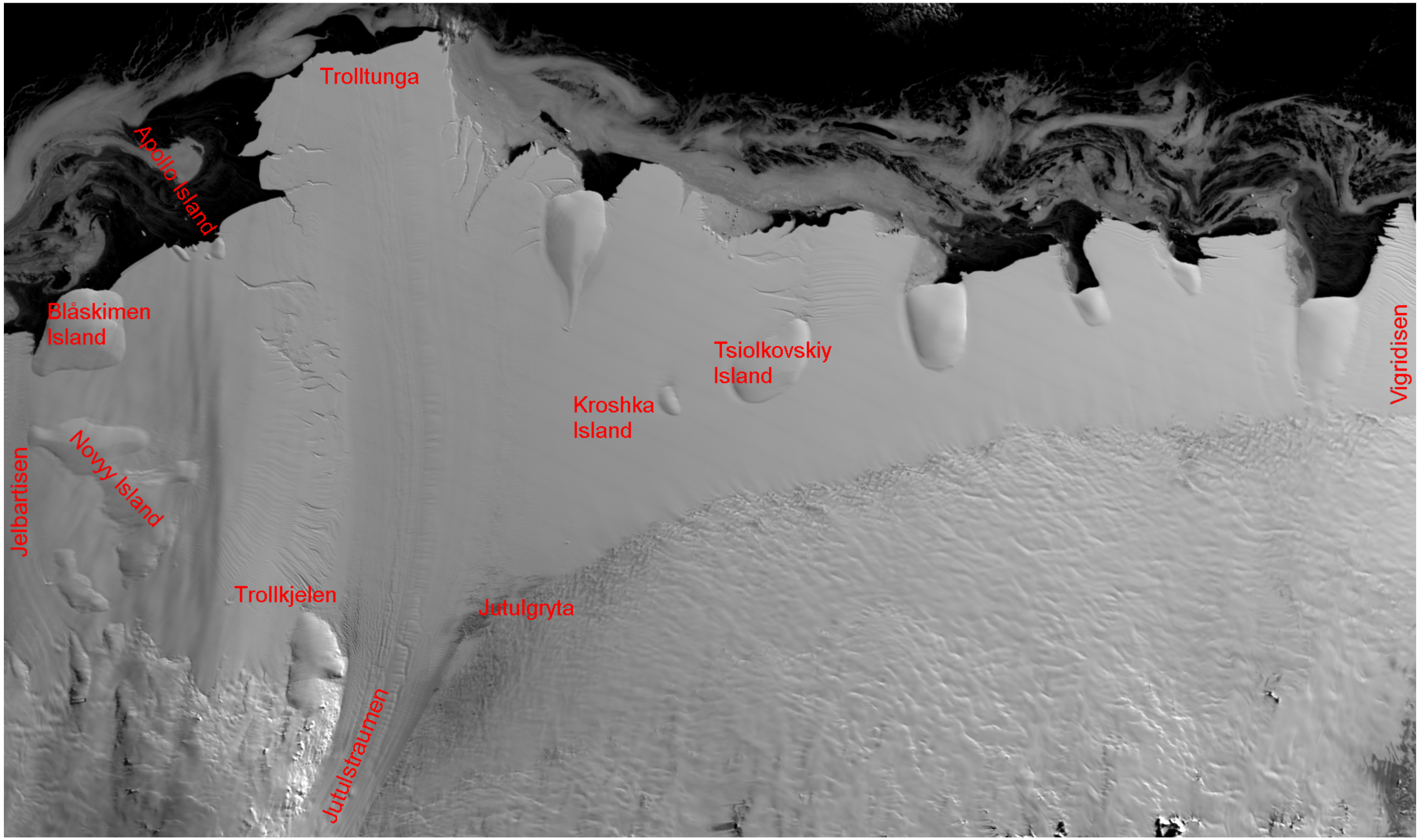

Figure 1.7: MODIS satellite image of Fimbul Ice Shelf, taken on 1 April 2005 08:55 UTC. A subsection of this image with enhanced contrast is shown in Figure 3.10c.

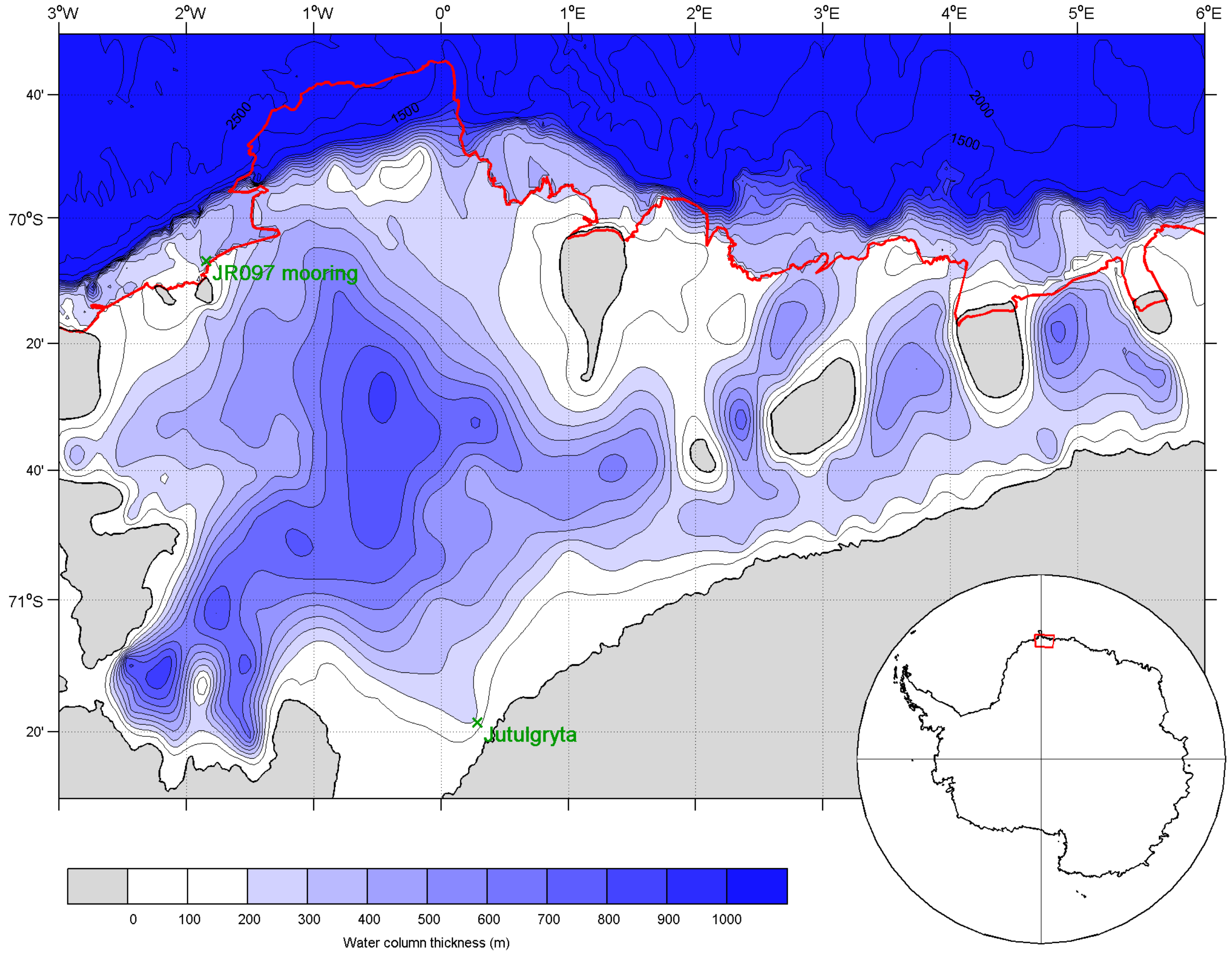

Figure 1.8: Water column thickness beneath Fimbul Ice Shelf (data from Nøst, 2004), with the ice front from February 2005 indicated with a red line.

1.6 Fimbul Ice Shelf

One of the most interesting ice shelves in the Eastern Weddell Sea is Fimbul Ice Shelf, also known as Fimbulisen (see the map in Figure 1.1 and satellite image in Figure 1.7). The ice shelf is fed by Jutulstraumen, an ice stream draining an area of around 126,000 km^2 (Melvold and Rolstad, 2000). The ice shelf is unique in that it extends far enough northward to overhang the continental slope. The glacier tongue, Trolltunga, was even more pronounced before 1967, when it extended almost 100 km farther than at present. The ice tongue was possibly hit by a large iceberg originating from the Amery Ice Shelf, causing it to break off and drift into the Weddell Sea, where it was tracked by satellites for over a decade (Swithinbank *et al.*, 1977).

The main ice stream that continues toward the remnants of Trolltunga is flanked by two fracture zones, Trollkjelen on the west and Jutulgryta on the east. To the west of the ice shelf there is a grounded area separating Fimbul Ice Shelf from adjacent Jelbartisen, while on the east there is a string of islands and grounded areas that define the seaward extent of the ice shelf. In addition to the large islands that are clearly visible in Figure 1.7, there is a group of smaller islands, the largest of which is Apollo Island, near the ice front directly west of the tongue, while there are two smaller clusters of ice rises east of the large drop-shaped ice rise east of the tongue.

Because of its proximity to the Norwegian bases Troll and the now-defunct Norway Station and SANAE III, ships have accessed the ice front of Fimbul Ice Shelf regularly since the 1970s to re-supply the stations. However, few oceanographic measurements have been made near the ice front.

The only measurements beneath the ice shelf itself come from three different projects, two of which are used in this thesis. In 1990–1992 a mooring was deployed through a fracture zone called Jutulgryta, east of the area where Jutulstraumen flows into Fimbul Ice Shelf (Orheim *et al.*, 1990, Østerhus and Orheim, 1994). These data are described in Chapter 2. In early 2005 a cruise on RRS James Clark Ross was carried out in the area around Fimbul Ice Shelf. During this cruise the Autosub-2 AUV was deployed beneath the ice shelf for one successful mission. Data from the ship-based measurements and from Autosub-2 are described in Chapter 3. Finally, in the 2009–2010 season the Norwegian Antarctic Research Expedition deployed three moorings through Fimbul Ice Shelf, and performed several CTD casts (Nøst *et al.*, 2010a,b). The mooring data were recovered in the 2010–2011 season and preliminary results of the CTD data were shown at the IPY Oslo Science Conference in June 2010 (Nøst *et al.*, 2010b).

1.6.1 Bathymetry

The bathymetry beneath Fimbul Ice Shelf is known at a spatial resolution of around 10 km from a seismic survey undertaken in the 2000–2001 field season (Nøst, 2004); the water column thickness has been plotted in Figure 1.8. There is a main basin in the central area of the ice shelf, with a sill near the western side of the base of the ice tongue. In addition there are several shallower sills on channels leading into the main basin from the east.

Measurements of ice thickness (but not sea-level depth) were conducted in 1968–1969 by the Belgian Antarctic Expedition and in 1994–1995 by AWI using airborne echo sounding (Steinhage *et al.*, 1999). Humbert (2006) used these data together with the data from Nøst (2004) to derive a new map of ice thickness, and showed that including the older data resulted in a considerably narrower keel along the extension of Jutulstraumen. However, those data have not been used for this thesis.

1.6.2 Glaciology

The flow of ice on Fimbul Ice Shelf has not been extensively studied through fieldwork. There has been a series of measurements of the motion of the ice shelf in connection with the Norwegian Antarctic Research expeditions in 1990 and 1992 using stakes (Orheim *et al.*, 1990, Østerhus and Orheim, 1994). In addition, a thermistor string was deployed through the ice shelf at $70^\circ\,59'\,\mathrm{S}\ 0^\circ\,12'\,\mathrm{W}$, near the deepest part of the keel. The temperatures were measured in Feb. 1990, following deployment, and again in Feb. 1992. The profiles showed remarkably cold temperatures, decreasing to $-28\,^\circ\mathrm{C}$ at 200–325 m depth. The thickness of the ice shelf is estimated at 400 m at this point, and it is about 45 km from the grounding line identified by Melvold and Rolstad (2000). While these cold temperatures were initially explained by high melt rates ablating the ice from below (before the ice can warm), they could also be caused by high flow rates in the central section of the ice shelf.

Recent glaciological modeling of Fimbul Ice Shelf by Humbert (2006, 2010) has attempted to explain the temperature profiles using a three-dimensional finite-element model of the ice shelf, forced using surface velocity fields (from remote sensing) and accumulation (precipitation) rates. These are then used to calculate flow rates, which in turn can generate three-dimensional temperature distributions throughout the ice shelf. The more recent simulations (Humbert, 2010) indicate that it is possible to match the observed temperature profiles quite well when the strength of the ice shelf is reduced in the shear margins; Humbert also compared the derived melt rates with values from Smedsrud *et al.* (2006) and the modeling results presented in Chapter 4.

Jutulstraumen has been mapped using ground-penetrating radar by Melvold and Rolstad (2000); in addition, they present some plots of velocity maps from interferometric synthetic aperture radar (INSAR). Large-scale studies of the mass balance of Antarctica using INSAR have shown that Jutulstraumen is approximately in balance overall (Rignot and Thomas, 2002). This implies that the precipitation over the ice stream's catchment area is approximately equal to the outflow into Fimbul Ice Shelf, estimated at 13.4 ± 1 $\mathrm{km}^3\,\mathrm{a}^{-1}$ ice equivalent. A rough calculation of the mass balance of Fimbul Ice Shelf itself is given in Section 4.4.4.

1.7 Oceanography of the Eastern Weddell Sea

To place Fimbul Ice Shelf in its oceanographic context, we must look at the water masses in the wider region. Temperature, salinity, and density sections as well as a θ/S diagram from O'Dwyer *et al.* (2002) along $2^\circ\,40'$ E are shown in Figure 1.9. This section runs over Maud Rise (just south of 65° S) to the continental slope; measurements were made to a depth of 2000 dbar only, because of instrument problems.

There is a clear core of warm, saline water centered around $68^\circ\,15'$ S; this is WDW, a derivative of Circumpolar Deep Water (CDW) (Heywood *et al.*, 1998). The surface layer is fresh (< 34.2) throughout the section, but the temperatures are lowest toward the ice front. In the southern part of the section, a wedge of Winter Water (WW) is visible between 100–250 m depth. Contrary to what is stated in O'Dwyer *et al.* (2002) no ISW is present in this section, although the water closest to the continental shelf most likely does contain some meltwater from the adjacent ice shelf: its potential temperature is close to, but above, the surface freezing point throughout. The slope front is clearly visible in the sections, with the upper boundary of the WDW, defined as the 0 °C isotherm, deepening toward the shelf break.

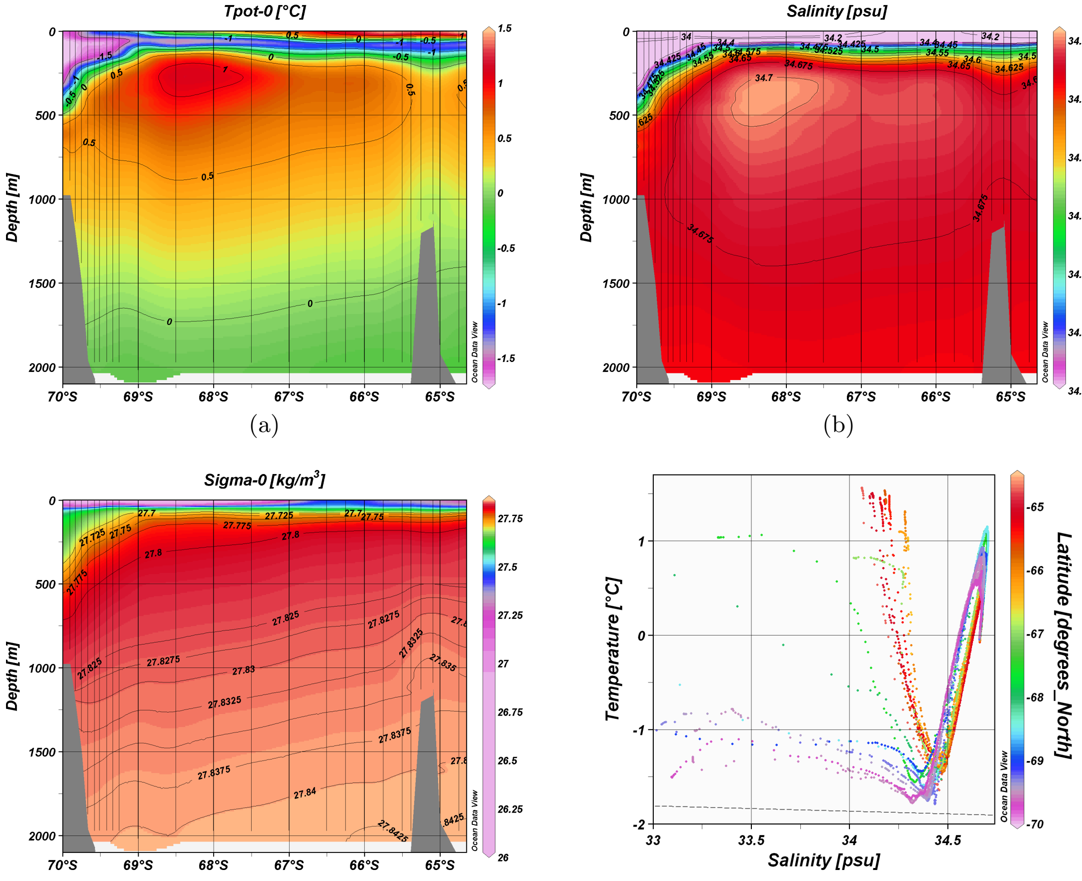

(a) (b)

(c) (d)

Figure 1.9: (a)–(c) Potential temperature, salinity, and potential density σ_0 sections along $2^\circ\,40'$ E; and (d) θ-S diagram from the same profiles, Feb. 2001, with the dashed line indicating the surface freezing point (from O'Dwyer *et al.*, 2002). Measurements were only made to 2000 dbar pressure.

Chapter 2

Jutulgryta

In 1990, as part of the Norwegian Antarctic Research Expedition 1989/90, several instruments were deployed through a fracture zone called Jutulgryta, east of the area where Jutulstraumen flows into Fimbul Ice Shelf (shown on the map in Figure 1.8; Orheim *et al.*, 1990, Østerhus and Orheim, 1994).

A hole was drilled on the site, which is situated in a rift partly filled with marine ice around 30–50 m thick, using a hot water drill. The drill was lowered down to 38 m, before it finally cleared the ice. However, there were many slushy ice layers below the consolidated ice, which had a thickness of only 11.1 m, with a freeboard of around 2.8 m (Orheim *et al.*, 1990, Appendix 2). CTD casts and other short-term instrument deployments were made through the hole, and finally an instrument mooring was deployed for almost two years, with a unit on the surface that stored data and also transmitted the data via the Argos satellite system. The transmitter failed shortly after deployment, though data were still recorded in the surface unit. A diagram of the mooring setup, with sample types of instruments, is shown in Figure 2.1. In December 1991 the site was revisited, and the mooring drilled free. At that time, the ice thickness was 29 m, with a freeboard of around 2 m (S. Østerhus, pers. comm., 2006)

In many ways, Jutulgryta is not a typical ice shelf site. Rifts like this cover only a small fraction of the ice shelf area, and heat fluxes through the relatively thin ice are probably much higher than in the rest of the ice shelf. Also, conditions within the rift are likely not representative of the larger ice shelf cavity, with the upper parts of the rift seeing larger quantities of surface runoff, and reduced currents.

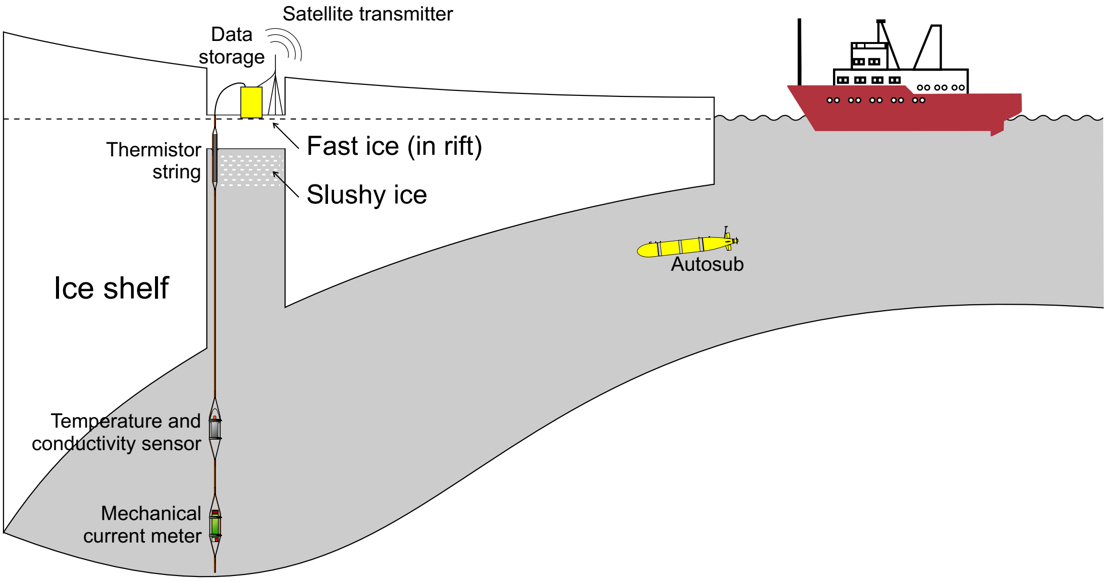

Figure 2.1: Diagram of sub-ice shelf mooring through a rift, as in Jutulgryta. Note that a satellite transmitter was not used at Jutulgryta. Not to scale.

2.1 Instruments and methods

2.1.1 CTD casts

In Feb. 1990 five CTD casts were taken through Jutulgryta using a Meerestechnik Elektronik (ME) probe. Over this time, the calibration of the conductivity cell drifted considerably. The spread in conductivities is around 0.03 mS/cm, and there are no water samples that could be used to calibrate the measurements. The ME probe, serial no. 48, was re-calibrated in December 1990, and these values indicate that the temperatures have an offset of 0.015 °C. This value has been subtracted from all temperature points from the instrument.

A second set of CTD casts was made on 11–27 Dec. 1991 using a different probe, serial no. 67. The conductivity profiles from this dataset have quite significant offsets, up to 0.4 mS/cm. Because of these offsets, and because a large fraction of the measurements were outside the range of expected values, the profiles were collapsed onto one line in T/S space. From these shifted values, median profiles were calculated for both sets of casts. After viewing these profiles in T/S space and comparing them with the Autosub and JR097 CTD datasets, an offset of -0.07 was applied to the 1990 salinities, and an offset of 0.11 was applied to the 1991 salinities (Nicholls *et al.*, 2008).

2.1.2 IFIX mooring

The mooring in Jutulgryta consisted of a loop of wire, with the ends attached to the surface unit, and instruments clamped onto the wire at various depths. The instruments transmit and receive data by induction, using the IFIX system (Christian Michelsen Research, 2006), similar to the moorings mentioned in Section 1.4.3. The surface unit polls each instrument in sequence every three hours; the instruments then send their data up the wire to the surface unit. The data were stored in an Aanderaa Instruments 2990E extended data storage unit (DSU), with a capacity of 262100 10-bit words (AADI, 2010). The unit has an internal clock, and time stamps are added every day at the first time that data are received after midnight. However, during the deployment the clock failed on 12 June 1991 (Østerhus and Orheim, 1994). Data after that time are still valid, but the time stamps are not, and most are missing. So we have no way to verify the dates for the subsequent data. However, extrapolating the time stamps to the end of the data, the time series lasts until 9 Dec. 1991, which was during the recovery fieldwork.

The mooring was deployed in Feb. 1990 and left in place until Dec. 1991, yielding a time series of almost two years. A list of instruments (based on the table in Appendix 2 of Orheim *et al.*, 1990) is provided in Table 2.1.

The instruments mainly consisted of temperature-conductivity and temperature sensors. Temperatures were measured using Fenwall GB32JM19 thermistors. Temperature sensors 0–7 were calibrated in a water bath in Bergen, in temperatures around -1.2–$-0.2\,^{\circ}$C (usually a narrow range for each sensor); this was used together with temperature data from CTD cast no. 3 from 1990 to derive calibrations for these sensors. Unfortunately the IFIX data start at 02:49 on 13 Feb. 1990, while the last CTD cast began at 19:46 on 11 Feb. Given the variability in temperatures between casts (0.012 °C at 251 m depth, up to 0.045 °C at the bottom), and the apparent mismatch between IFIX data and CTD casts just following recovery, the error in calibrations for the T/C sensors is currently estimated at 0.075 °C.

The temperature sensors on the current meters have complete laboratory calibrations, which have been applied. Temperature sensors 8–11 have a considerably wider range and lower resolution; the original processed data were used to calculate calibration coefficients to apply to the re-processed data. The same procedure was used for the thermistor string.

Table 2.1: Instruments deployed at Jutulgryta. Depths are measured from the surface of the ice, around 2.8 m above sea level in Feb. 1990. T=temperature only, C/T=conductivity and temperature, CM=current meter, TC=thermistor chain

Depth (m)	Instrument no.	Data channels	Instrument type	Temperature range	Temperature resolution	Last valid measurement
3.0[a]	8	17	T	−30 – −1	0.026	9 Dec. 1991
6.0[a]	9	18	T	−30 – −1	0.026	9 Dec. 1991
10.1–11.6[b]	12	21–28[c]	TC	−5 – +1	0.006	9 Dec. 1991
13.1	0	1–2	C/T	−4.1 – +2.4	0.006	9 Dec. 1991
16.1	1	3–4	T	−4.1 – +2.4	0.006	9 Dec. 1991
21.1	2	5–6	C/T	−4.1 – +2.4	0.006	9 Dec. 1991
26.1	10	19	T	−40 – −1.5	0.037	9 Dec. 1991
31.1	3	7–8	C/T	−4.1 – +2.4	0.006	9 Dec. 1991
41.1	13	29–32	CM	−5 – +1	0.006	16 Apr. 1990
51.1	4	9–10	C/T	−4.1 – +2.4	0.006	9 Dec. 1991
101.1	11	20	T	−40 – −1.5	0.037	9 Dec. 1991
201.1	14	33–36	CM	−5 – +1	0.006	26 Apr. 1990
251.1	5	11–12	C/T	−4.1 – +2.4	0.006	9 Dec. 1991
301.1	6	13–14	C/T	−4.1 – +2.4	0.006	none
371.1	15	37–40	CM	−5 – +1	0.006	22 May 1990
391.1	7	15–16	C/T	−4.1 – +2.4	0.006	none

---

[a] In ice

[b] Ice/ocean interface at 11.1 m (Østerhus and Orheim, 1994)

[c] Starting with the deepest sensor

The stability of the sensors is estimated to be within 0.05 °C/year (Orheim *et al.*, 1990). The drift is probably not this large, but since no post-calibration was done, apart from a comparison with later CTD casts, we cannot be sure. The stated accuracy of the temperature sensors on the current meters is 0.05 °C (Aanderaa Instruments, 1993), with a resolution of approximately 0.006 °C. The actual accuracy is probably considerably better than this.

The conductivity measurements were made using Aanderaa 2994 inductive conductivity cells. These have a resolution of 0.073 mS/cm (a range of 0–74 mS/cm with 10 bits resolution), with a claimed accuracy of 0.025 mS/cm (Orheim *et al.*, 1990). For the uppermost instruments, where salinity varies with seasonal runoff, the salinities do vary significantly. However, in the deeper layers, this resolution is inadequate to resolve almost any variations that occur in the time series. Several of the 11 sensors did not produce any data; sensor 3 drifted towards unrealistically high values, while sensor 4 gave persistently low readouts, except for fifteen days in late April/early May 1990, when the data look realistic, but with many data missing.

The current meters deployed in Jutulgryta were based on Aanderaa RCM7 mechanical current meters. However, as a large vane could not be lowered through an 18-cm borehole, the instruments were modified so they had a Savonius rotor on the top to measure current speeds, and had an extra section added to the bottom of the instrument case, with a small vane pivoting around the axis of the instrument. A compass measured the orientation of the vane, with another more centrally located compass measuring the orientation of the instrument housing. The two measurements are added in the instrument to provide the current direction. Unfortunately none of the current meters worked longer than around two months, and many of the measured current strengths were so low that they were near the threshold for turning the rotor.

The data stream from the IFIX sensor string was downloaded from the DSU as an ASCII file, with the complete data stream as a series of decimal words. These were then loaded into MATLAB, time stamps were extracted, and the data were assigned to the correct channels — 40 in total. Apart from various outliers, most of the data were recorded correctly.

Some of the sensors did have problems with their data: both the temperatures and conductivities from instrument 0 are occasionally shifted one or two bits to the right, though when this occurs it is obvious and can be easily be corrected. And in the end of July 1991 there are some times when the data from all of the channels of the thermistor string were shifted two bits to the right. It is possible that the electronics were affected by the cold, combined with drops in battery voltage over time. However, the problem seemed to correct itself after a few days. Conductivity sensor 3 had a very specific problem: the second-highest (256) bit dropped out in mid-October 1990. Again, this was very easy to correct, and was probably caused by problems with the electrical connections to the A/D converter in the instrument.

Other data from Jutulgryta include several short current meter records from the recovery season, and a one-month time series from an Aanderaa WLR-5 bottom pressure recorder, described briefly in Section 3.3.1.

2.2 Results

Median CTD profiles from the two drilling seasons are shown in Figure 2.2a. There is a general warming of the water under Fimbul Ice Shelf between the first and second groups of profiles; this was also seen in the IFIX data. Near the surface, there is fairly warm water; once we reach the bottom of the slushy ice layer, temperatures decrease as salinities increase. The coldest water is found just below the draft of the ice shelf outside the fracture zone (around 200 m). This is also consistent with the data from Autosub. Temperatures and salinities then increase towards the bottom.

The θ/S diagram in Figure 2.2b shows how the water mass properties change between the two years. While the deeper water masses appear to be related, near the temperature minimum there is a considerable freshening from 1990 to 1991. The 1990 profile appears to be very close to the conditions encountered by Autosub farther beneath the ice shelf in 2005 (mission 382, labeled as "M382"), while the 1991 profile is closer to the water masses observed near the ice shelf front on the outbound track. It is possible that the lower salinities observed are caused by an increased proportion of glacial meltwater or AASW. If it is the former, this could either be because the water took a longer pathway into the main cavity from one of the eastern sills, or because the source water was warmer, causing more melting on its way to the mooring site.

The temperatures from both sets of CTD casts and from the moored IFIX instruments are shown in Figure 2.3a. The only temperature sensor below the ice shelf draft that worked for the whole deployment was at 251 m depth.

In Figure 2.3b the first three months of the time series have been stretched to show the large variation taking place in the lower temperature sensors. The sensor at 100 m is not shown, since it has considerably coarser resolution. The water at the level of the deepest instrument, at 371 m depth, approximately 30 m above the bottom, starts at a higher temperature than the other instruments, but cools toward April. There are several episodes in April–May 1990 when temperatures rise by more than 0.1°C for about a week. The first of these pulses is visible both in the 251m sensor and in other instruments and lasts for several sampling cycles. These pulses of warmer water occur several times in the deeper instruments. The instrument at 371 m also had a current meter, which showed increased speeds (around 5 cm/s) during this warm episode. Unfortunately the deepest temperature sensor stopped operating after three months (on 21 May 1990).

The temperatures and salinities from the uppermost instruments are shown in Figure 2.4. Many different processes can be seen here. Firstly, the annual temperature cycle can be seen in the uppermost instrument at 3 m depth; this signal is attenuated at deeper depths. Note that the temperatures at 3 and 6 m depth are above -1°C in the beginning of the time series, but that is above the limit of the measurement range for these two sensors. The two uppermost sensors on the thermistor chain show gradually decreasing temperatures at the beginning of the time series; the upper one ends

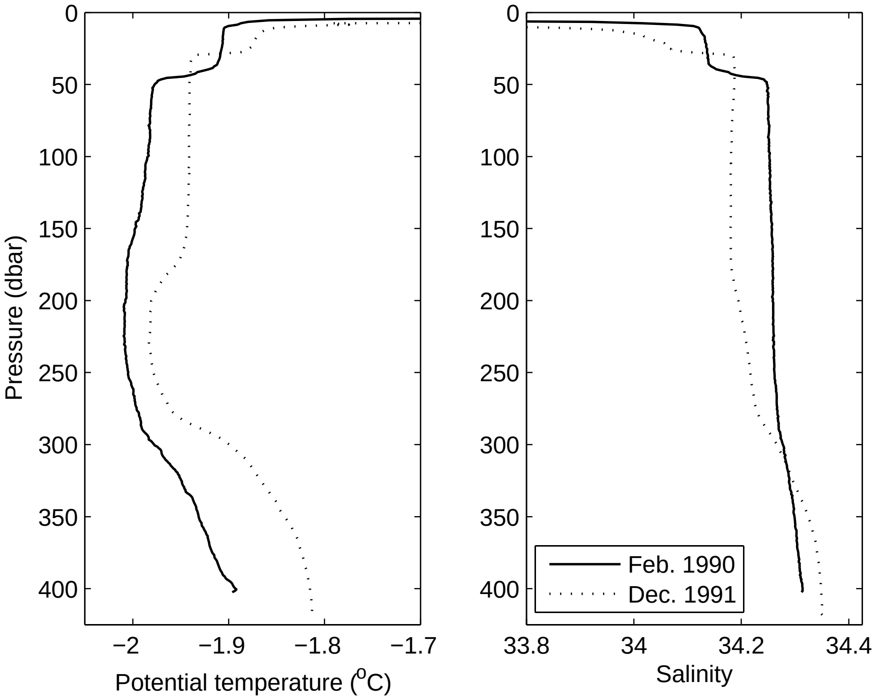

(a)

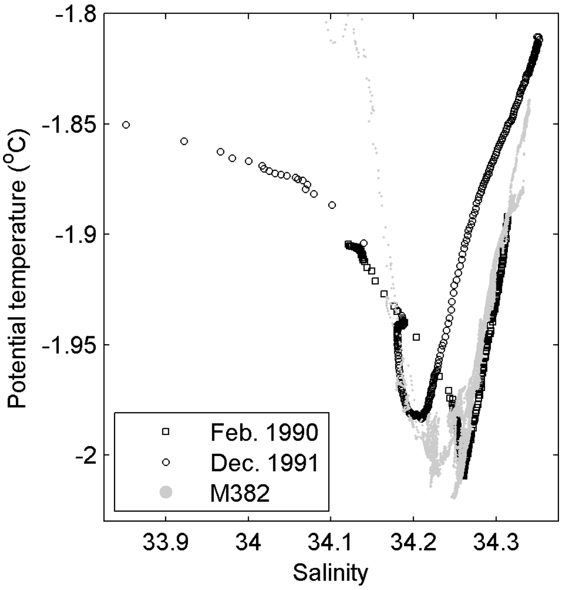

(b)

Figure 2.2: Median CTD profile data from Jutulgryta. The salinities have been shifted according to the values of Nicholls *et al.* (2008). (a) Median CTD profiles from the two field seasons. (b) θ/S diagram from Jutulgryta and Autosub mission 382.

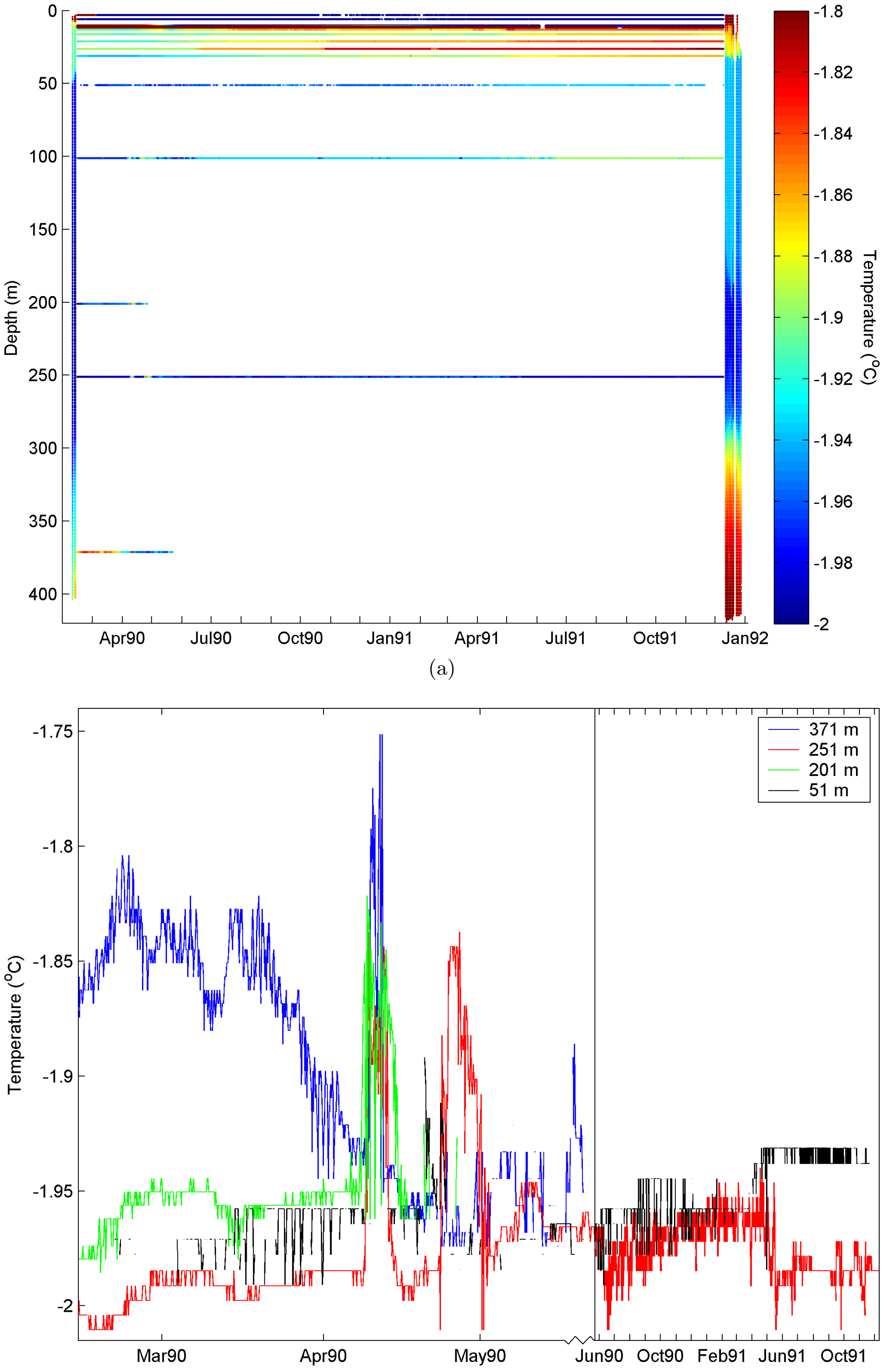

(a)

(b)

Figure 2.3: (a) Temperature records from CTD casts and IFIX mooring, Jutulgryta. (b) Temperatures from four temperature sensors at Jutulgryta. Note that the scale of the time axis changes after 21 May 1990.

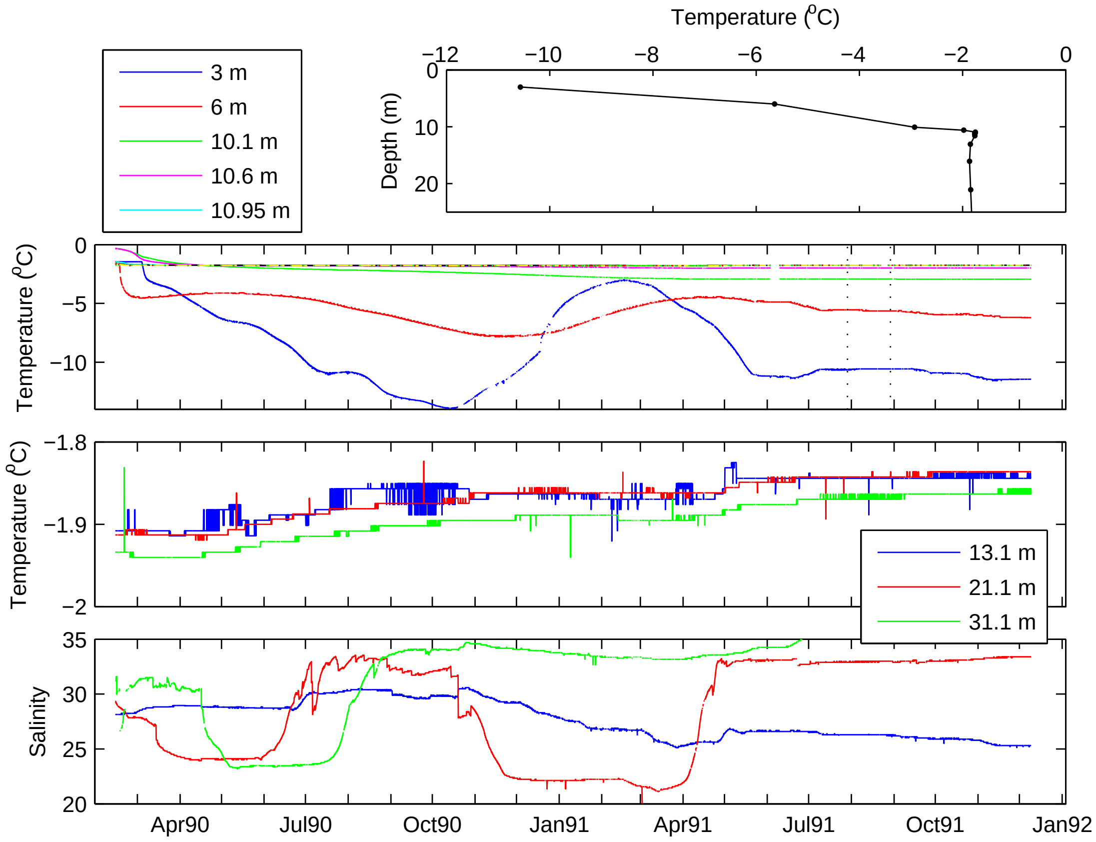

Figure 2.4: Near-surface measurements at Jutulgryta. The first plot shows average temperatures from the uppermost instruments, during the time interval marked with black vertical dotted liens in the second plot. The second plot shows temperatures from the uppermost instruments, including all measurements from the thermistor string — most of which are almost identical. The third and fourth plots show temperatures and salinities from the three uppermost instruments with working conductivity sensors.

up stabilizing near −3°C, while the lower stabilizes near −2°C. When the thermistor chain was deployed, the ice/ocean boundary was at 11.1 m depth (Østerhus and Orheim, 1994), so these two sensors are clearly inside solid ice, once it refreezes after deployment. Below this depth, the thermistors are in seawater and all have very similar signals, with temperatures around −1.9°C. However, it is notable that all of the thermistors from 11.1 m and down to 31 m show a gradual warming of around 0.05°C over the two years.

The salinities from the three uppermost conductivity sensors are shown in the lower panel in Figure 2.4. These show a fairly complex pattern; while the uppermost sensor starts having the lowest salinity of the three (as would be expected), it gradually rises until mid-October 1990, and then gradually decreases again. Much larger variation can be seen in the next sensor, at 21 m depth. Here the salinity decreases and remains quite low until June 1990, when it starts rising again. It then remains high until October 1990, when it falls rapidly, with some very sudden drops. Through the following summer salinities remain low, and then rise again in April 1991. They then remain steadily high until the end of the time series. Finally, the sensor at 31 m depth starts out reasonably high, but then suddenly falls in mid-April 1990. Salinities then rise again in July, and remain high, with a slight dip in the summer of 1991. In mid-June 1991 the salinities start to drift toward higher values, ending at an unrealistically high level above 39 psu at the time of recovery (beyond the scale of the plot).

Orheim *et al.* (1990) describe the ice as being 38 m thick, “a mixture of solid ice and freeze-on slush”. Also, during the drilling effort there was a large amount of meltwater on the surface (O. A. Nøst, pers. comm., 2008). We can therefore assume that while the sensors probably are surrounded by water, this is a complex area with various layers of ice (“false bottoms”), and possibly inter-connected pockets of sea water, with some connections to the surface of the ice shelf through cracks and moulins that drain the runoff into the rift. The sudden drops in salinity at 21 m depth could be from sudden pulses of surface runoff reaching the area around that sensor. Clearly, it is not connected directly with the area surrounding the conductivity sensors above or below. The increases in salinity could either come from brine rejection (from freezing occurring on the base of the solid ice above, caused by steady heat fluxes through the ice), or from mixing with higher-salinity water below. The quasi-annual signal indicates that surface runoff probably does control the salinity here. The deeper sensor, at 31 m depth, shows this signal in 1990, but then appears to stabilize in 1991 and remains high. The shallower sensor, at 13 m depth, displays less variability; perhaps this sensor is more fully enclosed by ice, with fewer connections to the surface, so it is less affected by the seasonal cycle of freezing and melting.

Chapter 3

Observations from Fimbul Ice Shelf: JR097

In February–March 2005 the third and final cruise of the Autosub Under Ice (AUI) program, JR097, took place on RRS James Clark Ross. The initial goal of the cruise was to go to Ronne-Filchner Ice Shelf and to send Autosub-2, an autonomous underwater vehicle (AUV), beneath the ice shelf to collect hydrographic and other data. However, as access to the ice shelf was restricted by sea ice near the eastern part of the Filchner ice front, the decision was made to follow the backup plan and go to Fimbul Ice Shelf instead. Details of the cruise can be found in the cruise report (Nicholls, 2005), but the events are summarized here.

The ship arrived at Fimbul Ice Shelf on Feb. 10, and began by undertaking a CTD and multibeam sonar (swath bathymetry) survey, and sending Autosub on a series of short test missions, during which it behaved satisfactorily. On Feb. 13 Autosub was launched on its first sub-ice shelf mission, mission 382; it returned to the rendezvous point with the ship after successfully completing its mission. The following day Autosub was again sent on a mission under Fimbul Ice Shelf, but this time it did not return (for more details, see the report of the inquiry into the loss: Strutt, 2006). It was not possible to recover the AUV, and the cruise continued, occupying CTD stations around Fimbul Ice Shelf, including some stations east of the ice tongue. Figure 3.1 shows the ship track and station positions around Fimbul Ice Shelf. The ship left Fimbul Ice Shelf on Feb. 21 and proceeded to the Brunt Ice Shelf to retrieve moorings deployed two years prior, near the ice front, starting on Feb. 24. On March 4, after further CTD and mooring work in the southern Weddell Sea, the cruise ended and the

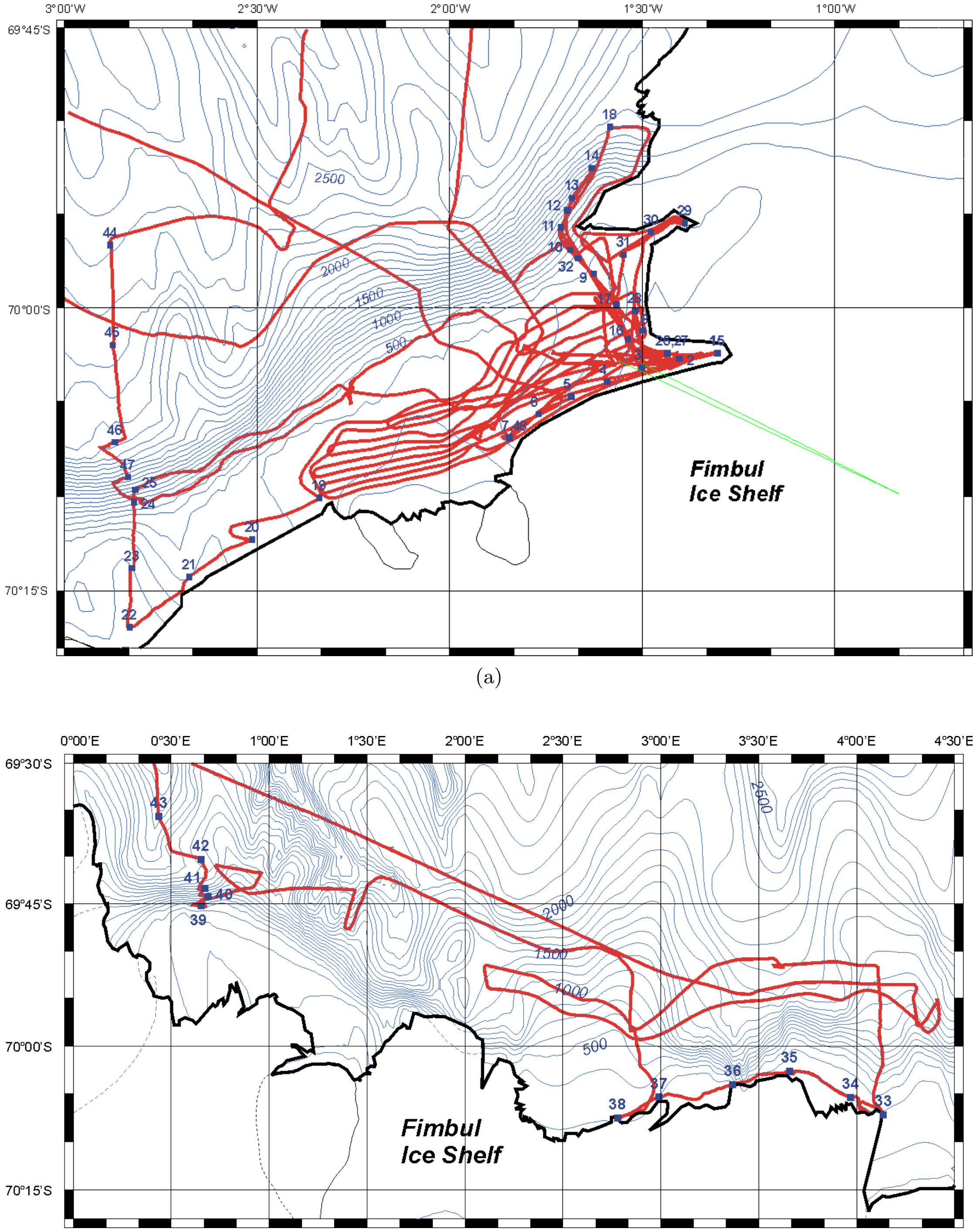

(a)

(b)

Figure 3.1: Overview of ship track and CTD station locations from JR097, (a) west and (b) east of the ice tongue (from Nicholls, 2005). Autosub's track on mission 382 is indicated in green. Note that the bathymetry data used in these figures are from an old version of GEBCO and may contain errors.

ship headed back toward Port Stanley in the Falkland Islands.

In addition to CTD profiles (described in Section 3.2.1), images of the seabed were obtained using a towed system (Jones *et al.*, 2007), and the ship's ADCP and multibeam sonar systems were running almost continuously. The swath data are described in Appendix A, while the ship's ADCP data are described in more detail by Walkden *et al.* (2009) and summarized below.

The rest of this chapter is structured as follows: first the instruments and methods used during the cruise are introduced. Then hydrographic data, both from Autosub and from the ship's CTD, are presented in Section 3.2, and current data and tidal model results are discussed in Section 3.3. Some of the results from the water samples taken on board are shown in Section 3.4, and measurements of the ice shelf base are discussed in Section 3.5. Finally, the results of an instrument mooring deployed during the time the ship was near Fimbul Ice Shelf are shown in Section 3.6.

3.1 Instruments and methods

3.1.1 Shipborne CTD

The CTD system on the James Clark Ross during JR097 consisted of a Seabird Electronics (SBE) 911+ system with dual pumped C/T sensors, an SBE 43 dissolved oxygen sensor, a Chesea Technologies Group Aquatracka III fluorometer and Alphatracka II transmissometer, a WET Labs BBRTD optical backscatter meter, an altimeter, and upward- and downward-looking 300-kHz ADCPs. The CTD was mounted beneath a 24-position carousel, with Ocean Test Equipment 10-liter Niskin bottles with external springs (model 110B-ES), which were fitted with specially vacuum-baked o-rings to avoid contamination of CFC samples (see Section 3.4.2). Salinity samples were processed on board, while δ^{18}O and CFC samples were sent back for later processing.

The CTD data were processed by Martin Price at the University of East Anglia. Preliminary alignment of the oxygen data with the C/T data, and compensation for the thermal mass of the conductivity cells were performed in the SBE Data Processing package. The data were then imported into Matlab, where outliers were automatically and manually flagged, and conductivity calibrations from salinity samples were applied. Finally, all measurements from the downcast were binned into 2-dbar pressure bins, where the median for each data channel was exported to a Matlab data file.

3.1.2 Autosub

Autosub-2 (henceforth referred to as Autosub) is an AUV that has been modified for use under ice (sea ice and ice shelves) for the AUI program. Most navigation while submerged is done with the help of one of the ADCPs, used as a Doppler velocity log, tracking either the seabed or the base of the ice shelf, whichever is in range. One advantage of Autosub is its capacity for carrying and providing power for a large scientific payload (Dowdeswell *et al.*, 2008). A schematic of the vehicle is shown in Figure 3.2. For mission 382 the following instruments were installed:

- CTD with dual T/C sensors and oxygen sensor (Seabird Electronics 9+)
- Downward-looking 150 kHz ADCP (RDI workhorse integrated with IXSEA PHINS fiber-optic gyroscop)
- Upward-looking 300 kHz ADCP (RDI workhorse)
- Upward-looking 200 kHz Multibeam Sonar (Simrad/Kongsberg EM-2000)
- Downward-looking sub-bottom profiler (Edgetech FS-AU)

A water sampler was also mounted during mission 382, but did not take any samples. The instruments used in this work are described below; further details can be found in the cruise report (Nicholls, 2005).

3.1.2.1 CTD

The CTD mounted on Autosub was a Seabird Electronics 9+ unit, fitted with dual temperature/conductivity sensors and an SBE43 oxygen sensor. All data were recorded in Autosub's logger and then extracted to a raw binary file that can be processed using SBE's “SBE Data Processing” software. The conductivities were advanced by 0.073 s and the oxygen concentrations were advanced by 6 s; then the conductivities were corrected for cell thermal mass effects. Rudimentary removal of outliers was performed, derived variables such as salinity were calculated, the data were averaged into 2-s bins and finally imported into Matlab for further processing together with the ADCP data. Unfortunately no post-cruise calibration could be performed on any of the sensors, as the sensors themselves were not available and no water samples

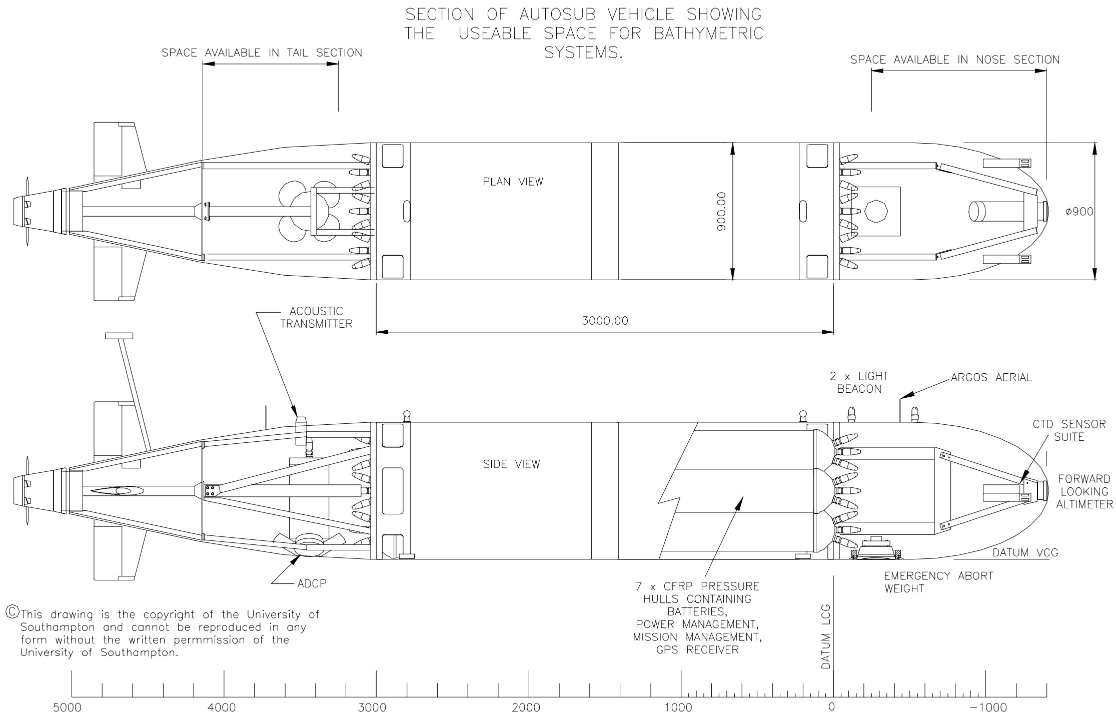

Figure 3.2: Schematic of Autosub-2. Dimensions are in mm. In addition to the base instrumentation shown, an upward-looking ADCP, water sampler, sub-bottom profiler, and upward-looking multibeam sonar were installed. Reproduced with the kind permission of the University of Southampton.

were collected by Autosub. This probably is not a serious problem for the conductivity or temperature sensors, but the dissolved oxygen values are probably not accurate, as the sensor calibrations may have drifted.

3.1.2.2 ADCP

The ADCP data from Autosub were processed in Matlab. The data processing software was originally written by Kate Stansfield for the Autosub science missions. Prior to the cruise it was updated and modified; the processing steps are more fully described in the JR097 cruise report (Nicholls, 2005). A brief summary is provided here.

After the CTD data are loaded into Matlab, the navigation data provided by the Autosub team are loaded. Then the ADCP data from Autosub's data logger, which are provided in 2-s bins, are loaded. The data are aligned and truncated to the time when Autosub was in the water, are rotated from a forward–starboard–up coordinate system to east–north–up, and are corrected for variations in the speed of sound. Points where Autosub was tracking the surface and bottom are identified, and flagged. Then the navigation data are re-integrated using dead reckoning with the updated

ADCP data between good GPS fixes at the surface. Next, Autosub's speed (as determined from bottom-tracking, surface-tracking, or water-tracking, in that order of priority) is filtered and subtracted from all the ADCP measurements to get absolute velocities. Finally, contaminated velocities close to the surface and bottom are removed, and velocities are mapped onto fixed-depth bins. Averages of all data are then calculated in 100-m segments along the track of the vehicle. The beam ranges from the upward- and downward-looking ADCPs are then transformed into geographical target coordinates.

Some problems were encountered with the ADCP data from under the ice shelf: backscatter was extremely low, yielding only a few valid bins in each profile, with significant noise in these data. Although the data are acceptable when several profiles are averaged (as would normally be done with ADCP data), the vertical coverage of the ADCPs was surprisingly limited, indicating that very few biological scatterers are present within the sub-ice shelf cavity. Bottom/surface tracking worked well, with strong returns from both the seabed and the base of the ice shelf.

3.1.2.3 Swath

The multibeam sonar data from Autosub were converted from Kongsberg's proprietary format to Matlab using software by Arthur Kaletzky, and manually edited by Martin Stott during JR097. The resulting data files have been referenced to the corrected positions from the ADCP/CTD data, and corrected for Autosub's depth, giving geographical coordinates for each beam target. The targets were then gridded on a $4 \times 4\,\mathrm{m}$ grid using mbgrid (Caress and Chayes, 2003, 2005, accessed 2006). The swath only locked onto the base of the ice shelf when the center beam was within a range of around 120 m. On mission 382 Autosub was programmed not to get closer than 100 m to the surface at any time, and was following the bottom on the outbound track and attempting to stay close to 100 m of the surface on the return track. This meant that the surface was in range during most of the returning track (with side beams up to 180 m away), and a few data were collected when entering the cavity.

3.1.2.4 Other instruments

The Edgetech FS-AU sub-bottom profiler was logging during the sub-ice shelf missions, but the bottom was at the limit of the range of the instrument, and very little

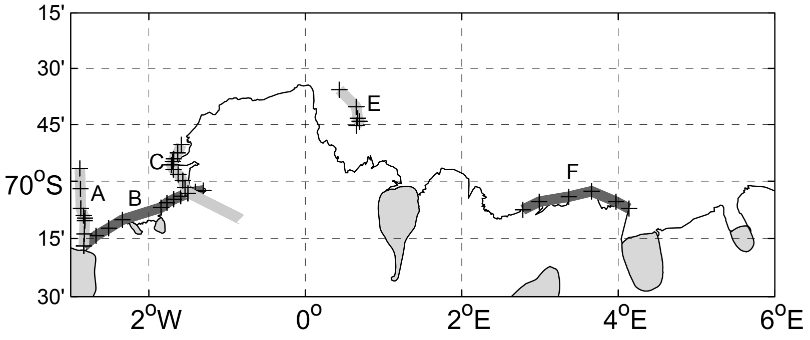

Figure 3.3: Map of CTD sections during JR097. The cross-shelf sections are in light gray, while sections along the ice front are in dark gray. Note that section C is extended to the south beneath the ice shelf by Autosub mission 382.

structure is visible in the data. However, the bottom itself is visible, so the data can be used to calculate the bottom depth as a single-beam downward-looking sonar; together with target ranges from the four beams of the downward-looking ADCP, these data have been used in Appendix A to map some features of the seabed beneath the ice shelf.

3.2 Water masses

3.2.1 Shipborne CTD

A total of 48 stations were occupied around Fimbul Ice Shelf. This yielded a total of 103 profiles, one of which is disregarded because of quality concerns. This was station 1, where we believe there was ice in the sensors; however, a second cast was later obtained at this position as station 15. Stations 26–28 were "yo-yo" stations, consisting of multiple casts in the same location, and are discussed further in Section 3.6. The stations and ship track are plotted in Figure 3.1.

The sections obtained during JR097 are shown in Figure 3.3. Sections along the ice front were obtained west of the ice tongue (section B), as well as near one of the eastern sills (section F). Cross-slope sections were taken along the western edge of the ice tongue (section C), farther to the west (section A), and east of the ice tongue (section E). The section names in Figure 3.3 use the same nomenclature as Price *et al.* (2008) and Walkden *et al.* (2009). Upward- and downward-looking LADCPs were used in addition to a CTD, and water samples were taken for salinity, CFC, and δ^{18}O analysis. The CFC samples, which I was responsible for collecting, are discussed in Section

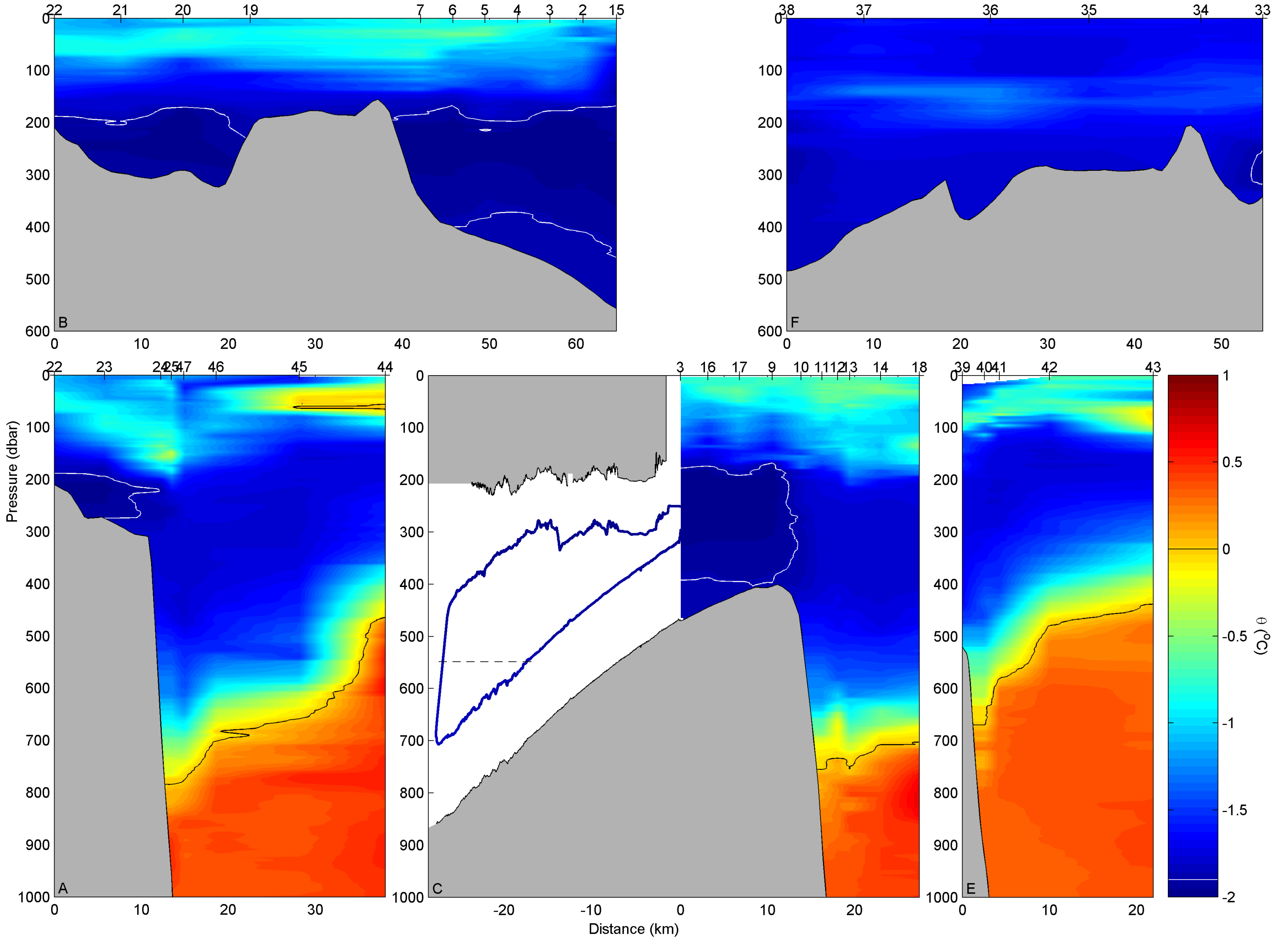

Figure 3.4: (a) Sections of potential temperature θ (°C) from JR097, including Autosub mission 382. The contour for $-1.9\,°\mathrm{C}$ is shown in white, and with a dashed line in section C, while the $0\,°\mathrm{C}$ contour is shown in black. The bathymetry is from multibeam sonar. The labels in the bottom left of the sections denote the section letter, as shown on the map in Figure 3.3.

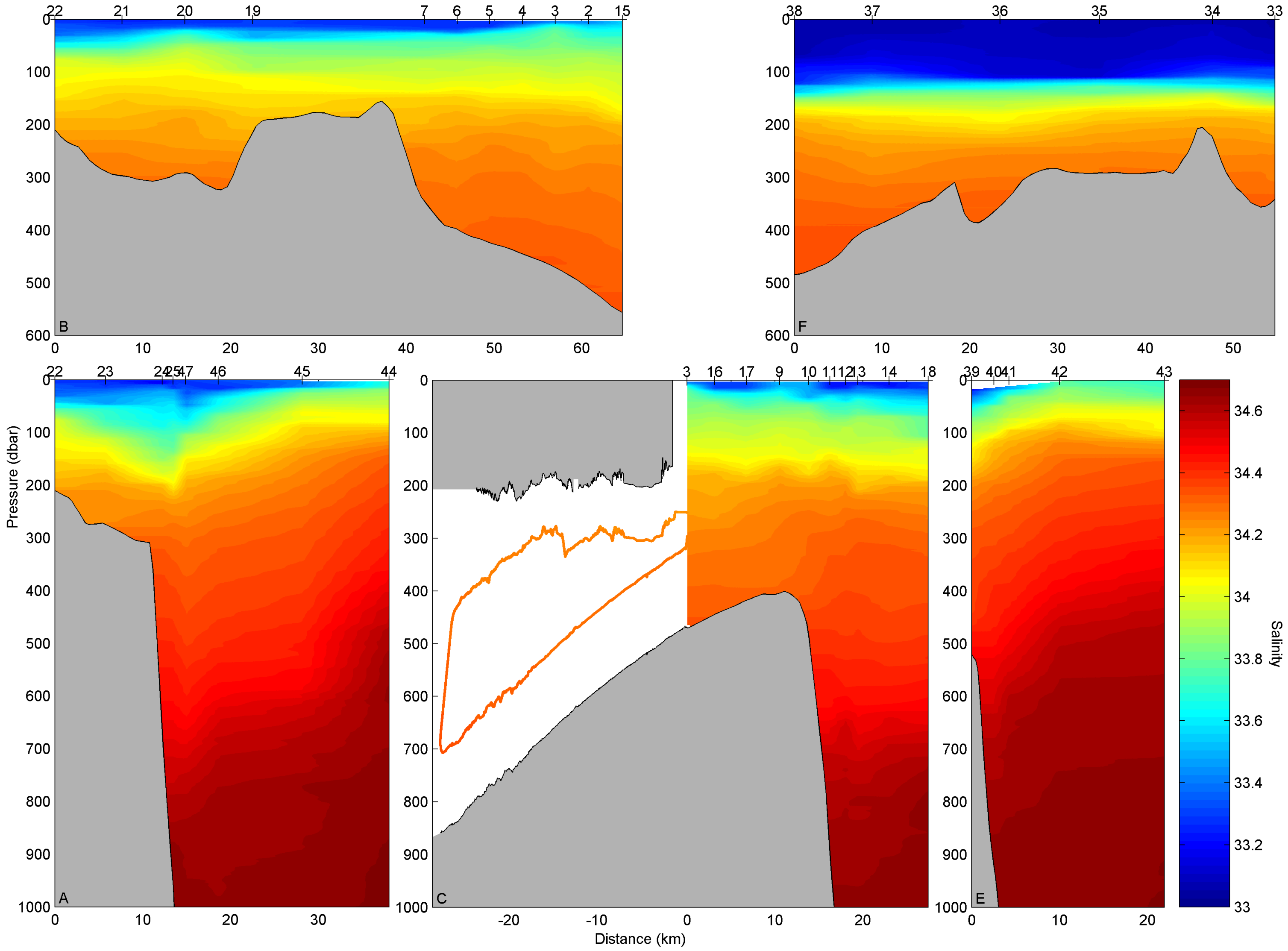

Figure 3.4: (b) Sections of salinity from JR097.

3.4.2. The oxygen isotope samples were analyzed by the group at UEA and described by Price *et al.* (2008), whose findings are summarized in Section 3.4.1.

Sections of potential temperature and salinity in the top 1000 m are shown in Figure 3.4; the two roughly zonal sections along the ice front, west and east of the ice tongue are in the top panels, with the three meridional sections across the shelf break in the bottom panels. Isotherms for $-1.9\,^{\circ}$C and $0\,^{\circ}$C are plotted on the temperature sections in white and black, respectively, to indicate the presence of ISW and WDW.

In section B, ISW ($\theta <$ surface freezing point, delineated by white lines in Figure 3.4a) is present throughout at depths between 200–400 m; in this area, the ice shelf draft is around 200 m. In section F there is some ISW in the easternmost station, which is close to a sill leading into the ice shelf. In addition, temperatures decrease toward the west, though the westernmost station has temperatures that are just above those for our definition of ISW. Unfortunately we could not continue the section farther toward the west because of the ice conditions; our westernmost station is in front of the next sill leading into the ice shelf cavity, though we do not have full coverage of that sill. Within the ISW layer there is clear stratification of salinities. As can be seen from the three meridional sections, ISW extends out to the shelf break; this is about 10 km from the ice front at section A (around $2^{\circ}\,40'$ W) and about 14 km just west of the ice tongue on section C. Interestingly, the southernmost stations on section C have temperatures above the surface freezing point near the bottom, beneath the ISW layer. This could imply that there is an inflow of warmer water (just above freezing) onto the shelf, probably through the deepest part of the sill, slightly east of the section.

The sections across the shelf break (A, C, and E) show that the interface between WDW and WW deepens toward the coast, intersecting the slope around 700–800 m depth. WDW in its unmodified form (defined as $\theta > 0\,^{\circ}$C, and delineated by black lines in Figure 3.4a) is only found on the slope below 750 dbar; no water near these properties was measured on the shelf.

3.2.2 Autosub

The most innovative use of technology on JR097 was sending Autosub beneath Fimbul Ice Shelf. This section describes the results from the one successful mission: mission

382. On this mission, Autosub started near the ice front, and was sent out in terrain-following mode, staying 150 m above the seabed until a predetermined waypoint was reached, approximately 25 km from the ice front. Then Autosub rose until it reached 400 m above the bottom and returned along its outward track. There was an overriding rule to stay at least 100 m below the surface, so as Autosub moved into shallower water it stayed in surface-following mode until another waypoint was reached, when it made a dive to 300 m above the bottom. Shortly afterwards the water shallowed enough that the vehicle once again went into surface-following mode. So in practice, Autosub remained 100 m below the ice shelf base for most of the returning track. After leaving the sub-ice shelf cavity, Autosub rendezvoused with the ship and was recovered, and all data were downloaded.

The CTD data gathered by Autosub during mission 382 are shown in Figure 3.5. The track can also be seen as a southward extension of section C in Figure 3.4. In Figure 3.5 the horizontal axis is kilometers from the turning point, farthest beneath the ice shelf. Panel (a) shows the meridional component of the ADCP data, with the first part of the ADCP data inset. In addition, the seabed depths from the downward-looking ADCP on the outbound track and the ice drafts from the upward-looking ADCP on the returning track are plotted. Panel (b) shows the detided median currents from the ADCPs; these use all the vertical bins, and one-km horizontal binning, to decrease the noise in the data. The tidal model described in Section 3.3.1, and the current measurements are described further in Section 3.3. Panels (c), (d), and (e) show salinity, potential temperature, and dissolved oxygen, respectively, with the outbound track plotted in red and the returning track plotted in blue, as in panel (b).

Beneath the ice shelf the prevalent water mass is ISW. When Autosub reached the maximum sill depth of approximately 570 m the temperature rose to the surface freezing point. At 657 dbar depth, just beyond the 4-km mark in Figure 3.5d, there was a sharp rise in temperature: 0.016 °C in just 24 m horizontal distance. This was accompanied by a similarly sharp drop in dissolved oxygen, and a change in current direction, as seen in the red plots in panels (e) and (b). Once the AUV surfaced to around 570 m temperatures again fell below the surface freezing point, and remained low on the rest of the outbound track. On this leg of travel, oxygen concentrations gradually increased, while salinities decreased, indicating a gradual increase in the fraction of meltwater. There are some patches of elevated oxygen concentrations, generally concurring with areas of slightly lower salinity.

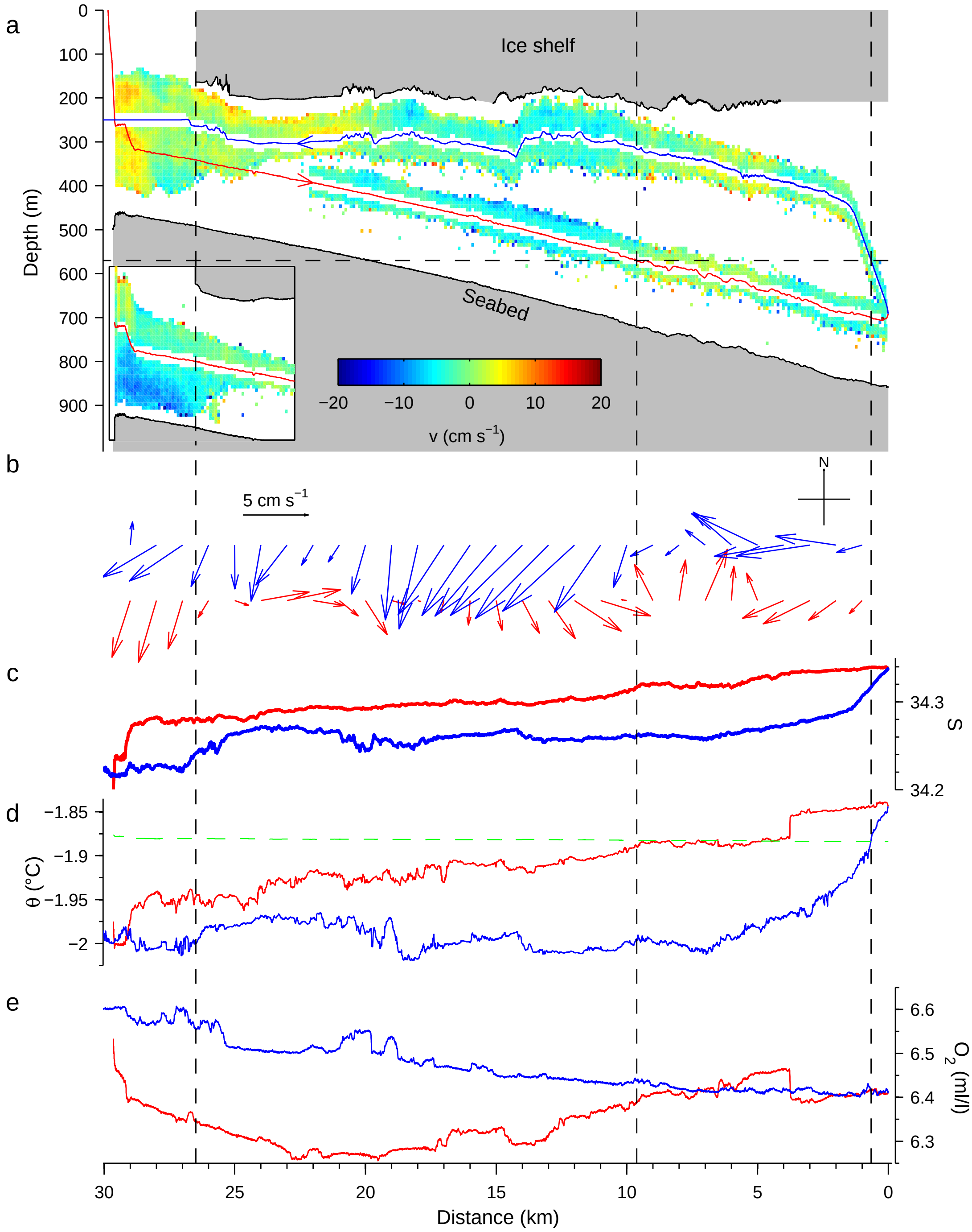

Figure 3.5: Hydrographic data from Autosub mission 382. (a) Northward component of the ADCP currents; measurements from the first part of the inbound track are plotted in the inset box. (b) Detitded current vectors — median across 1-km horizontal segments and all vertical bins. (c) Salinity. (d) Potential temperature, with the dashed green line indicating the freezing point at surface pressure. (e) Dissolved oxygen — uncalibrated. Data are plotted against the distance from the turning point; measurements from the inward leg are shown in red, while measurements from the returning leg are in blue.

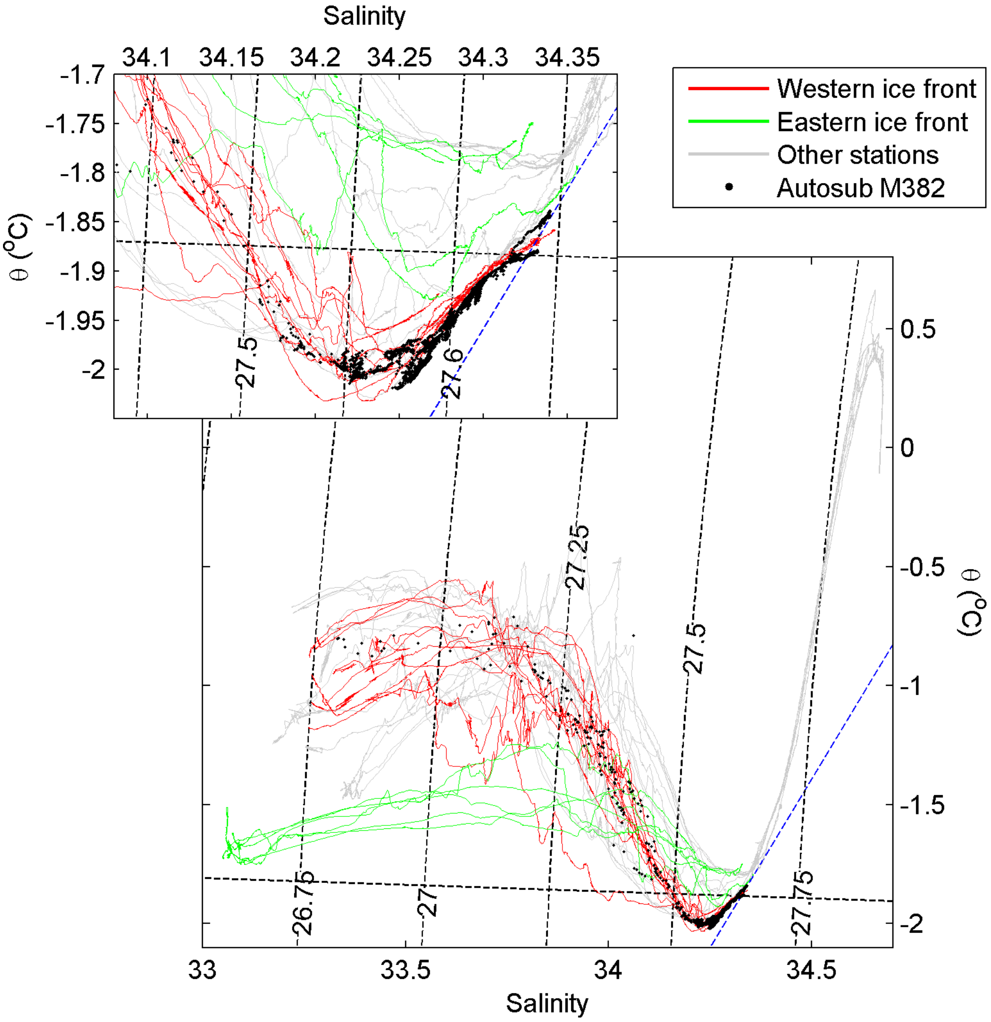

Figure 3.6: θ/S diagram from the CTD stations near Fimbul Ice Shelf, and Autosub mission 382. Contours of potential density at 0 dbar and the surface freezing point are indicated. The dashed blue line is a possible mixing line, with a slope of 2.83 °C psu^{-1}.

The smaller-scale features in temperature and salinity do not appear to be correlated between the inward and outward tracks, though the currents do hint at a barotropic current structure.

Figure 3.6 shows a θ/S diagram of the combined Autosub and ship-based CTD data, with the stations along the western and eastern ice fronts highlighted in red and green, respectively.

3.2.3 Discussion

The inset plot in Figure 3.6 shows that much of the cold water below the ice shelf is similar to water masses observed outside the ice shelf, along the western ice front. If we use the equation for a mixing line (see Section 1.3) assuming an ice shelf temperature of $-28\,^{\circ}\mathrm{C}$ (Østerhus and Orheim, 1994), and source water temperatures and salinities of $-1.72\,^{\circ}\mathrm{C}$ and 34.35, respectively, we obtain a slope of $2.83\,^{\circ}\mathrm{C}\,\mathrm{psu}^{-1}$. A line with this slope is drawn through the deepest, warmest water masses below the ice shelf. We can see that these could be formed from one of the stations on the eastern part of the ice front. However, there are no possible source water masses on the western ice front. Of course, our hydrographic data are merely a snapshot of conditions in February 2005, so it is possible that a source water mass can be found along the western ice front at other times of year, or, given the probable interannual variability, other years. The station that is the most likely source candidate is the westernmost station on the east, station 38, at depths around 420–480 m. It is possible that this water mass could enter the ice shelf cavity either through one of the eastern sills, or by flowing beneath the ice tongue and in through the main sill.

At salinities around 34.25, the θ/S curve appears to have bifurcated into two branches, one with higher and one with lower temperatures. Nicholls *et al.* (2008) interpreted the cluster of relatively warm water as a water mass that has been modified by passing beneath the ice tongue, as opposed to the colder water masses that have been modified at deeper parts of the ice shelf. This is supported by the dissolved oxygen data from Autosub, which have their highest values in this area. Interestingly, this water mass is found both near the ice front and near an area around 20 km from the turning point where the base of the ice shelf appears rougher from Figure 3.5a. In these rougher areas, the draft of the ice shelf is smaller. Since Autosub was following the surface, this means that the measurements were taken at slightly shallower depths. So it is possible that this water mass can be found higher in the water column in other places. It seems unlikely that any enhanced local melt rates in the rougher areas could explain this level of horizontal variation in meltwater content. However, the indicated changes in ADCP direction indicate that local variations in currents could account for the differences.

3.3 Currents and tides

3.3.1 Tidal model

Following the cruise to Fimbul Ice Shelf in 2005 a tidal model, part of the Oregon State University Tidal Inversion Software suite (OTIS: Egbert and Erofeeva, 2002),

Table 3.1: RMS misfits between currents measured from a mooring deployed near Fimbul Ice Shelf (described in Section 3.6) and a bottom pressure recorder deployed through a rift in the ice shelf (described further in Chapter 2), and corresponding tidal model predictions for these locations.

	Fimbul mooring currents (cm/s)	Jutulgryta bottom pressure (dbar)
OTIS medium	5.08	0.069
OTIS coarse	5.50	0.070
CATS02.01	6.07	0.071
TPXO6.2	6.92	0.103

was run to provide an estimate of the tides around Fimbul Ice Shelf for detiding current data from the ship and Autosub. The model runs were done using the matrix factorization solution of the linearized shallow-water equations, initially on a coarse $12 \times 5'$ grid, then on a finer $6 \times 2'$ grid, roughly equivalent to 3800 m resolution. The bathymetry (water column thickness) used was the one plotted in Figure 1.8, synthesized from GEBCO CE and swath bathymetry from JR097 outside the ice shelf cavity, and data from Nøst (2004) inside the cavity. The model was forced on the boundaries using results from the CATS02.01 tidal model (Padman *et al.*, 2002). A linear bottom drag parameterization, which was not modified beneath the ice shelf, was used. The misfits between the resulting models (at coarse and medium resolution), CATS02.01, and TPXO6.2 (Egbert and Erofeeva, 2002), and measurements from the lower current meter on the mooring described in Section 3.6 and the bottom pressure recorder data from Jutulgryta (see Chapter 2) are shown in Table 3.1. The RMS misfits of the currents are calculated as $\sigma_V = \sqrt{\frac{1}{N}\sum_{t=1}^{N}((u_m - u_o)^2 + (v_m - v_o)^2)}$, where u_m and u_o are modeled and observed current components, respectively.

Although King and Padman (2005) found that TPXO6.2 generally gave better results around Antarctica than CATS02.01, Table 3.1 clearly indicates that around Fimbul Ice Shelf CATS is the more accurate model of the two, and that using improved bathymetry under the ice shelf further improves tidal predictions beneath and around the ice shelf. Further improvements in accuracy could probably be obtained by assimilating the ship-borne ADCP data from JR097 and velocities from the mooring into the model using the inverse modeling techniques that Erofeeva *et al.* (2005) applied in the Ross Sea. However, considering the effort involved, the resulting improvements may not be significant (Erofeeva *et al.*, 2005, Padman, pers. comm., 2005). Even without these improvements, a subjective comparison between the tidal model results and the ship-borne ADCP data indicates that the medium-resolution OTIS run performs better around Fimbul Ice Shelf than CATS02.01 or TPXO6.2 (Walkden *et al.*, 2009, G. Walkden, pers. comm., 2007). Núñez-Riboni and Fahrbach (2010) found that the model from Robertson *et al.* (1998) provided a better fit to ADCP data directly north of the Fimbul Ice Shelf than either the newer CATS2008 or TPXO7.1 models.

The predicted tidal currents from the time of Autosub mission 382 are shown in Figure 3.7. As the model is barotropic, it computes depth-integrated transport, which is divided by the water column thickness to derive the velocity. Thus, any errors in water column thickness will lead to errors in the speeds. The currents used to detide the measurements from mission 382 use the water column thickness measurements from Autosub itself, while the other currents presented in Figure 3.7 use the model's water column thickness. These only differ significantly just around the ice front, where the lower resolution of the model bathymetry leads to minor differences. Mission 382 lasted around 12 hours, or close to one semi-diurnal tidal cycle. Tidal ellipses beyond the shelf break are almost collapsed onto a line, oscillating between westward and eastward currents. Beneath the ice shelf there is considerable flow through the eastern sills during much of the tidal cycle (with outflow from 12:00–15:00 and 22:00–23:00 and inflow from 16:00–21:00 in Figure 3.7. Currents appear to diverge when the tidal current flows beneath the ice tongue, converging again toward the downstream side. Beneath most of the ice shelf, currents are around 5–10 cm/s, with values slightly higher near the eastern sills, and lower in the southwestern part of the ice shelf.

3.3.2 ADCP measurements

Vertically averaged current measurements from Autosub are plotted as red vectors in Figure 3.7. Current measurements have a severely restricted vertical range beneath the ice shelf, most likely as a result of a severe lack of scatterers. So the plotted current vectors do not necessarily represent a barotropic flow beneath the ice shelf, but indicate currents near the AUV's depth at the time of measurement. From 14:00–16:00, when predicted tidal currents are eastward into the ice shelf cavity, measurements are also in this direction; similarly, from 19:00–22:00, currents are predominantly westward, out of the cavity. When the tidal vectors are subtracted from the measurements, the residual vectors (plotted in green) still appear to point in roughly

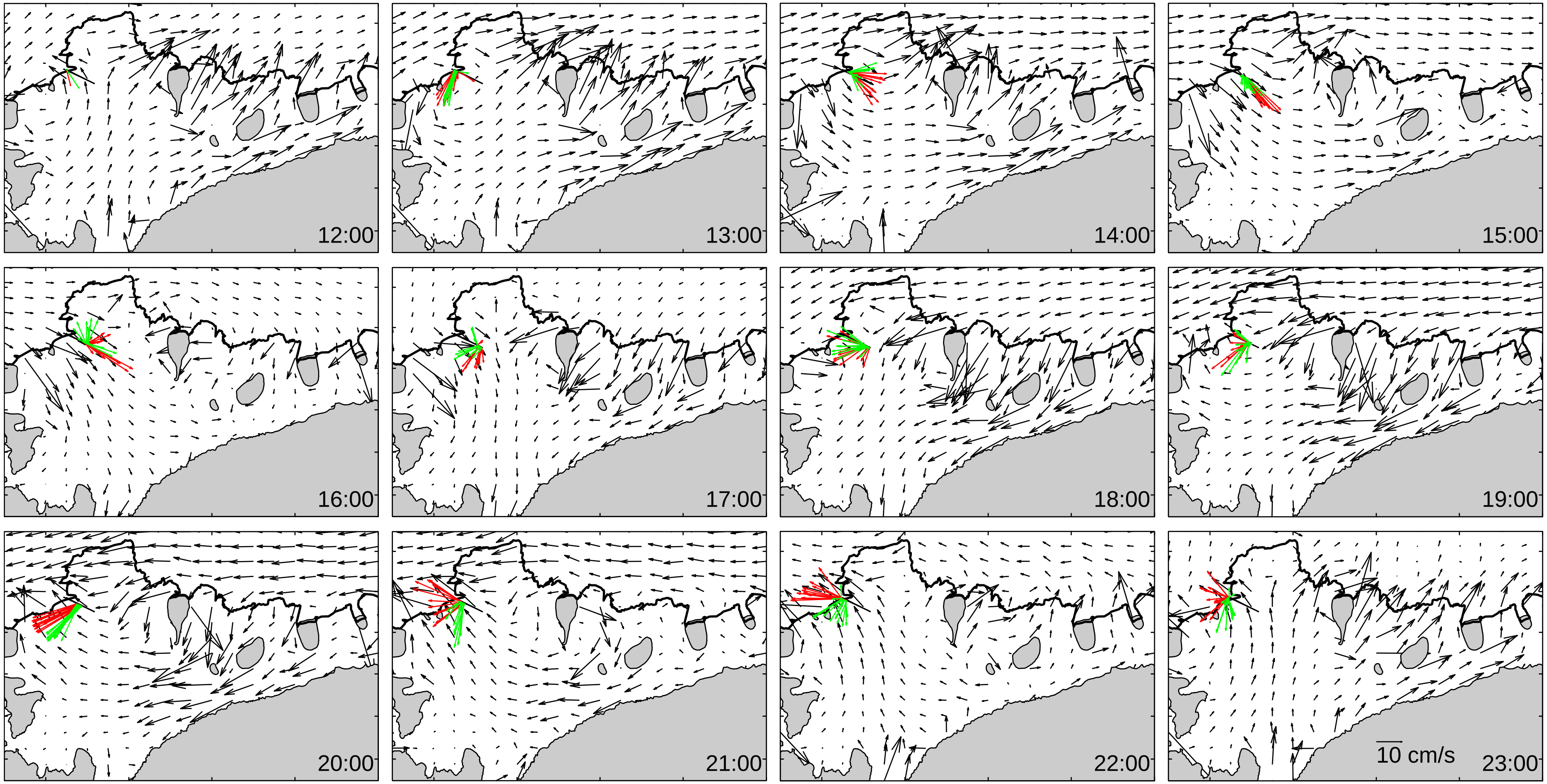

Figure 3.7: Tidal currents during mission 382, with current measurements superimposed. The times are on Feb. 13, 2005, and are all UTC; the current measurements plotted are from a one-hour window centered on the displayed time. Red vectors are current measurements from Autosub (from all depths), green vectors are the residuals after detiding using the transport fields from OTIS, divided by the water column thickness measured by Autosub to obtain velocities.

the same direction on the inbound track, while on the returning track, they point persistently toward SW. This current appears to be more intense nearer the base of the ice shelf.

3.4 Water samples

3.4.1 δ^{18}O data

Water samples for δ^{18}O are described by Price *et al.* (2008). Using a three-component mass balance between WDW, sea-ice meltwater, and glacial meltwater, they determined the fractional composition of water at various depths. While large amounts of sea-ice meltwater were found in the upper water column (down to 200 m depth), there was very little glacial melt. However, at 200–400 m depth there was a larger contribution of ice shelf water west of the ice tongue, with a maximum near the shelf break. At 3° W this meltwater was considerably more diffuse, and appears to have spread farther out beyond the shelf break. Since some of the meltwater was found quite far north along the western side of the ice front, they concluded that this must have melted from the ice tongue itself rather than from the main cavity.

3.4.2 CFC samples

On JR097 120 CFC samples were taken in total; 84 of these were from the area around Fimbul Ice Shelf, yielding 74 valid measurements. In addition, 28 valid samples were obtained from the Filchner Sill area. The samples were collected from the CTD rosette using 10-liter Niskin bottles with external springs; the o-rings were baked prior to the cruise to remove contamination with CFCs. The samples were then drawn straight from the Niskin bottles through steel tubing into glass ampoules, where they were flame sealed while ultra-pure nitrogen was blown through the headspace. After the cruise, the samples were shipped to Lamont-Doherty Earth Observatory, where they were processed courtesy of Dr. Bill Smethie. The sampling and analysis methods used are described in more detail by Smethie *et al.* (2000). Because the atmosphere of the James Clark Ross was less contaminated than a submarine, not all the precautions described in that paper were followed; however, errors from contamination from the surrounding air during sampling were probably minimal. One problem that did occur was that the seals on some of the ampoules shattered during analysis; this meant that

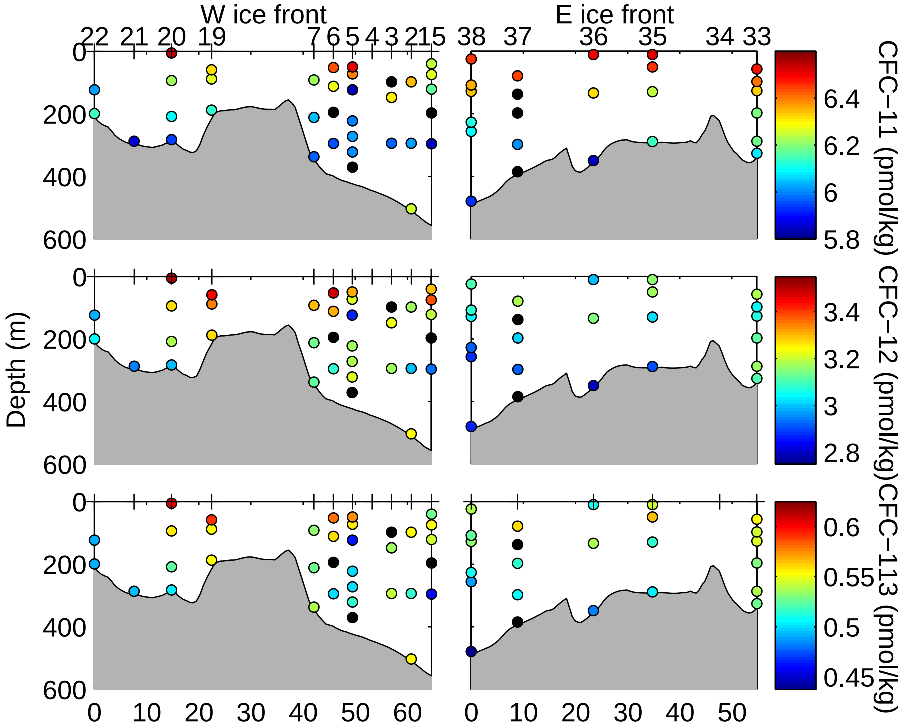

Figure 3.8: CFC concentrations along the front of Fimbul Ice Shelf. The black dots are invalid samples. The sections are the same as those in the upper panels of Figure 3.4.

the headspace volume could not be determined accurately enough to give the highest possible precision (W. Smethie, pers. comm., 2006,2009). The errors in the measurements are estimated to be of order 5%.

Past studies of CFCs around ice shelves have been used to determine the residence times under the ice shelf (Gammelsrød *et al.*, 1994, Smethie and Jacobs, 2005) and CFC saturations on the continental shelf (e. g., Klatt *et al.*, 2002). Unfortunately the residence times under Fimbul Ice Shelf are considerably shorter than under Ross Ice Shelf; this precludes determining the residence time under the ice shelf, as the differences between the water masses to the east and the west of the ice shelf are small compared with the scatter of the measurements. The CFC concentrations to the west and east of the ice tongue are shown in Figure 3.8.

3.4.2.1 Surface saturations

As would be expected, the highest CFC concentrations are found in the upper water column, where the water has most recently been ventilated. By calculating the equilibrium CFC solubility of the CFCs in seawater (Warner and Weiss, 1985, Bu and Warner, 1995), given the atmospheric concentration in Feb. 2005, derived from

Table 3.2: CFC saturations and ratios for surface water (upper 100 m), WW, WDW, and ISW from around Fimbul Ice Shelf. Median values are given, with standard deviations in parentheses.

	Saturation (%)			Ratio		
	CFC-11	CFC-12	CFC-113	CFC-11/12	CFC-11/113	CFC-12/113
Surface water						
West	88.7 (2.2)	88.3 (3.8)	77.5 (4.5)	2.07 (0.05)	11.75 (0.45)	5.75 (0.10)
East	86.3 (0.5)	80.2 (2.0)	69.6 (2.5)	1.89 (0.06)	11.34 (0.35)	5.89 (0.19)
North	91.0 (0.5)	85.0 (2.6)	70.9 (7.5)	2.03 (0.06)	12.88 (1.21)	6.11 (0.69)
Overall	88.0 (2.3)	85.0 (5.2)	71.8 (5.6)	1.99 (0.10)	11.50 (0.80)	5.79 (0.38)
WW	78.4 (2.6)	73.2 (4.5)	62.9 (6.0)	2.07 (0.08)	12.12 (0.90)	5.87 (0.46)
WDW	18.3 (8.5)	16.0 (8.5)	13.6 (5.6)	2.16 (0.11)	14.72 (2.10)	7.09 (1.06)
ISW	79.6 (1.3)	79.0 (2.7)	66.2 (3.0)	1.94 (0.06)	11.70 (0.47)	5.94 (0.20)

the annual southern-hemisphere concentrations from (Walker *et al.*, 2000, southern hemisphere values extrapolated to Feb. 2005), we can find the saturation of the three chemical species. Median and standard deviation values for the three sections around Fimbul Ice Shelf are given in Table 3.2.

It is surprising that the surface water on the eastern side of the tongue is about 8% less saturated with CFC-12 and CFC-113 than on the west, while its CFC-11 saturation is comparable. The difference in saturation can be explained by the higher ice concentration to the east; in comparison, Gammelsrød *et al.* (1994) found surface saturations of around 90% for CFC-11 and 85% for CFC-12 in the southern Weddell Sea. However, there is no obvious reason why the ratios should be similar in the west, and different elsewhere.

After the James Clark Ross left the Fimbul Ice Shelf area, it continued into the southern Weddell Sea, near Caird Coast, where a section was made from Caird Coast towards NW into Filchner Depression. In addition to CTD casts, CFC samples were collected from the upper 20 m of the water column. The conditions along the section varied from open water nearest the coast to full sea ice cover in Filchner Depression. The CFC saturations and sea surface potential temperature as a function of distance along the section (from the station nearest the coast) are shown in Figure 3.9. In addition, sea ice fractions from visual observations are shown in the lower part of the figure.

As the sea ice cover increases away from the coast, and shifts towards thicker ice classes, the surface temperatures decrease toward the freezing point, showing the limit of the coastal current. In the well-ventilated ice-free region, CFC-11 saturations are over 90%, while CFC-12 is closer to 85% and CFC-113 is just over 70%. Moving

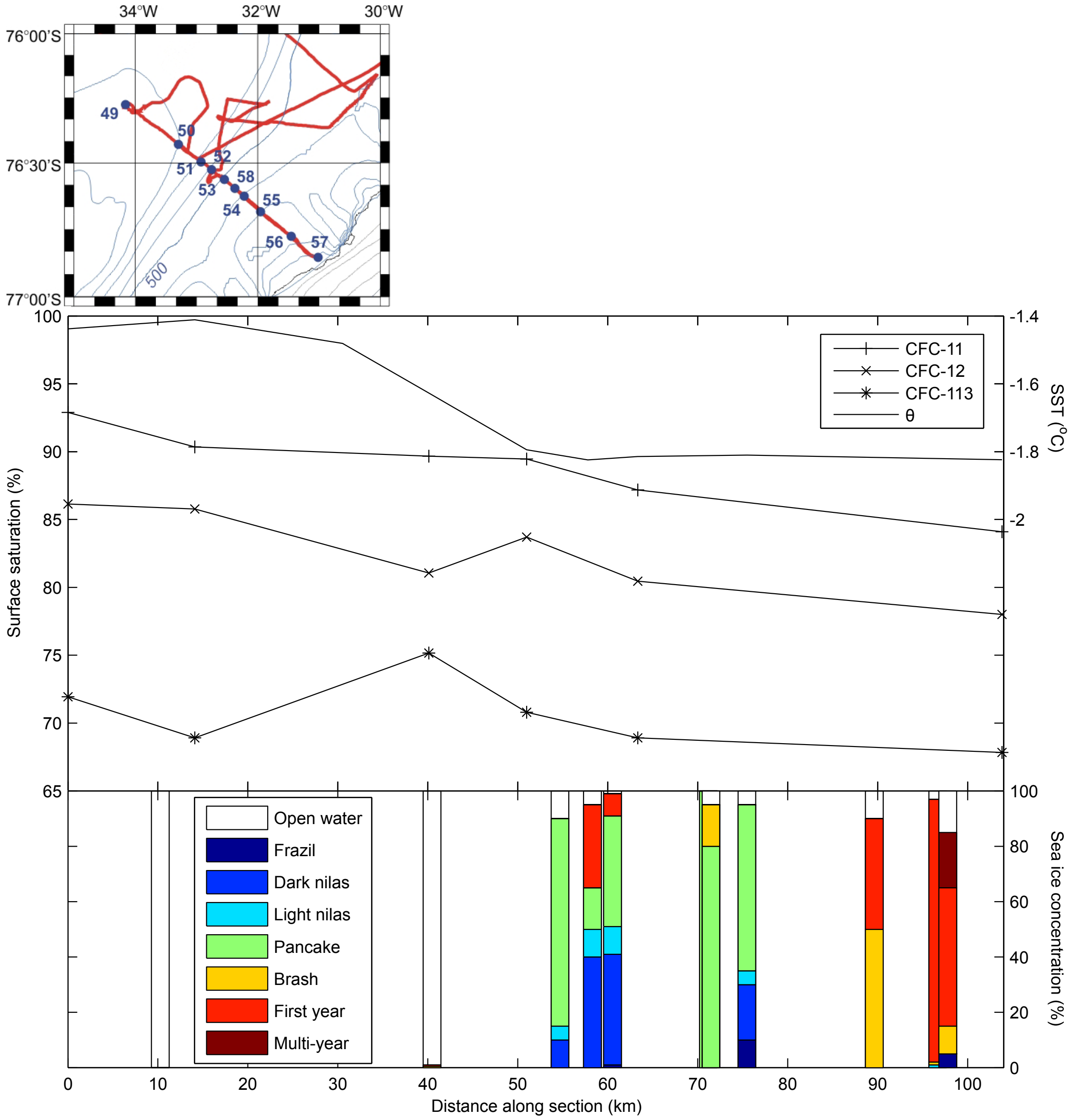

Figure 3.9: Surface CFC saturation and potential temperature in a section heading NW from Caird Coast as shown in the map, into increasing sea ice. Sea ice concentrations and composition (from visual observations) are shown in the lower part of the figure.

into the ice-covered region, the CFC-11 saturation decreases steadily. The decrease in CFC-12 saturation is slightly noisier, while we observe the highest CFC-113 saturation near the ice edge. This can only be attributed to measurement errors. It could be interesting to see if the insulating effect of sea ice cover impacts the properties of bottom water formed in the Weddell Sea. However, that is well beyond the scope of this thesis.

3.4.2.2 Conclusions

It is clear from Figure 3.8 that CFC concentrations to the east and west of the ice shelf do differ slightly. On the western section, the lowest concentrations are found in the ISW layer. On the eastern side, the CFC-11 concentrations are higher than on the west, while the CFC-12 concentrations are lower and the CFC-113 concentrations are similar to the western side.

The saturations measured during JR097 are comparable to previous measurements from Gammelsrød *et al.* (1994), and indicate that equilibration with atmospheric CFC concentration occurs more slowly for CFC-12 than for CFC-11, with CFC-113 even slower. Variations in near-surface CFC saturation around Fimbul Ice Shelf are likely caused by variations in sea ice cover, though the relative differences in saturations between chemical species remains unexplained.

The samples taken within the ISW layer have concentrations higher than those in the WW, but below those of the surface water. We can assume that the glacial meltwater is completely CFC-free; since there is no more than 1.2% meltwater in any of the sampled water masses (Price *et al.*, 2008), the reduction in concentration from the addition of meltwater is smaller than our sampling error. One constant even if meltwater is added is the ratio between chemical species. The ratios found in ISW are closest to the properties of surface water near the ice shelf, though they are not (statistically) significantly different from WW. WDW does have significantly different properties, both in saturation and in ratios, as a result of its much longer age since ventilation. However, given the large uncertainties of these measurements, we can still not conclude much about the composition of our ISW, except to say that at the end of our error bars it cannot contain more than $\sim 20\%$ unventilated WDW. However, such a large fraction of WDW would, in any case, be quite unlikely.

3.5 Ice shelf base

On the returning track from mission 382, Autosub stayed around 100 m below the base of the ice shelf, where the surface was within the range of the multibeam sonar. These data are shown in Figure 3.10b; a subsection of the profile is visualized in 3-D in Figure 3.10a. While most of the ice shelf is smooth, as generally would be expected, there are several large areas with much rougher ice (e.g. the areas around the 13, 18, 20, and 26 km marks).

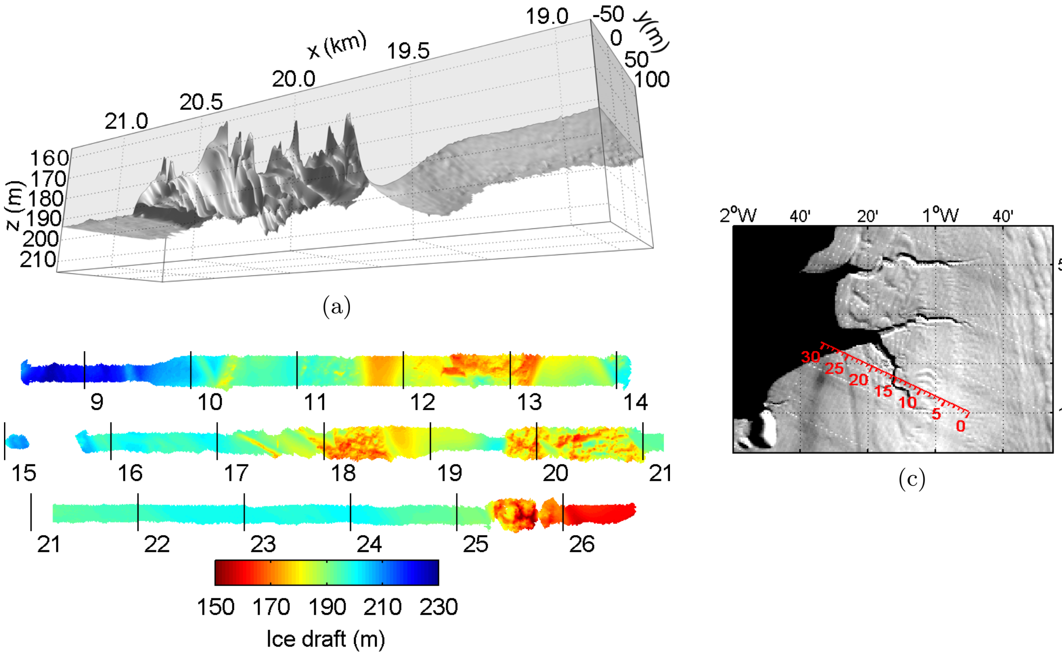

(a)

(b)

(c)

Figure 3.10: (a) Visualization of the ice shelf base; x is the distance from the turning point in the direction of travel, y is the cross-track direction. (b) Draft of the ice shelf along Autosub's returning track; the distances are in km. (c) Detail of a MODIS image of Fimbul Ice Shelf taken on 1 April 2005 08:55 UTC, with enhanced contrast to show flow traces and rifts.

Figure 3.10c shows a visible-light image of the surface of the ice shelf with Autosub's track superimposed. Contrast has been enhanced on the image, to make the surface features stand out more clearly. On this type of image, the reflected brightness is a function of the surface slope and its angle relative to the sun's position (Dowdeswell and McIntyre, 1986). So although the darker areas are not actual shadows, they will be caused by areas tilting away from the sun. As the image was taken at 8:55 in the morning, the scene was illuminated from the NE. A higher-resolution image of the area around the rift is shown in Figure 3.11, with the swath data from Autosub superimposed. Here an area of open water can be seen in the top left, with two rifts extending southward and eastward into the ice shelf. These rifts are filled with multi-year marine ice, which appears darker and much less smooth in the images.

The rough areas observed by Autosub correspond quite well to some of the flow traces in the images: lines mostly parallel to the flow of the ice shelf (Fahnestock *et al.*, 2000). The exact mechanism behind the formation and persistence is not well understood, but they are a ubiquitous feature of many ice shelves (Glasser *et al.*, 2009).

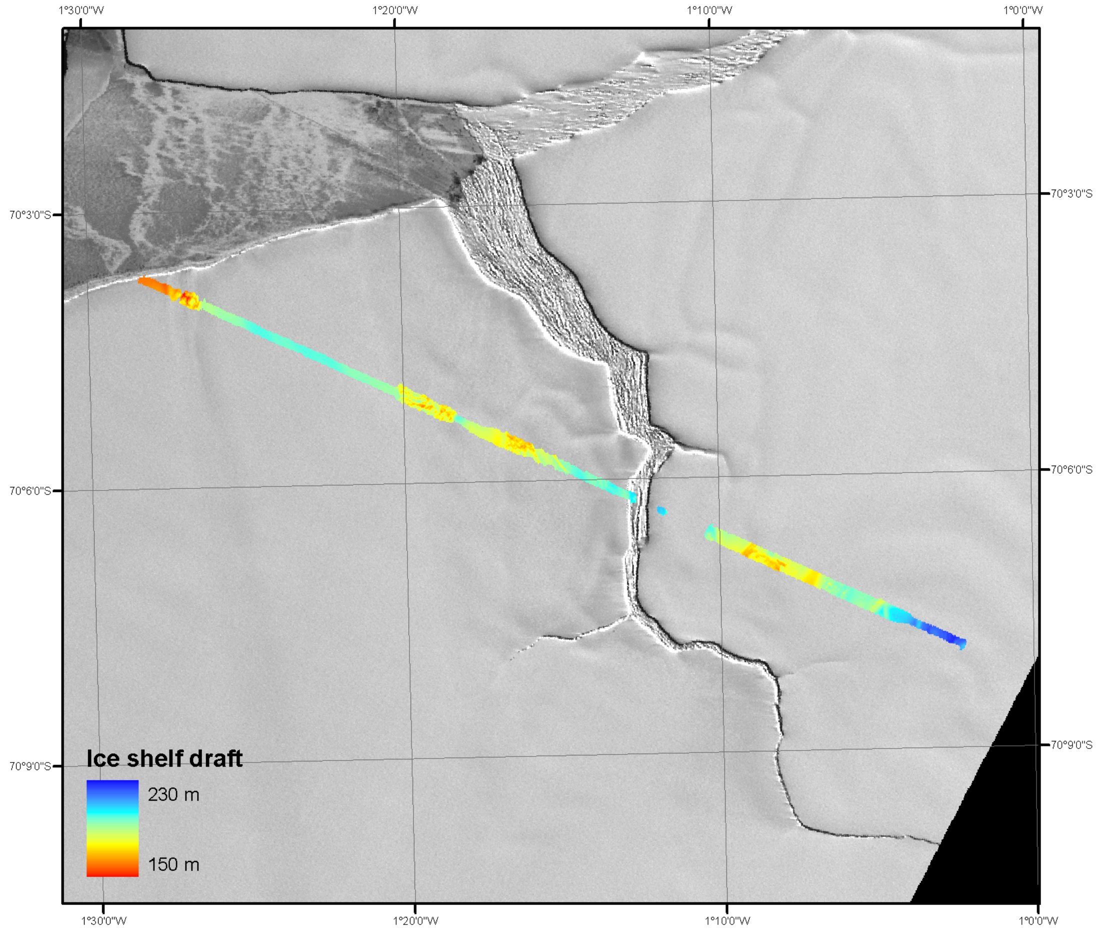

Figure 3.11: Satellite image from Aster, Jan. 4th, 2005 at 08:50 UTC, with ice shelf draft from Autosub superimposed. The background image comes from channel 2 (red, λ = 630–690 nm) and has been plotted using a non-linear color scale, to enhance the contrast of the flowlines.

They are most commonly found downstream of faster-flowing ice streams. One theory for their formation is that they form when ice streams are compressed laterally, and stretched longitudinally (as when an ice stream in pressed through a narrow gap); another is that they originate as shear zones separating adjacent ‘flow units’ within ice streams — but velocity gradients across them have not been observed on ice shelves (Glasser *et al.*, 2009).

In Figure 3.10b there are two gaps evident in the profile. The first, just after 14 km, is caused by Autosub diving at a pre-arranged waypoint. After a short distance of following the bottom, the surface comes back into range again, but then the track passes under a large rift in the ice shelf (at the 15.5 km mark). At this point neither the multibeam sonar nor the upward-looking ADCP receives any returns from the ice base, so we do not know the depth of this rift.

While most of the base of the ice shelf is smooth, a large part appears not to be, and this is probably significant in determining the friction coefficient used in numerical models such as frazil plume models (e.g., Holland and Feltham, 2005) and general ocean/ice shelf models (e.g., POLAIR, see Chapter 4). As it appears that the areas beneath flow traces are measurably rougher, this could be used to improve estimates of mixing beneath ice shelves, based on the extent of flow traces as observed in satellite imagery.

3.6 Mooring

A mooring was deployed during JR097 just west of the sill (see Figure 1.8), with two current meters, at 20 and 140 m above the bottom (in 347 m of water). During deployment the vane of the upper current meter got tangled in the mooring line, tilting the instrument. This jammed the compass, resulting in directions that are invalid, although the speeds are still usable (both current meters were equipped with Savonius rotors, which are independent of the heading of the current meter). The resulting data are shown in Figure 3.12, along with CTD profiles from the deployment and recovery of the mooring.

The temperatures from the two current meters are almost anticorrelated, and show a semidiurnal signal in the beginning, becoming more diurnal toward the end. Minimum temperatures are generally lower at the upper current meter, which appears to be in the outflow from under the ice shelf. At the bottom, minimum temperatures are slightly higher and the range of temperatures is much narrower. On Feb. 15 and 16 there are two episodes where significantly warmer water reaches the upper current meter. There were gale force easterly winds around Fimbul Ice Shelf on Feb. 15, decreasing in strength on Feb. 16, and generally the mixed layer deepened on this day (Stansfield and Lane-Serff, 2005). So it appears that the warmer surface water that was seen in the CTD cast on Feb. 12 was mixed down past the level of the upper current meter. Between the deployment and recovery, the surface layer changed significantly, becoming much cooler and fresher across the upper 130 m, most likely as a result of this event.

The cooling of the surface layer between the two profiles is equivalent to an average heat flux of order 350 W/m^2 over the nine days when the mooring was deployed

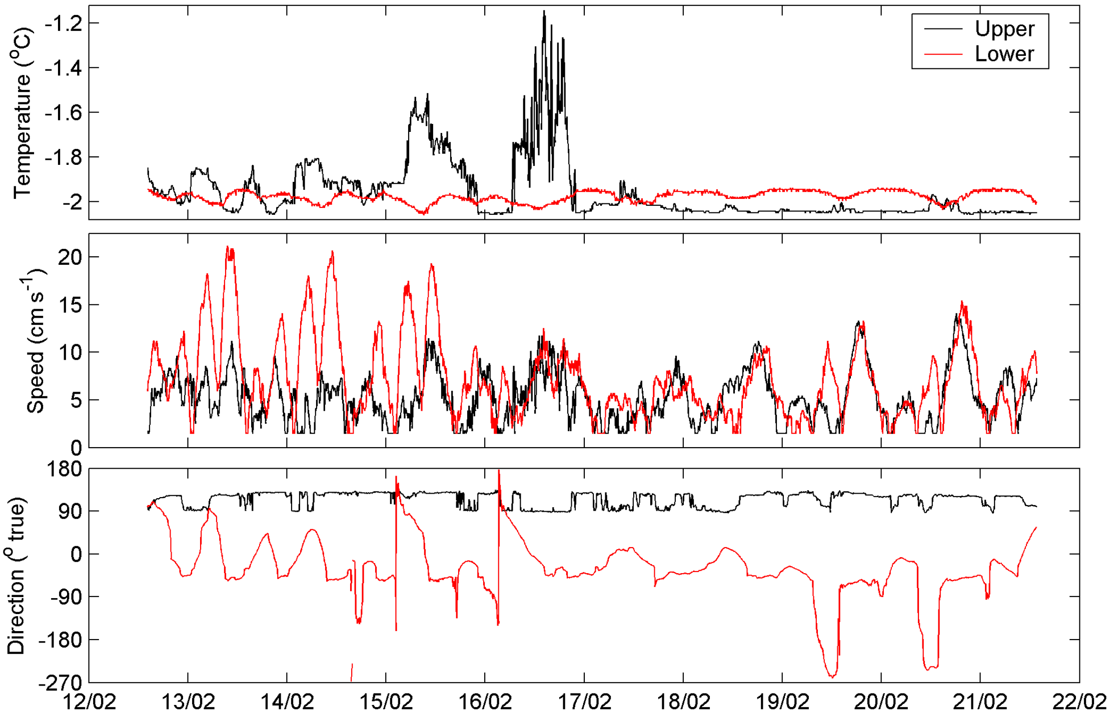

(a)

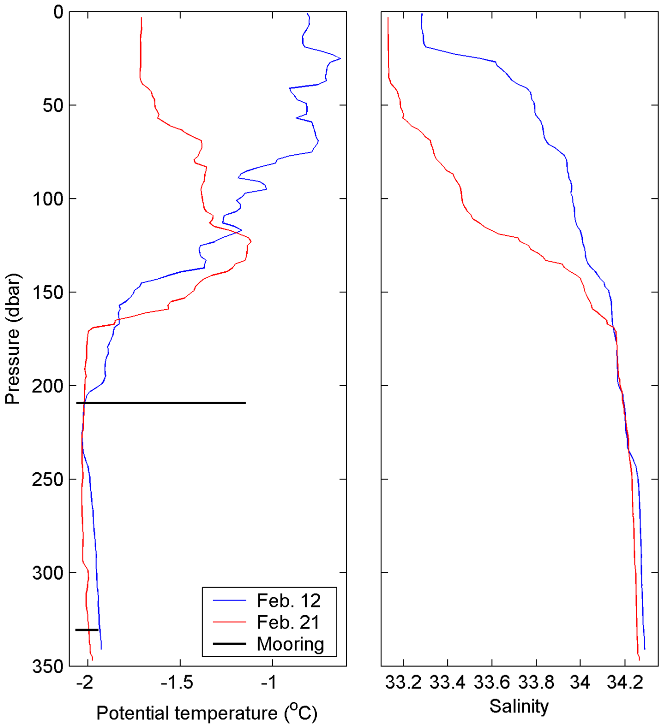

(b)

Figure 3.12: (a) Temperatures, speeds, and directions from the mooring off Fimbul Ice Shelf. (b) Potential temperatures and salinities from CTD profiles taken at the time of the deployment and recovery of the mooring, with the temperature ranges measured by the current meters shown as black horizontal lines. Dates are in 2005.

(i.e. a net heat loss from the ocean to the atmosphere). Winds measured from the ship during the mooring deployment averaged around 8 m/s, with a mean air temperature of −4.5 °C. This heat flux is quite high; for comparison Fiedler (2010) found heat fluxes of order 100–250 W/m^2 in the Ronne Polynya, but with higher air–ocean temperature differences and stronger winds. In contrast, Budillon *et al.* (2000) found net downward summer heat fluxes in the approaching 200 W/m^2 Ross Sea, largely caused by the increased shortwave radiation — while the sensible heat loss was of order 30–85 W/m^2. One clear indication that the changes are not caused by purely convective processes is the salinity difference: to freshen the profiles by the amount observed would require a freshwater flux above 100 mm/day over nine days — clearly an unrealistic amount.

On Feb. 15–16 the ship was on the west side of the ice tongue, waiting for the weather to improve and doing ‘yoyo casts’. Three such stations were occupied: 26, 27, and 28. Stations 26 and 27 were at the same location, in the first rift in the ice tongue, while station 28 was about four nautical miles to the NW, between the first and second rifts (see Figure 3.1a). The temperature profiles from these casts are plotted in Figure 3.13, along with temperatures and salinities from the depths of the current meters on the Fimbul mooring. While we cannot compare the temperature and salinity time series from the two locations directly, the temperatures from station 28 show considerable variability. Qualitatively they do seem similar to the measured variations from the mooring on Feb. 16, lending further credence to the interpretation that the temperature excursions at the upper current meter come from deepening of the thermocline during this episode.

Again, the heat gain during stations 26–27 and subsequent heat loss observed during station 28 are too large to be contributed to purely convective processes (they are equivalent to heat fluxes of order 3000 W/m^2). A much more probable explanation is enhanced downwelling as a response to the strengthening of the winds during the gale, and a subsequent relaxation as winds started to decrease during station 28.

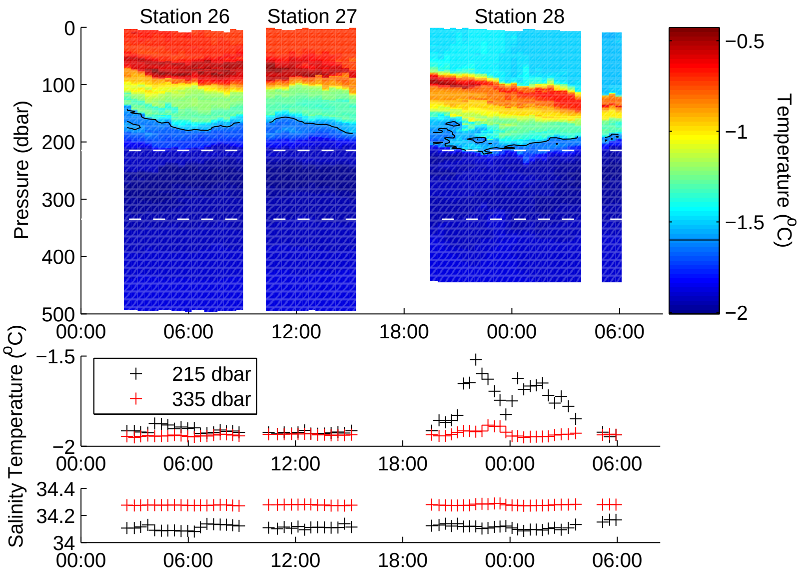

Figure 3.13: Temperature profiles from the 'yoyo' stations on Feb. 15–16, 2005, along with temperatures and salinities from the depths of the current meters on the Fimbul mooring.

Chapter 4

Modeling using POLAIR

While the observations beneath and around Fimbul Ice Shelf have provided insights into conditions beneath and surrounding the ice shelf, they still leave many unanswered questions. The moored observations show interesting variability, but only at a fixed point, while the measurements from Autosub and ships provide good spatial coverage, but only at a snapshot in time — and only at times of the year when ships are able to reach the ice shelf.

To supplement these sparse data, and to help explain the observations, a numerical model has been used to simulate the circulation beneath and surrounding the ice shelf. Smedsrud *et al.* (2006), henceforth referred to as LHS2006, previously applied the POLAIR modeling system (Holland and Jenkins, 2001) to this region, so the work presented in this chapter builds on their model study, but includes many modifications and improvements, including changes to the model domain and to the forcing applied.

The model is used to help explain the response of the slope front to changes in wind patterns, which in turn can affect the inflow of MWDW to the cavity. In addition, using annual and multi-year forcing we can gain more insights into the variability within the cavity. And the dependence of basal melt rates on changes in the forcing is also explored, as this can help explain previous modeling results, which show very high melt rates beneath the ice shelf.

LHS2006 used highly simplified forcing consisting of a constant easterly wind stress, decreasing as a cosine from the southern edge of their domain toward the north. With this forcing they found that WDW entered the ice shelf cavity, causing a net melt averaging 1.9 m/year, with most melting taking place around the central keel of the ice shelf. This is less than predicted in other models (e.g. Hellmer, 2004), but would still cause a significantly negative mass balance (Smedsrud *et al.*, 2006, and calculations in Section 4.4.4).

Preliminary runs using the model setup from LHS2006 with closed boundaries gave unrealistic results. The flow recirculated back toward the ice shelf from the northern boundary in the middle of the domain without being fully restored to the boundary conditions. To solve this, cyclic boundary conditions were chosen instead, such that water could flow uninterrupted through the domain from east to west, albeit with some restoration of temperatures and salinities on the boundary. In addition, the original model did not include any time variation in the wind forcing, and tides were not included. These issues have been addressed, to provide new insights into the circulation under the ice shelf.

Both the IFIX data set (Section 2.2) and the temperature time series from Fahrbach *et al.* (1994) show warm water flowing onto the shelf in pulses. To see if the model could provide decreased, more realistic levels of warm inflow to the ice shelf cavity, time-varying wind forcing was added. In addition, adding tides to the model runs can be used to help detide and interpret the ADCP and LADCP data from JR097 (Section 3.2) and to help quantify the effect of tides on melt rates and circulation, an effect found to be important under Ronne-Filchner Ice Shelf (Makinson and Nicholls, 1999).

As well as using novel combinations of model components, new data visualization techniques were developed for, and used in this study, highlighting some flaws in the previous output routines and leading to the identification of several bugs both in the output routines and in the model code. Major changes to the code made in the course of this work are listed in Appendix B, which also provides details of the settings used in the different model runs.

4.1 Model description

The POLAIR modeling system consists of a coupler, which calls several component sub-models in turn. These sub-models are, in the order in which they are called, atmosphere, glacier (ice shelf), ice (sea ice), land, and ocean. This nomenclature will be used in this section, so all mention of the ice model refers to the sea ice model. Each of these models is described in the following sections.

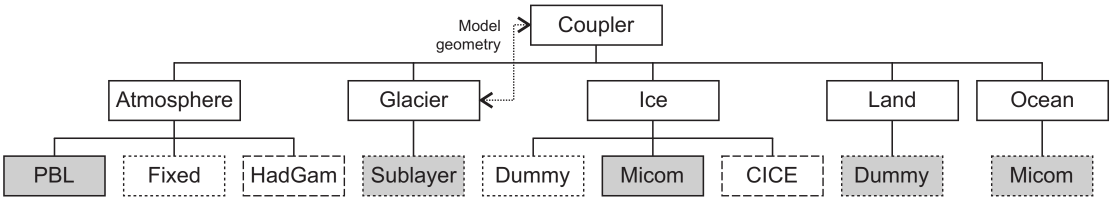

Figure 4.1: Diagram of the structure of the POLAIR modeling system (not complete). The boxes with dashed lines are not yet implemented or fully tested, those with dotted lines were used in LHS2006 and in Section 4.3.1, and the shaded boxes are the models used for the other runs in this chapter.

4.1.1 Coupler

The coupler allocates grids for the domain geometry and for all variables that are used to exchange data between sub-models. In theory, this should allow for a fairly simple replacement of model components. In addition, the coupler provides routines for data I/O, interpolation, and date calculations; however, the models must currently keep track of variable positions within files and all other data. Although the idea behind the system is that each sub-model can work on different grids, currently all sub-models use the same grid as the coupler. The glacier model is slightly more intertwined with the coupler, since it also loads the orography, a task that perhaps would be more appropriate to place within the coupler. Several choices of sub-model are available, as shown in Figure 4.1.

Currently boundary conditions are set by the coupler, and are used for all models. In past POLAIR runs, the most commonly used boundary condition was the Dirichlet (zero-value, no-slip) condition, while free-slip conditions also are available, as well as periodic conditions across the E–W or N–S boundaries; no open boundary conditions are currently implemented.

The eastern and western boundary conditions have been set to cyclic in the runs presented here, so all water or ice flowing out of the western boundary circulates back in through the east and vice versa — though it may be modified by any restoring that is set up on the boundaries. On the northern boundary free-slip conditions were used, while the southern boundary was set to no-slip. However, no ocean model points actually reach the edge of the grid.

4.1.2 Atmosphere model

The PBL (planetary boundary layer) atmosphere model, as it is configured in these model runs, merely loads surface air temperature and sea-level pressure data from files containing daily averages from the NCEP reanalysis (Kalnay *et al.*, 1996). These are used to calculate the geostrophic wind to provide surface stress forcing for other submodels. The geostrophic wind vectors are rotated 25 degrees (clockwise in the southern hemisphere) and multiplied by 0.8, to take account of drag in the boundary layer. In addition, the model calculates a radiation balance based on the local insolation, the albedo and other properties of the local ocean/sea ice/land surface. These values are then fed back into the coupler grids.

The major modification that has made to the atmosphere model code was to enable multi-year forcing. With this implementation, the model generates new forcing files with NCEP data for one year (actually from Dec. 31st of the previous year to Jan. 2nd of the following year) at the first time step following 12:00 noon on Jan. 1st of each year. This is done to be consistent with the filtering/interpolation algorithm that is applied to annually recurring daily forcing: a three-day window is applied to the data to smooth them and interpolate between the measurements. The filter weights are calculated by the coupler.

The fixed atmosphere sub-model used by LHS2006 does not provide any heat fluxes at the surface. Instead, the ocean model restores temperatures and salinities at the surface, as described below. The fixed model prescribes an easterly wind, decreasing as a cosine from a set value at the southern boundary to zero at the northern boundary. The strong wind scenario used by LHS2006 had a maximum wind speed of 15 m/s, while the weak wind scenario had a speed of 10 m/s.

There are currently plans to couple other atmosphere models into POLAIR, such as HadGam, most probably through some form of one-way coupling. However, at the time of writing, this has not yet been completed.

4.1.3 Glacier (ice shelf) model

The glacier model is a very simple thermodynamic ice shelf. It takes in the atmospheric temperature, precipitation, and sublimation rates, ocean mixed layer temperature, salinity, and friction velocity (u*), and provides basal freshwater and heat fluxes following the three-equation parameterization of Jenkins (1999). Some support for including glacier dynamics is provided for an idealized ice shelf scenario, but this is not implemented for general ice shelves.

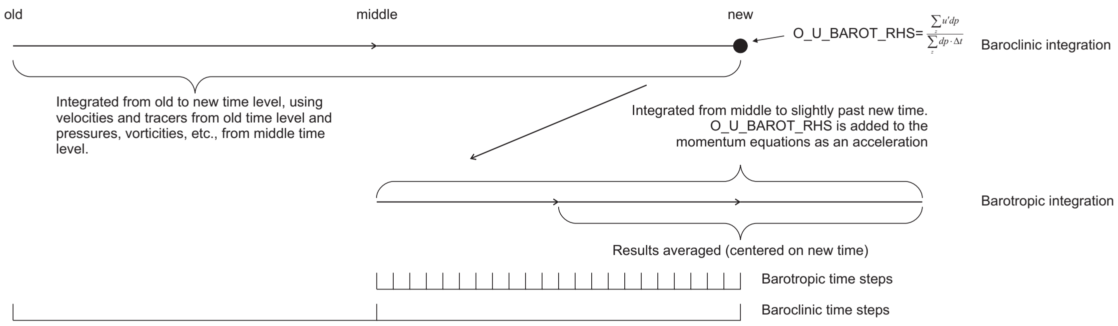

Figure 4.2: Time stepping scheme used in the MICOM implementation in POLAIR.

4.1.4 Sea ice model

The sea ice model currently implemented is a cavitating fluid model (Flato and Hibler, 1992, Holland and Jenkins, 2001). This implementation uses the same basic equations of motion as the ocean model, but using a different rheology for the ice. This means that the ice has no resistance to divergent forces, but a limited strength to resist compression.

Cyclic boundary conditions are applied such that ice advected out of the western boundary is imported from the east and vice versa. However, along the boundaries (including the cyclic boundary) the ice concentration is restored toward monthly climatological values (averages of SSM/I ice concentrations from 1987–1995 from Comiso, 1990, updated 1995). The thickness is not restored, and is allowed to develop thermodynamically throughout the domain. The model is initialized with 99% ice concentration and 1 m ice thickness throughout.

4.1.5 Ocean model

The ocean model in POLAIR is based on the Miami Isopycnic Coordinate Ocean Model (MICOM; Bleck and Smith, 1990), with subsequent modifications following Sun *et al.* (1999), Higdon (1999), and Holland (2001a), among others. The vertical coordinate is virtual potential density (i.e. compensating for the compressibility introduced by the thermobaric effect), and the equations of motion are split into baroclinic and barotropic components. The experiments described here use a coupler time step of one hour, split into six baroclinic time steps (ten minutes); each of these is split into a further 22 barotropic time steps (approximately 27.3 s). Tests performed at BAS with several domains have shown that 22 barotropic time steps per baroclinic step is the maximum at which the model consistently is stable (Paul Holland, pers. comm.).

The time stepping scheme of the model follows Higdon (1999) and is shown in Figure 4.2. First the baroclinic fields are integrated from the "old" to the "new" time using a leapfrog scheme. Then the barotropic fields are integrated from the middle time to one baroclinic time step past the new time using a forward–backward scheme; the barotropic residual from the baroclinic velocity fields is added as an acceleration to the baroclinic momentum equations. The barotropic fields, averaged over two baroclinic time steps centered on the new time, are used as the value at the new time step; this "blurring" of the barotropic fields contributes to the stability of the model. The fields are then shifted so the middle time step becomes the old, the new time step becomes the middle, etc.

One important detail when using cyclic boundary conditions is that the boundary conditions for the barotropic pressure variable need to be disabled to avoid introducing spurious pressure gradients on the boundaries. This is particularly important when tides are used, as otherwise the tides — especially the semi-diurnal components — are attenuated at the boundaries. Boundary conditions are applied to the barotropic velocities at each barotropic time step, and to the averaged pressures and velocities at the end of the barotropic solver at each baroclinic time step.

Sub-grid-scale eddies are not explicitly parameterized in the model. However, a diffusion term is applied to the layer thickness fields in the model (Holland, 2001b), and this takes the same form as the eddy parameterization from Gent and McWilliams (1990). However, Gent (2011) does note that this type of layer thickness diffusion had previously been included in isopycnic models to increase stability, also prior to its explanation as an eddy parameterization. The diffusivity applied here ($10\,\mathrm{m}^2/\mathrm{s}$ — see Table B.1) is about two orders of magnitude smaller than that used in other models (e.g., Danabasoglu and McWilliams, 1995). Thus, any reduction of the slope of isopycnals is considerably weaker than in reality.

In POLAIR, tidal forcing is implemented by restoring the surface elevation along the boundaries of the domain. The original implementation restored the elevation on the boundary toward a computed tidal elevation. However, this suppressed the background circulation, as the elevation associated with the coastal current was effectively set to zero; this was particularly noticeable when cyclic boundary conditions were used. Therefore, a modified method was developed: first the scenarios are run without tides, and without any barotropic restoring along the boundaries. At every coupler time step (one hour) the barotropic pressure two grid cells from the boundary is written to a raw binary file. The scenario is then rerun, and the file is loaded in during the run. Tides are superimposed on the surface elevations from the file and the barotropic pressure is restored toward these values, with a time constant varying linearly from 14 minutes (0.01 days) on the boundary to 1:12 hours (0.05 days) five grid cells inward. The tidal elevations are calculated at every baroclinic time step using ten constituents from the Circum-Antarctic Tidal Simulation model (CATS02.01, Padman *et al.*, 2002), with nodal corrections applied but without inferring any of the minor constituents. Model velocities in the interior of the domain have been shown to fit the values predicted by CATS very well; the restoration time constants were chosen to provide a good fit to the CATS velocities while still allowing the non-tidal circulation to develop. By superimposing the tidal elevations on the background elevations from previous runs, hopefully more of the barotropic background circulation that otherwise would be suppressed by the tidal forcing will be maintained. For testing purposes, the model was also run with this surface restoring on, but without tides.

In POLAIR, all layers exist throughout the domain, with some thickness, even if this number is very small (the mixed layer has a minimum thickness of 10 m). The original behavior of MICOM was to copy the temperature of the layer above into thin layers, and then calculate the salinity as a function of the temperature and the layer's target density. However, in POLAIR this was modified so that the layers took on both the temperature and salinity of the layer above, effectively lowering the density of the layer; this was apparently done because the original MICOM algorithm caused spurious salinities to appear in the model. In a domain like Fimbul Ice Shelf, where layers disappear and reappear seasonally and on shorter timescales, this approach had a particularly pronounced effect, and led to a considerable drift in the layer densities, to the point that inversions were quite commonly seen (Paul Holland, pers. comm., 2007). One side effect of this method was that the water seen inside the ice shelf cavity was cooled, since the water masses whose properties were being copied downward were all near the freezing point. The fix to this problem was not to transfer the water mass properties downward: very thin layers therefore end up with the properties of the water that is advected into the cells — and as long as no diapycnal mixing is implemented they will not influence the properties of surrounding layers. One consequence is that the water masses in the cavity are considerably warmer than before. Surprisingly, this has not had a major impact on the basal melt rates. Because the densities now remain closer to their target values, spurious pressure gradients have been reduced, and the kinetic energy in the ocean model now comes much closer to reaching a steady state, whereas before it continued to increase linearly; therefore, this change appears to be extremely important. In other model domains these problems were not as serious, probably because layers did not disappear and reappear as frequently, since less variable forcing was applied.

There are still some problems with the model code that have not been addressed in the runs discussed in this thesis. One bug that was identified and fixed involved the advection terms in the momentum equation; near boundaries the transport could effectively be halved because of a mistake in the calculation. In addition, Paul Holland recently implemented an updated version of the advection scheme, following the same methodology as HYCOM. However, since these changes it has not been possible to get the model to complete a run without crashing 17–18 years into the integration. Another issue that remains in the code is the implementation of Higdon's (1999) modifications to the calculation of the Montgomery potential. The implementation of these changes was never completed, so some parts of the calculation still use the original Bleck formulation. However, to complete this, and to perform adequate testing of the code is beyond the scope of this thesis.

4.1.6 Domain/bathymetry

In order to use E–W cyclic boundary conditions, a modified bathymetry dataset had to be generated. The name of the new orography in the model is FIMBUL_CYCLIC.

The basis for the new bathymetry was Bedmap (Lythe and Vaughan, 2001), with Nøst's (2004) bathymetry substituted in the region where he had made measurements. The Antarctic Digital Database (ADD; SCAR 2000) was used to generate a mask of the grounded areas of the ice shelf. Two grid cells north of the ice front, GEBCO bathymetry (IOC *et al.*, 2003) was then substituted. All ice shelf areas apart from the main ice shelf cavity were then masked out; this was done to reduce the effect of spurious melt rates beneath the smaller ice shelves close to the boundaries. Toward the eastern and western boundaries, the bathymetry was shifted south- and northward, respectively, to make the coastlines line up. All areas deeper than 2500 m were set to 2500 m depth, and small, isolated shallower areas near the boundaries were removed so the eastern and western boundaries had similar profiles. The reason for limiting the depth was to keep the barotropic time steps reasonably long.

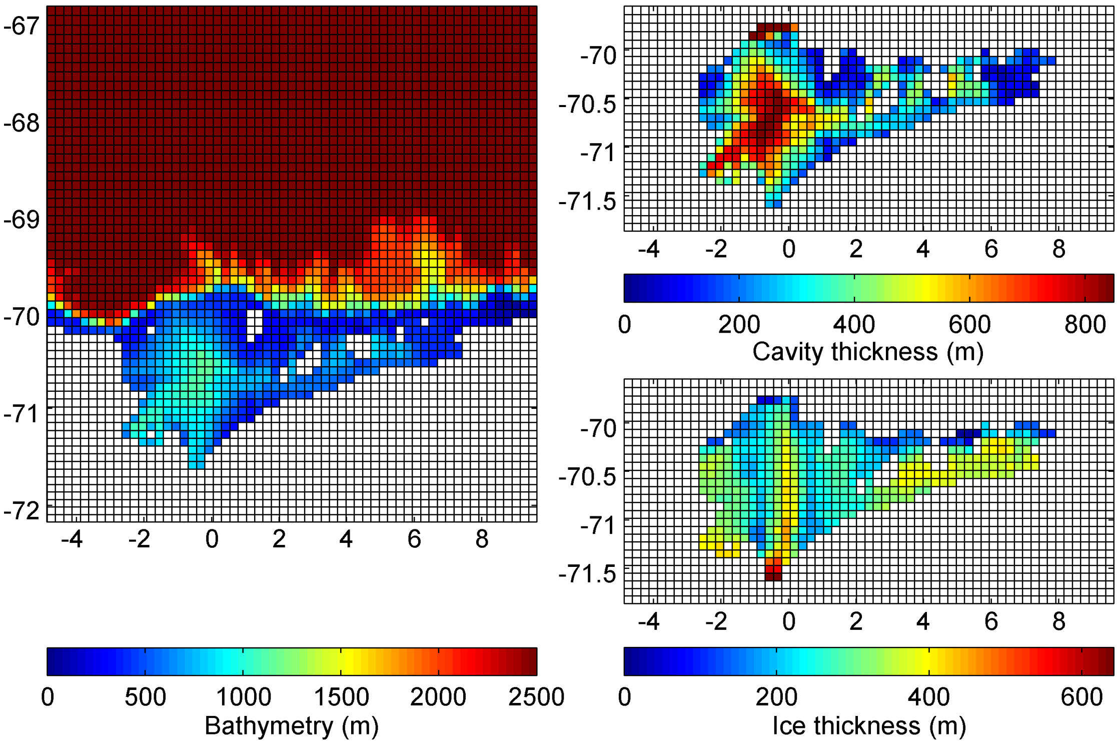

Figure 4.3: Map of the bathymetry used in the POLAIR model. This figures shows the bathymetry, cavity (water column) thickness, and ice thickness.

The resolution of the model is 0.25° longitude, with the latitudes chosen so grid cells are square. The domain is from 4° 45′ W to 9° 45′ E, 72° S to 67° S, with 61 × 62 grid cells. This means that the size of the grid cells varies from 8.6 to 10.9 km. There are either 16 or 6 vertical coordinates (see Section 4.1.8).

The resulting bathymetry, shown in Figure 4.3, is slightly idealized: all ice shelf cavities apart from the main one have been filled in. However, conditions along the boundaries are improved, since we can now use east/west cyclic boundary conditions, removing the solid walls that previously were present. Nonetheless, it is still possible to retain restoring along the eastern/western boundaries. Note that all maps in this chapter are plotted using an equirectangular projection, with the standard parallel at the center of the modeling domain (69° 30′ S).

4.1.7 Forcing

The main forcing for the model comes from the atmosphere; in addition, the ocean is restored in various ways.

The atmospheric forcing used in LHS2006 consisted of imposing a fixed easterly wind varying as a cosine from the southern to the northern boundary of the domain.

No radiation was used, and instead temperatures were restored to the local freezing point, and salinities were restored to a predetermined value: some runs used a constant salinity, while some had a seasonally varying value. No sea ice model was used, as prescribing a seasonally varying salinity is meant to parameterize the annual cycle of sea ice freezing and melting.

For the new runs, temperature and sea-level pressure forcing from the NCEP reanalysis (Kalnay *et al.*, 1996) have been used. Geostrophic winds are calculated from pressure fields, and assuming a slight rotation of the wind because of the planetary boundary layer, this causes a wind stress on the ice or ocean. Since surface air temperatures also are imposed, a sea ice model needs to be included, as the surface water otherwise would be supercooled, causing unrealistic convection. The sea ice concentration is restored toward climatological monthly values along the boundaries, while the thickness is allowed to develop thermodynamically. The time scales used for this restoration vary linearly from 5 days to 1 day over five grid cells from the boundaries.

Along the boundaries the ocean temperatures and salinities were initially restored to the AWI Hydrographic Atlas of the Southern Ocean (Olbers *et al.*, 1992). However, since this only has a resolution of one degree latitude/longitude (equivalent to 111 km/38 km) and most of the variability in this region is across the shelf break, this does not resolve the slope front adequately. Therefore a new "pseudo-climatology" was generated for the domain, based on the source data from the AWI atlas, other Norwegian and German cruises in the area, and JR097. First all the data were loaded, and the points with depths that clearly were inconsistent with their location were removed (e.g., deep stations located on the shelf). Then the profiles were sorted by bottom depth, and median temperature and salinity profiles were generated for each standard depth in the AWI atlas. Outliers were then removed and interpolated values substituted. Finally these standard profiles were used as a lookup table by depth to fill in the model domain with a resolution of 0.5 degrees longitude (equivalent to approximately 19 km). The areas beneath the ice shelves were filled with a separate profile based on the CTD data from Autosub.

Although this climatology is not necessarily representative of year-round conditions in the area, it does provide reasonable boundary conditions, with a clear slope front, as well as WDW off the shelf. Although the E–W boundary conditions are cyclic, it was decided to restore the ocean and ice conditions along these "boundaries", to avoid the model drifting away from realistic values. This is done on time scales decreasing linearly toward the boundary from 30 to 10 days. Note that this is a long time constant, so the restoring is fairly weak.

4.1.8 Distribution of water masses across layers

The choice of vertical coordinates is an important decision in an isopycnic model, and deserves some justification. Three different sets of vertical coordinates were used: the ones used by LHS2006, a modified distribution, and a simplified set of only six layers. A complete list of the model runs, and which coordinate systems were used, is given in Appendix B, Table B.4.

The three sets of model layer densities are plotted in Figure 4.4. It is clear that the LHS2006 coordinates have very high resolution in the lower layers (WDW and WSDW), and lower resolution in the ISW and MWDW range. The new coordinates have attempted to rectify this by slightly reducing the number of dense layers and increasing the resolution in the intermediate layers; it is the runs with these coordinates that are primarily used in this thesis. As a test, some runs were done using six layers: one layer for WSDW, one for WDW, one in the cooler range of MWDW/the denser range of ISW, and two layers for lighter surface water. In this context, WDW layers are defined as layers 9–16 in LHS2006 coordinates, layers 12–16 in the new coordinates, and layers 5–6 in the 6-layer coordinates. This definition includes the layers that contain WSDW, although these do not extend into the ice shelf cavity.

The distribution of these layers on a section along 1° W in January and July 1989 is shown in Figure 4.5, with the upper boundary of the WDW layers plotted with a dashed line. After 19 years, the model has reached a fairly representative state. In the summer plots (left column), the mixed layer is relatively thin, and there are a wide range of non-WDW layers in the cavity. Outside the cavity, the lighter layers are more pronounced in the coastal current, while denser layers are present further from the coast. In winter, the mixed layer is thicker both inside and outside the cavity. The slope front appears steeper, and the mixed layer is particularly thick at the ice front. Outside the cavity, the intermediate layers are very thin, with the mixed layer in direct contact with WDW layers.

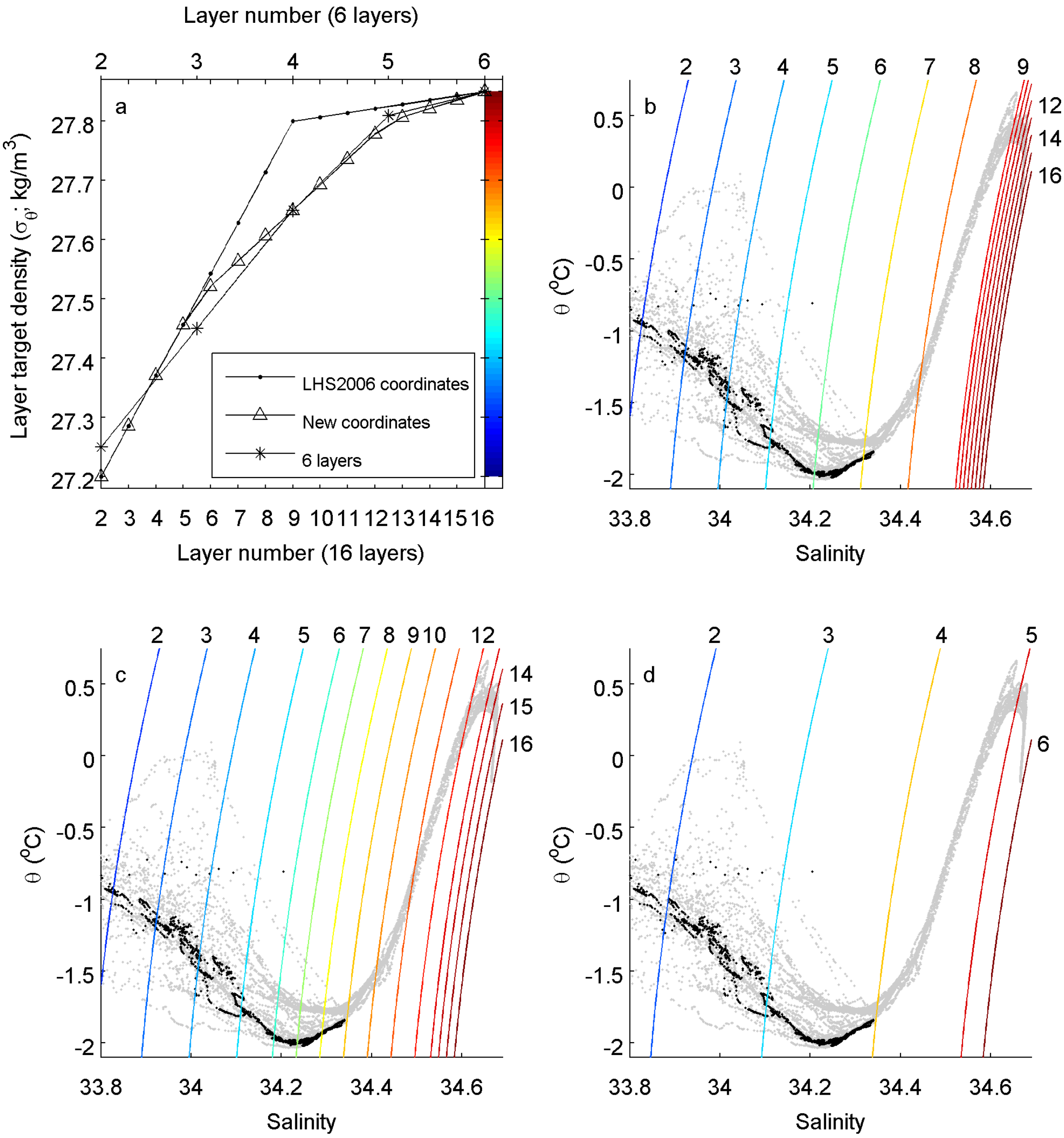

Figure 4.4: Vertical (density) coordinates used in model runs. Layer 1 is the mixed layer, with varying density. The color scale used in panel (a) is used to show the density of the isopycnals in panels (b–d), as well as in Figure 4.5. Panels (b–d) show the distribution of model layer densities in θ/S space; (b) shows the LHS2006 coordinates, (c) the new coordinates, and (d) the six-layer coordinates. In the background are θ/S data from JR097 in gray, and Autosub CTD data in black.

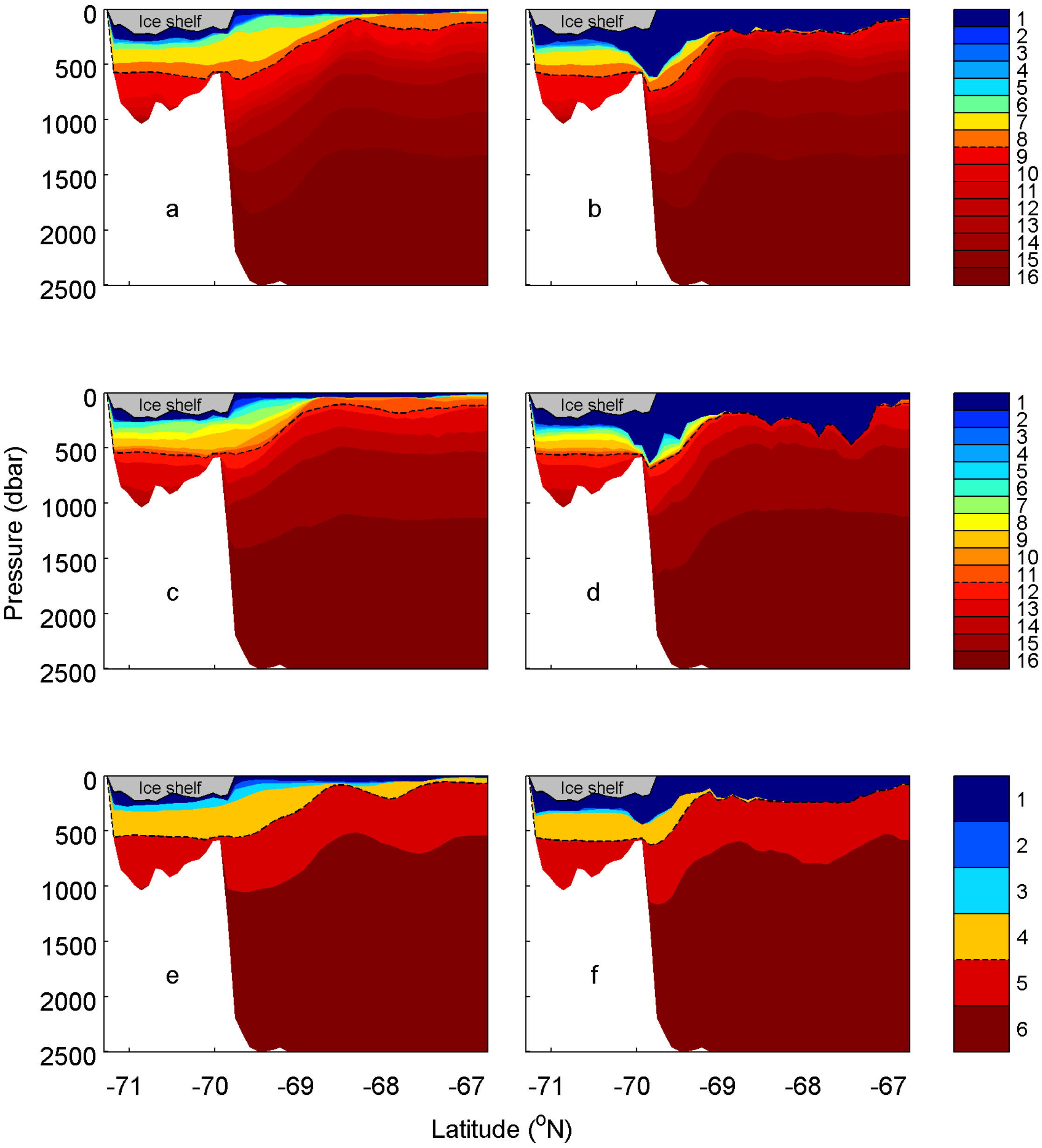

Figure 4.5: Distribution of layers on a N/S section at 1° W, without tides. The left column (a, c, e) are averages over Jan. 1989; the right column (b, d, f) are from July 1989. The first row (a, b) uses the LHS2006 coordinates, the second (c, d) uses the new coordinates, and the third (e, f) has six layers. The dashed lines indicate the top boundary of the WDW layers (as defined in Section 4.1.8). The coloring of the layers uses the same density-based color scale as in Figure 4.4.

4.2 Model runs

Two overall sets of forcing were used for the model results shown in this chapter. The first uses the same forcing scheme as LHS2006, where surface winds are prescribed, and sea surface salinities are restored either to a constant or sinusoidally varying value. The second uses NCEP atmospheric forcing, with a sea ice model enabled.

All of the runs described here were spun up for ten years (1970–1979); in the NCEP runs the forcing for 1980 was repeated ten times during this period. The runs using LHS2006 forcing were then run for an additional two years, while the NCEP runs were run for 25 years (1980–2004). All of the runs were performed both with and without tides enabled.

The details of all the model runs (combinations of forcing, tides, and isopycnic coordinates) are given in Table B.4 in Appendix B.

4.3 Modeling results

4.3.1 LHS2006 forcing

To evaluate the runs from LHS2006, the newest version of the model code (with modified bathymetry and boundary conditions) was initially run with the same forcing: fixed atmospheric forcing, and surface temperature/salinity restoring. As in LHS2006 two wind speeds were used along the northern boundary: 15 m/s and 10 m/s (referred to as ‘strong’ and ‘weak’ winds), and both constant and sinusoidally varying target sea surface salinities were used (‘constant’ and ‘varying’ SSS). The surface temperature was restored toward the *in situ* freezing point. All four possible combinations of these choices were run for twelve years, with and without tidal forcing enabled; the first ten years were considered to be the spin-up, with the last two years used for the subsequent analysis.

The fraction of WDW (as defined in Section 4.1.8) under the ice shelf is shown in Figure 4.6. The case with strong wind and constant SSS forcing effectively keeps WDW out of the ice shelf cavity; after 12 years there is no appreciable increase in this water under the ice shelf, and some of the WDW included in the number comes from underneath the ice tongue, where we would expect to find WDW. With varying SSS we get a slight, near-linear increase in WDW under the ice shelf, but still at a very slow rate. The inflow occurs in October, with a slight outflow in September. The runs

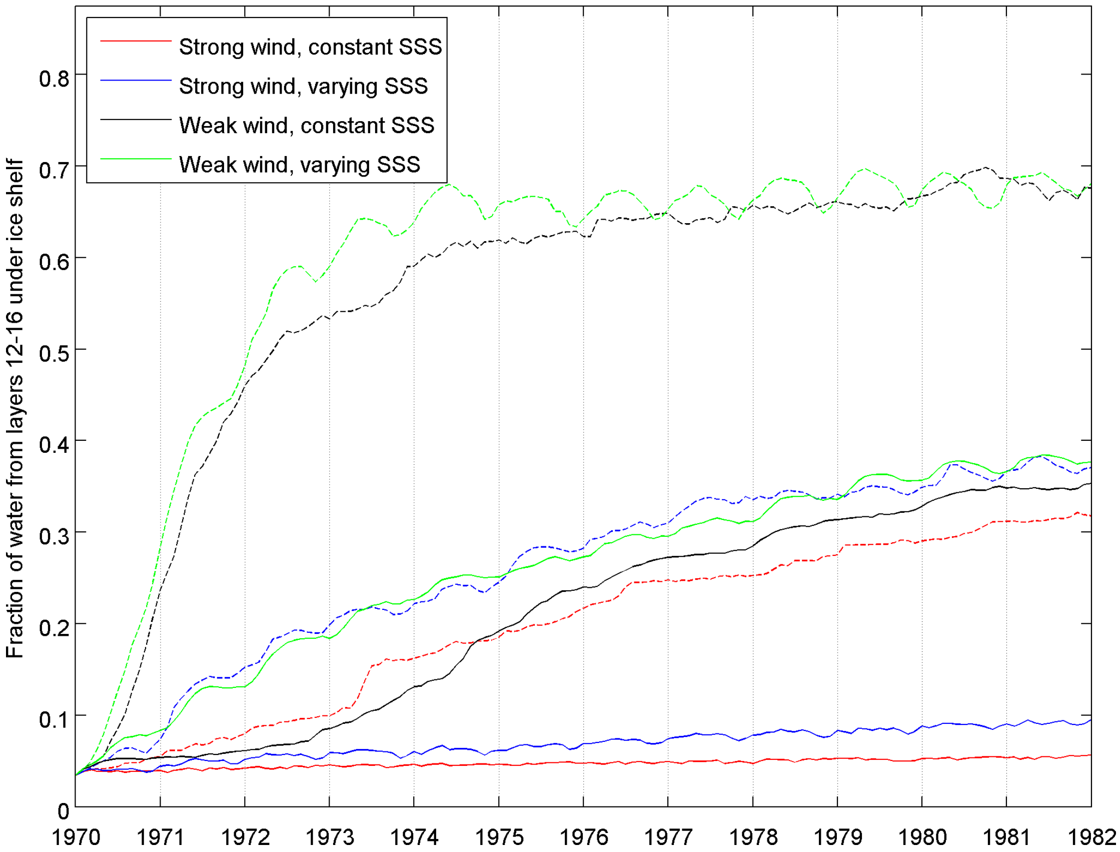

Figure 4.6: Fraction of WDW under ice shelf, with LHS2006 forcing. Dashed lines indicate runs with tides.

with weak wind let considerably more WDW into the cavity; the run with constant SSS appears to reach a near steady state after eleven years. The run with weak wind and varying SSS has an inflow occurring over several months during the summer; it still appears to be increasing after twelve years. In the runs with tides enabled, the increase in WDW beneath the ice shelf is most pronounced in the first two years, while the model is spinning up. The runs with weak winds are close to a steady state after four years, with a very high level of WDW in the cavity.

The basal melt rates from these experiments, as well as for NCEP forcing and LHS2006 and test runs with AWI atlas climatology are shown in Table 4.1, as well as in Figure 4.11. All of the runs appear to reach a steady state; the runs with variable salinity restoring show a clear annual cycle, with the highest melt rates in late winter or early spring. Tides clearly cause higher melt rates beneath the ice shelf, probably because of increased mixing.

To estimate the effect of the choice of climatology on the boundaries, the model was run with LHS2006 forcing using the AWI atlas on the boundary. The result is

Table 4.1: Average basal melt rates (cm/year) for various runs, following 10 years of spin-up (i.e. 2 years for fixed atmosphere runs, 35 years for NCEP runs). The final line of the table is one of the model runs from Smedsrud *et al.* (2006).

	Fimbul climatology			AWI atlas	
	Tides off	on		Tides off	on
Strong wind, constant SSS	17.8	54.6		24.3	89.8
Strong wind, varying SSS	29.5	62.1		35.8	98.0
Weak wind, constant SSS	16.2	94.3		27.0	122.5
Weak wind, varying SSS	22.1	86.8		47.1	151.6
LHS2006 coordinates, NCEP	53.4	88.2	63.5[a]	-	-
New coordinates, NCEP	55.5	88.3		-	-
LHS2006 (strong wind, constant SSS)	-	-		193	-

---

[a] Elevation restoring on, tides off

a consistent increase in the melt rates; the overall average increase is 57%. I believe most of this increase is because the slope front is not resolved adequately, allowing WDW to reach the ice shelf cavity.

4.3.2 NCEP forcing

In an attempt to replicate the complex annual cycle more accurately and introduce interannual variability to the model, it was run with varying wind and temperature forcing, and with the sea ice model enabled. The first step in evaluating these results is to compare it with the previous forcing.

4.3.2.1 Comparison of NCEP and LHS2006 forcing

One question that must be answered before comparing the results of LHS2006 with this study is how the LHS2006 forcing compares with the more complex NCEP forcing and sea ice model. This especially applies to the runs with varying SSS forcing, as they attempt to reproduce the annual cycle of sea ice freezing and melting. The annual cycle of SSS at a point in the open ocean is shown in Figure 4.7. The prescribed target SSS has its minimum in March and maximum in September. This is approximately two months later than occurs in the runs with NCEP forcing. As a consequence, the annual cycle of the model lags behind by approximately two months; this is also visible when comparing Figure 4.13 and Figure 4.6: the main inflow to the cavity occurs around December with NCEP forcing, and in late summer with weak wind and varying SSS. The prescribed annual cycle in SSS is slightly smaller in amplitude

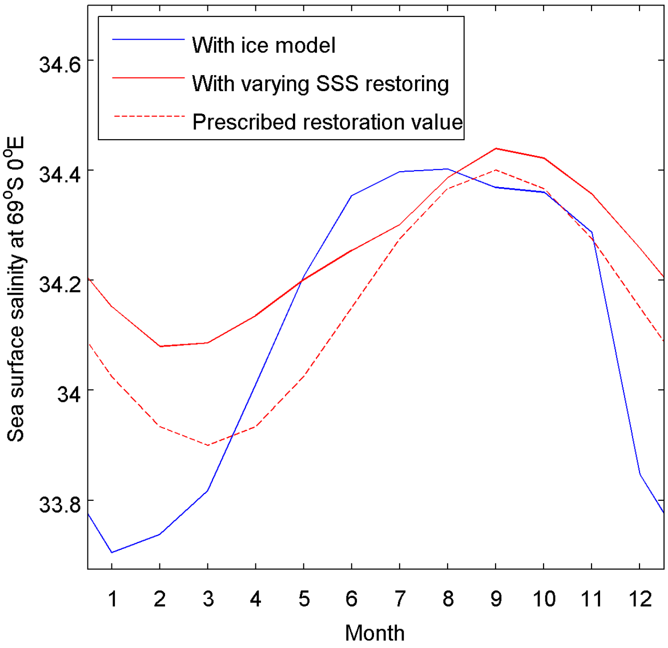

Figure 4.7: Annual cycle of sea surface salinity at 69° S 0° E with NCEP (sea ice model; blue) and LHS2006 (SSS restoring; red) forcing. The values used to restore the SSS are also shown (red dashed line).

than in the run using NCEP forcing, with the resulting model SSS cycle showing even less variability.

4.3.2.2 Annual cycle

The annual cycle of SSS in the runs with NCEP forcing and sea ice are largely determined by the annual pattern of winds and temperatures from the NCEP reanalysis and the radiation balance calculated by the atmosphere model. In addition, climatological sea ice concentrations are used to force the sea ice model along the boundaries. Each of these mechanisms has some uncertainties and limitations, discussed below.

The NCEP reanalysis has a resolution of 2.5 degrees of latitude and longitude. This is clearly not fine enough to resolve small-scale features like katabatic winds on glaciers on the Antarctic Peninsula. For that purpose, a finer model would need to be used, as was done, for example, by Skogseth *et al.* (2007) for model runs of Storfjorden, Svalbard. However, while Storfjorden is surrounded by steep topography and multiple small outlet glaciers, the topography over Fimbul Ice Shelf is relatively flat.

Neethling (1970) lists the frequency of wind directions observed at the original SANAE I station (near the coast) from 1963–1966, and found that more than 60% of observations are from between ENE and SE, with the mode being directly from the east. So while the NCEP model may not resolve some of the local wind circulation on the ice shelf itself, it should do a reasonable job on the ocean in the vicinity of the ice front and further offshore.

The NCEP temperatures, however, are more suspect. They are known to be too low in much of the Antarctic region during winter (Large and Yeager, 2004). This is explained by the fact that the NCEP model does not allow partial sea ice concentrations: the sea ice is either present (10/10 cover) or absent; this means that around the coast, the atmosphere is not warmed by the heat flux through leads in the sea ice. Large and Yeager (2004) suggest a correction by imposing a minimum temperature as a function of latitude and day of year. The resulting zonal average difference during the winter is around 4–8 °C at about 70° S. As we have not performed any corrections, we may have an excess of around 500–750 freezing degree days each winter, with most of these occurring toward late winter. We would expect this to lead to a later sea ice melt than observed, and a larger cycle in sea surface salinity than in reality.

Unfortunately we do not have any winter salinity observations from the mixed layer to compare with the model output. However, monthly climatological sea ice concentrations from Schweitzer (1995), which are derived from the same dataset as the model forcing, have been compared with the sea ice concentration cycle from the model. Since the climatology uses data from 1978–1991, ice concentrations from 1980–1989 (the first 10-year run following spin-up) have been used for the comparison. Compared with the subsequent 15 years, model ice concentrations from these years are slightly lower in April and May, but around 4% higher from August to November.

The sea ice concentrations from the model and climatology are shown in Figure 4.8. The model has a larger range of winter concentrations than the climatology, as would be expected. However, on average the model has lower ice concentrations during the winter, and slightly higher ice concentrations during the summer. Both the domain average ice concentrations and the averages along 0.3° W are plotted; while the domain average values appear to be well correlated to the climatology, the annual cycle at 0.3° W slightly lags the average model values and the climatology. This could indicate that the forcing from the boundary is taking some time to propagate into the middle of the domain. It should be noted that the climatology uses a mask that includes Trolltunga, so ice concentrations close to the ice front are omitted.

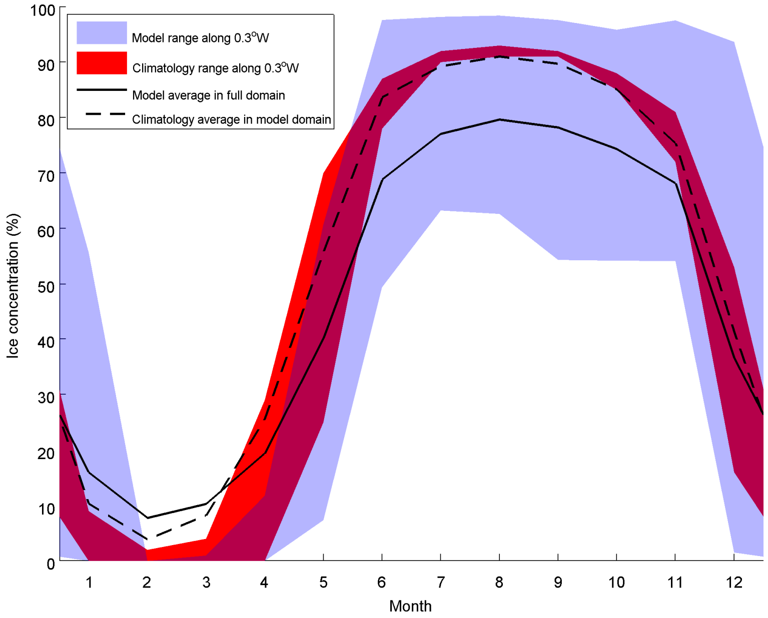

Figure 4.8: Monthly ice concentrations from the model and climatology (Schweitzer, 1995).

The annual patterns of inflow and outflow through the sills in runs with and without tides are shown in Figure 4.9; the letters in Figure 4.9d will be used to refer to the different sills here. The most persistent pattern observed here is that there is net inflow through the main sill, A, in summer (December–March), and net outflow in autumn (April–June). Sills C and E, east of the ice tongue, both show weak outflows in January–March, and inflows for the rest of the year. This could be significant, as sill C could be deep enough to potentially lead into the main cavity. Sill D shows a fairly persistent outflow for most of the year, with a weak inflow in November–December. In the tidal runs, the inflow from sills C and E is considerably stronger from May to November.

Figure 4.10 shows the mean monthly circulation, with and without tides enabled. The December–February circulation patterns qualitatively look very similar between the runs with and without tides; the cyclonic circulation beneath the main part of the ice shelf appears to be strongest in December. The circulation gradually weakens, reaching a minimum in April. The inflow from sill E in the tidal runs is clearly visible from May to November, with some additional inflow from sill C, and a bit of recirculating outflow through sill D. Where the resulting inflow reaches the main cavity, it appears to disrupt, or at least weaken, the outflow through sill B.

Looking at Figure 4.9c, which shows the volume fluxes in layers 12–16 only, with densities corresponding to WDW, the annual cycle looks somewhat different. Here the

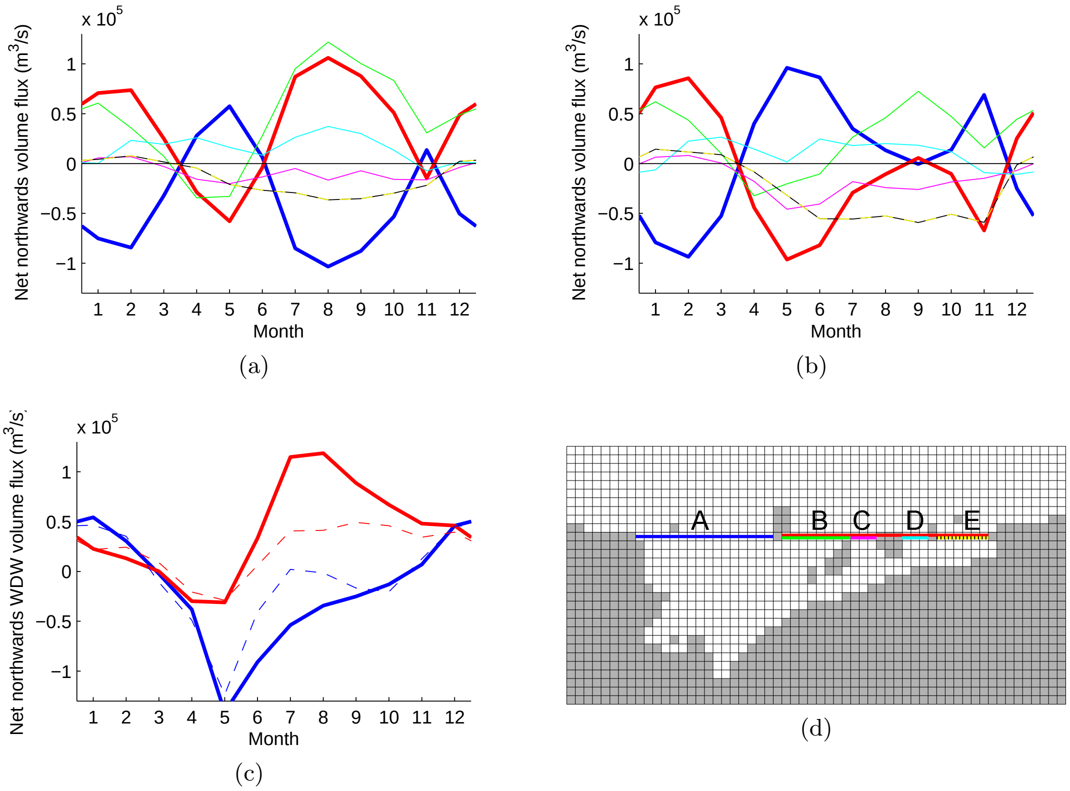

(a)

(b)

(c)

(d)

Figure 4.9: Net volume fluxes across 70° S; (a) without tides, (b) with tides. (c) Net fluxes in layers 12–16 (WDW) without tides (solid lines) and with tides (dashed lines). The map in part (d) shows the color scheme used for the lines in parts (a), (b), and (c).

inflow through sill A is strongest in May, decreasing through winter, becoming a slight outflow in November through February. The eastern sills (B–E) have a strong outflow in July–August, with net inflow only in April and May. These cycles are roughly the same in the runs with and without tides, though the tidal runs have weaker outflow through the eastern sills.

The annual cycle in melt rates for the NCEP runs is plotted in Figure 4.11 (a)–(b), with and without tides. During the summer, high melt rates are found near the ice front, as warm surface water contacts the base of the ice shelf. These propagate inward toward the grounding line, where the maximum melt occurs during the winter, except near the grounding line where Jutulstraumen flows into the ice shelf. In all of the runs some areas of freezing are seen around Trollkjelen. Interestingly, the runs with tides appear to have stronger areas of freezing, including more freezing around Jutulgryta. The runs with NCEP forcing have the strongest melt signal near the ice front; this is probably because these runs do not have surface temperature restoring, which could cause anomalously low temperatures in the LHS2006 runs. Apart from

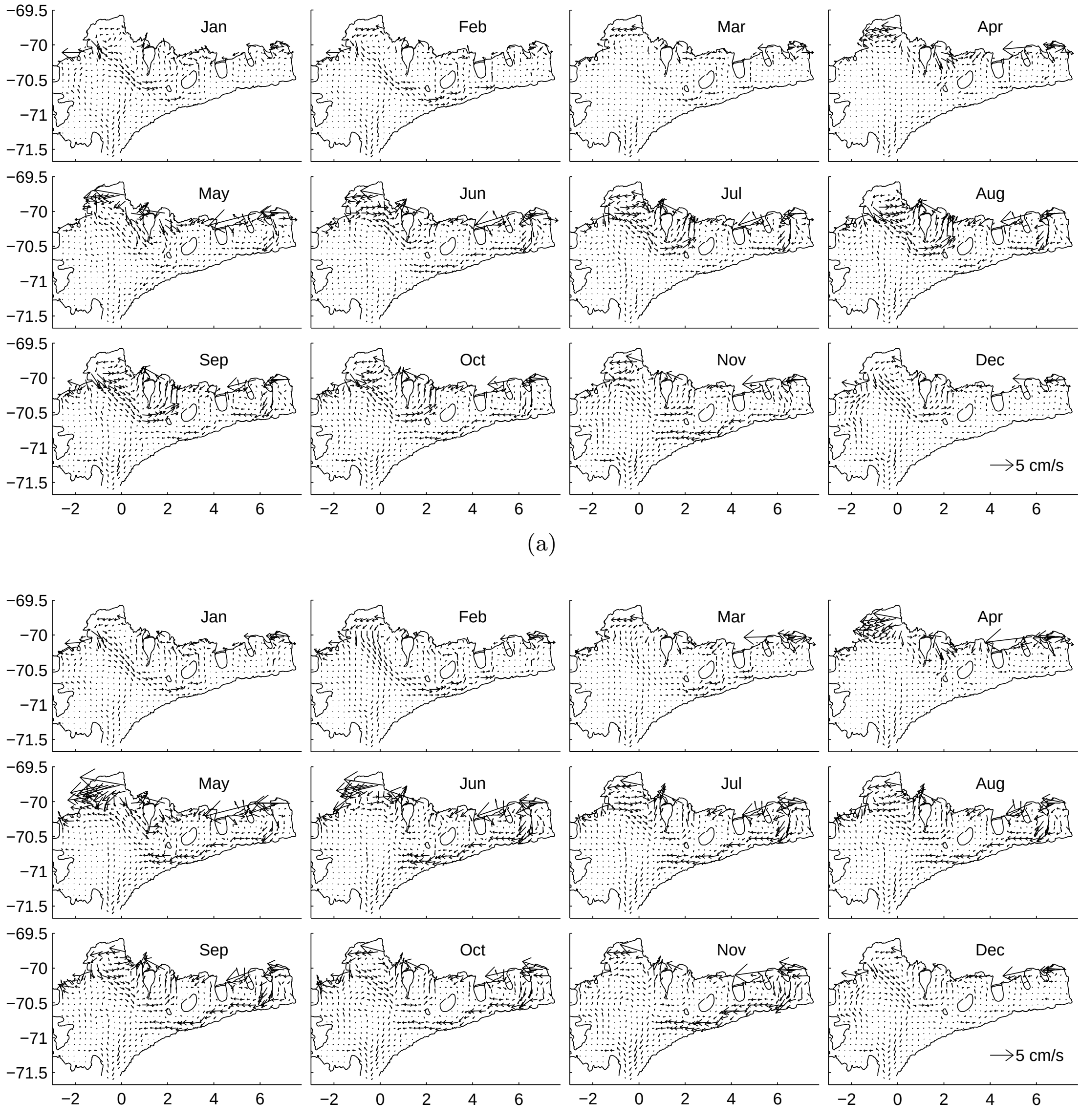

(a)

(b)

Figure 4.10: Average monthly currents from POLAIR; (a) without tides, (b) with tides.

the area near to the ice front, the pattern of melting propagating southward from the ice tongue appears to be similar between the ‘strong wind, varying SSS’ run in panels (c)–(d) and the NCEP runs in panels (a)–(b). The same pattern can be seen in the ‘weak wind, varying SSS’ run without tides in panel (e), though the melt rates are considerably lower, while the pattern of melting is quite different in the run with tides (in panel (f)), which displays higher melt rates along the main keel of the ice shelf emanating from Jutulstraumen. This pattern can also seen in the runs with constant SSS and weak winds in panel (j), as well as in the original ‘strong wind, constant SSS’ run from LHS2006, plotted in panel (k).

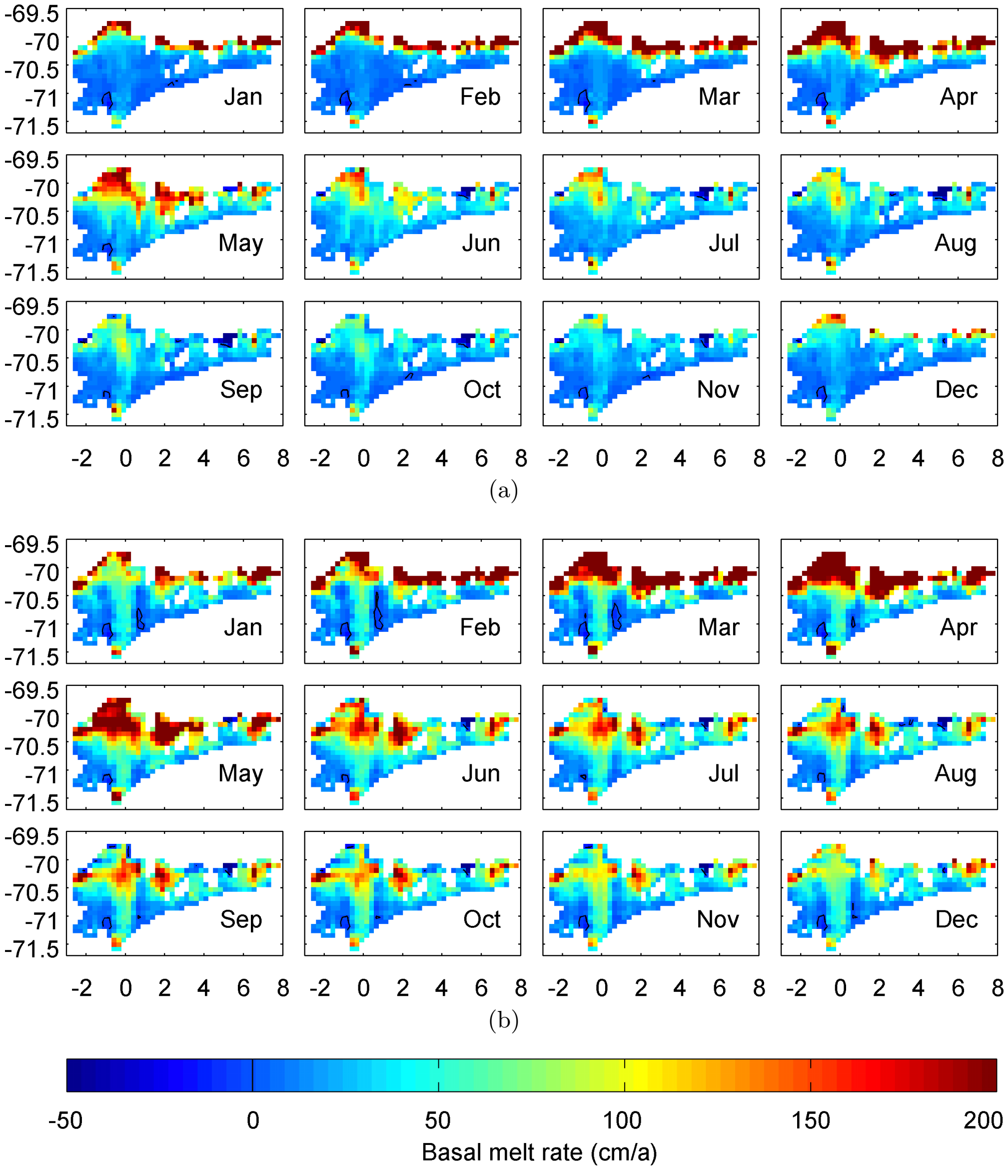

(a)

(b)

Figure 4.11: Modeled melt rates from runs with NCEP forcing, averaged from 1990–2004. (a) without tides, (b) with tides. Areas of freezing are demarcated with a solid line.

Mixed layer salinities also follow an annual cycle: during the summer sea ice melt causes the mixed layer to freshen and thin, while brine rejection during the winter causes it to deepen and get more saline. This signal is visible at the ice front and propagates southward, where it reaches its minimum around June halfway toward the grounding line, and has a minimum in August–September at the grounding line; this occurs both with and without tides present. As the signal propagates southward, it is attenuated; the amplitude of the annual salinity variation at the grounding line is around 0.15; in the open ocean it is around 0.7 (see Figure 4.7).

The propagation of the month of the minimum mixed layer salinity is shown in

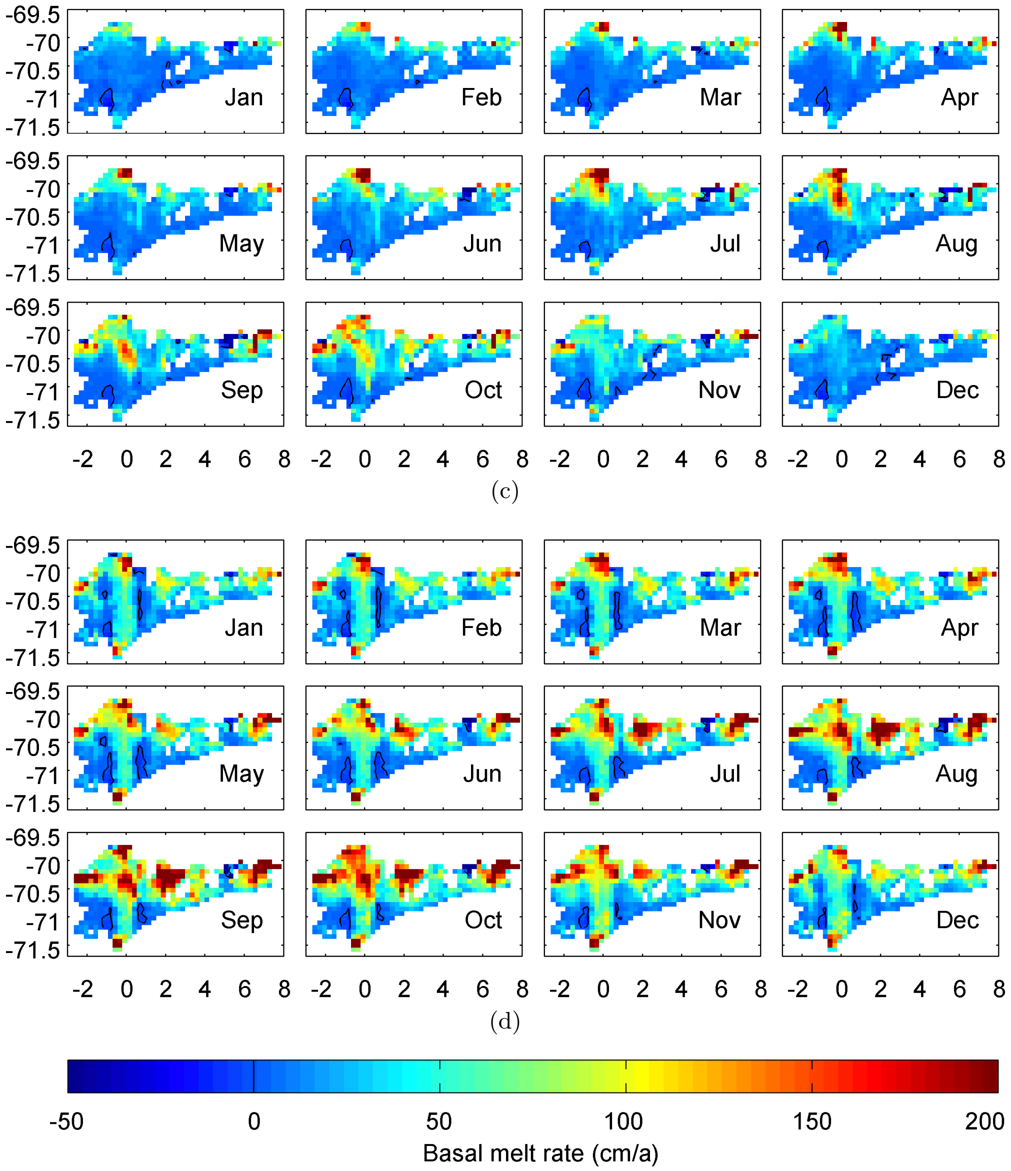

(c)

(d)

Figure 4.11: (continued) Modeled melt rates from runs with LHS2006 forcing, using strong winds and varying SSS. (c) without tides, (d) with tides. Areas of freezing are demarcated with a solid line.

Figure 4.12. A lag of two months appears to be introduced at the ice front itself; the lag seems particularly pronounced at the western part of the ice shelf cavity. The propagation of the signal is slightly faster when tides are switched on, but follows a similar pattern. It is likely that this signal is advected around the ice shelf cavity, rather than caused by local melting.

In terms of the energy budgets, all of the runs show the same seasonal pattern, with most kinetic energy in late autumn and early winter, and least energy in the summer, when the water column is most strongly stratified, making energy transmission from the surface downward more difficult. In addition, the strongest winds are

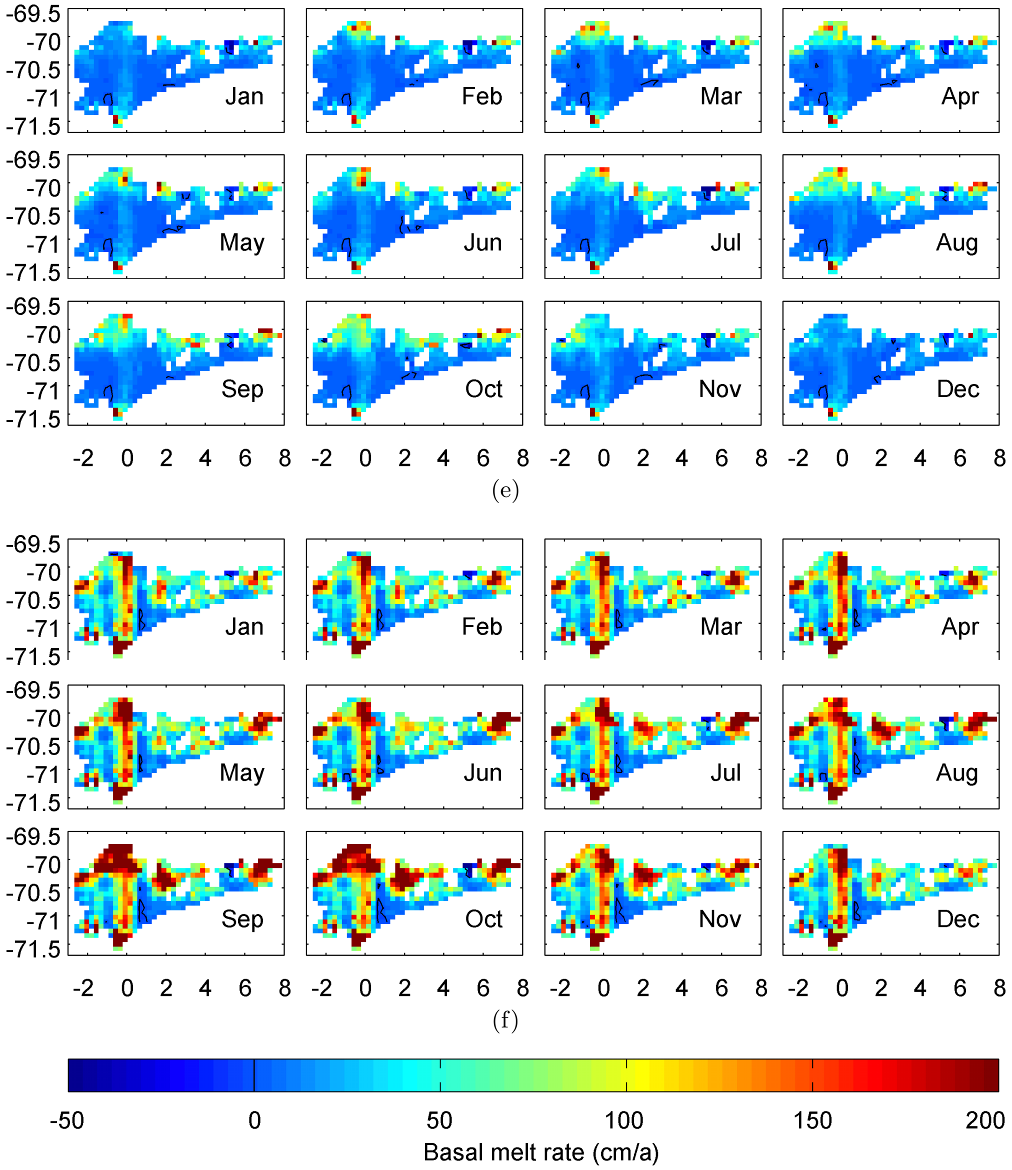

Figure 4.11: (continued) Modeled melt rates from runs with LHS2006 forcing, using weak winds and varying SSS. (e) without tides, (f) with tides. Areas of freezing are demarcated with a solid line.

found during the winter; however, increased sea ice cover will also reduce the transfer of momentum from the atmosphere to the ocean surface (E. Fahrbach, pers. comm., 2011).

4.3.2.3 Interannual variability

In addition to the annual cycle, the model also shows interannual variability, caused by changes in the wind and temperature forcing. One of the reasons for doing the modeling work was to use model results to interpret variations in data from Fimbul Ice Shelf, and to "fill the gaps" between measurements. This is, however, considerably

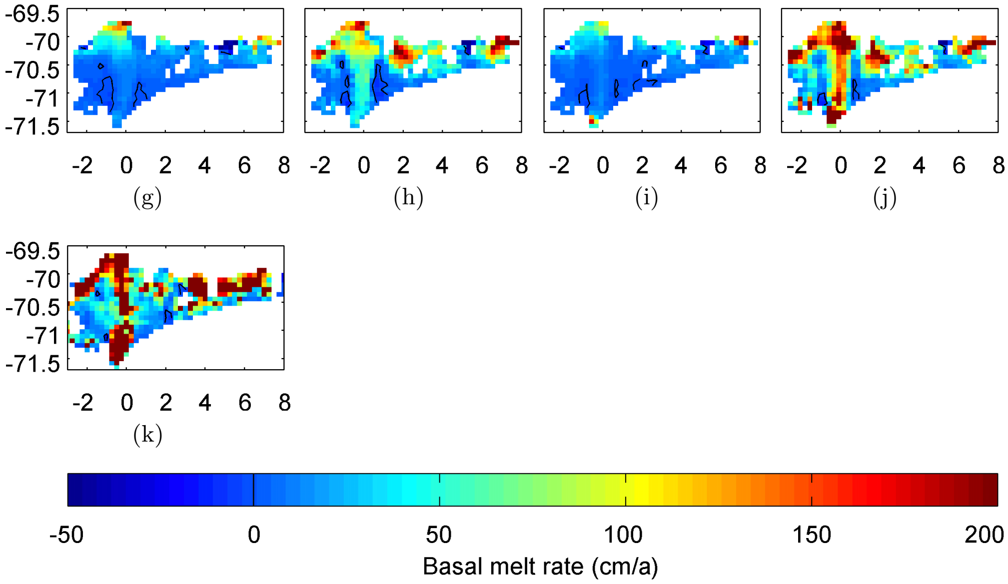

Figure 4.11: (continued) Modeled melt rates from runs with LHS2006 forcing, using constant SSS. (g) strong winds and no tides, (h) strong winds with tides, (i) weak winds and no tides, (j) weak winds with tides, and (k) strong winds and no tides, results from the model runs of LHS2006. Areas of freezing are demarcated with a solid line.

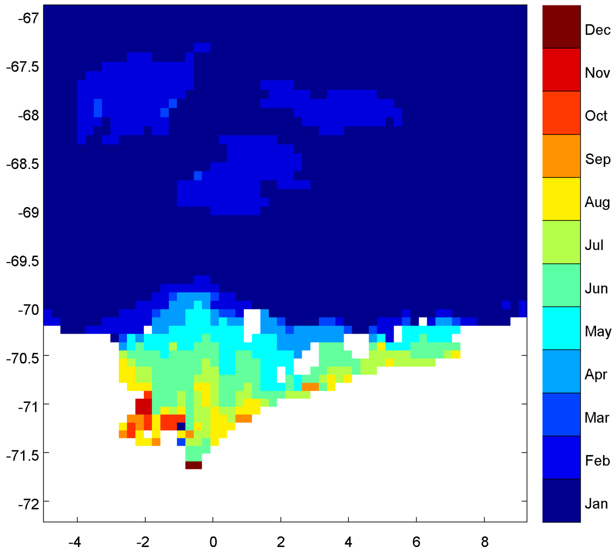

Figure 4.12: Month of minimum average mixed layer salinity, without tides enabled.

more difficult than originally envisioned, because of the complexity of the model and the whole system around Fimbul Ice Shelf. Nevertheless, some interesting patterns have emerged.

There does not appear to be any obvious correlation between the wind forcing and either the inflow of warm water beneath the ice shelf or basal melt rates. From Figure 4.13 we can see that the amount of WDW under the ice shelf does vary annually as well as on decadal time scales. After spin-up (1970–1980), the WDW levels under the ice shelf decrease, until they begin to rise again in 1998, leveling out again around 2003–2004. While there does not appear to be any year-to-year correlation between wind strengths and WDW levels, there does appear to be a longer-term correlation: the zonal winds did strengthen on average through the early 1990s, weakening in 1997, when the WDW levels started to increase again. So it is possible that a much slower adjustment to the long-term wind averages does take place. However, this would be with a lag of more than a year. This is discussed further in Section 4.4.2.1.

Comparing Figure 4.6, which shows the WDW fraction beneath the ice shelf for the LHS2006 runs, with Figure 4.13, which shows a similar plot for NCEP forcing, the LHS2006 runs with weak wind forcing and no tides end up at more or less the same levels as the runs with NCEP forcing. The scenarios with strong wind let less WDW in, but the run with strong winds and tides enabled is also similar to the NCEP runs. Enabling tides seems to have a much greater effect on the LHS2006 runs than on the runs using the more variable NCEP forcing. Having a steady, strong wind over the shelf is, of course, not realistic, so it is likely that the overall effect of the varying wind forcing is closer to that of having a constant, but slightly weaker, wind.

Finding any correlation between melt rates and atmospheric patterns has been unsuccessful. There are clearly some years where melt rates are particularly low (e.g., 1982 or 2003), but no anomalies in atmospheric patterns that could explain them satisfactorily have been found.

4.3.3 Fluxes across 70° S and WDW fraction under ice

Fluxes across 70° S have been investigated in various model runs, to see how sensitive the inflow and outflow through the cavity is to changes in the forcing, choice of vertical coordinates, and whether or not tides are switched on. The section along 70° S is

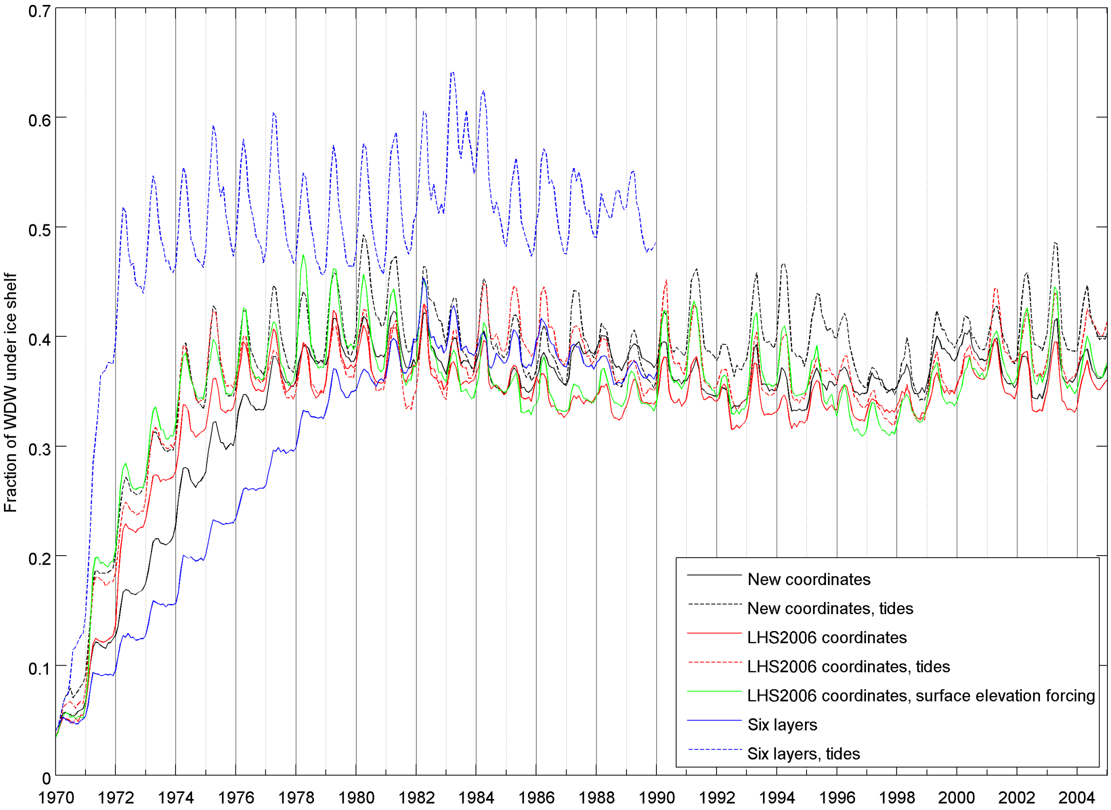

Figure 4.13: Fractions of WDW (as defined in Section 4.1.8) in the ice shelf cavity with different vertical coordinates and surface elevation forcing.

very useful since it captures the fluxes across the eastern and main sills, and west of the ice tongue it also intersects the coastal current.

The two sets of runs with 16 layers display very similar patterns. As would be expected, currents visible in certain water masses in the LHS2006 coordinate runs are visible in the layers with corresponding densities in the new coordinate runs (not shown; some vertically integrated fluxes are shown in Figure 4.9). So it appears that the choice of coordinates does not seem to be that important to the overall patterns of inflow; the new runs merely have higher resolution at intermediate densities, and less resolution in the densest range. The fraction of WDW under the ice shelf is plotted in Figure 4.13. Here we can see that although the spin-up/response time of the model does seem to depend slightly on the choice of coordinates, the end result is remarkably similar for the three different vertical coordinates, except for the six-layer run with tides enabled.

The runs with six layers show considerably reduced circulation within the ice shelf cavity, perhaps because the layers in which exchange between the cavity and the open ocean take place are not adequately resolved. Also, the slope front is weakened considerably when tides are switched on, letting much more warm water enter the cavity. Most likely this is caused by a lack of resolution.

4.3.4 Sensitivity to tides

After spin-up, the fluxes into the ice shelf cavity seem largely unaffected by the presence of tides, unlike the LHS2006 runs, where tides make a large difference. To remind the reader, tides were implemented by restoring the boundary elevations to values from the non-tidal run, with tides superimposed; in addition, a run was performed with this restoration, but without tides for comparison. The coastal current is strengthened considerably both in the runs with tides switched on and in the runs with surface restoring but without tides. Since the coastal current accounts for a large part of the kinetic energy in the model, these two scenarios have a total kinetic energy approximately 2 PJ higher than the runs without elevation restoring; the scenario with tides has around 0.2–0.3 PJ more energy than the non-tidal one. Melt rates are strongly affected by tides, increasing by around 60%; this is discussed further below.

The runs with only six layers are strongly affected by tides: when tides are switched on, the slope front is weakened considerably, and warm water quickly enters the cavity, reaching a much higher level than in any of the other runs (dashed blue line, Figure 4.13). In the scenario with tides, WDW occupies around half of the cavity within two years, and it appears to be close to a steady state after three. In contrast, the runs without tides appear to level off only after 12 years, and the fraction of WDW in the cavity is around 0.35.

The barotropic transport (vertically integrated velocity) within the cavity, with and without tides, is shown in Figure 4.14. Again, we see that the overall circulation is very similar between the runs with LHS2006 coordinates and those with the new coordinates. However, the flow between the main sill and the main cavity is reduced in the scenarios with six layers. The main circulation within the cavity is cyclonic, with an outflow east of the teardrop-shaped ice rise in the runs without tides. When tides are switched on, inflow from the eastern sills is strengthened, and a larger part of the outflow occurs west of the ice rise.

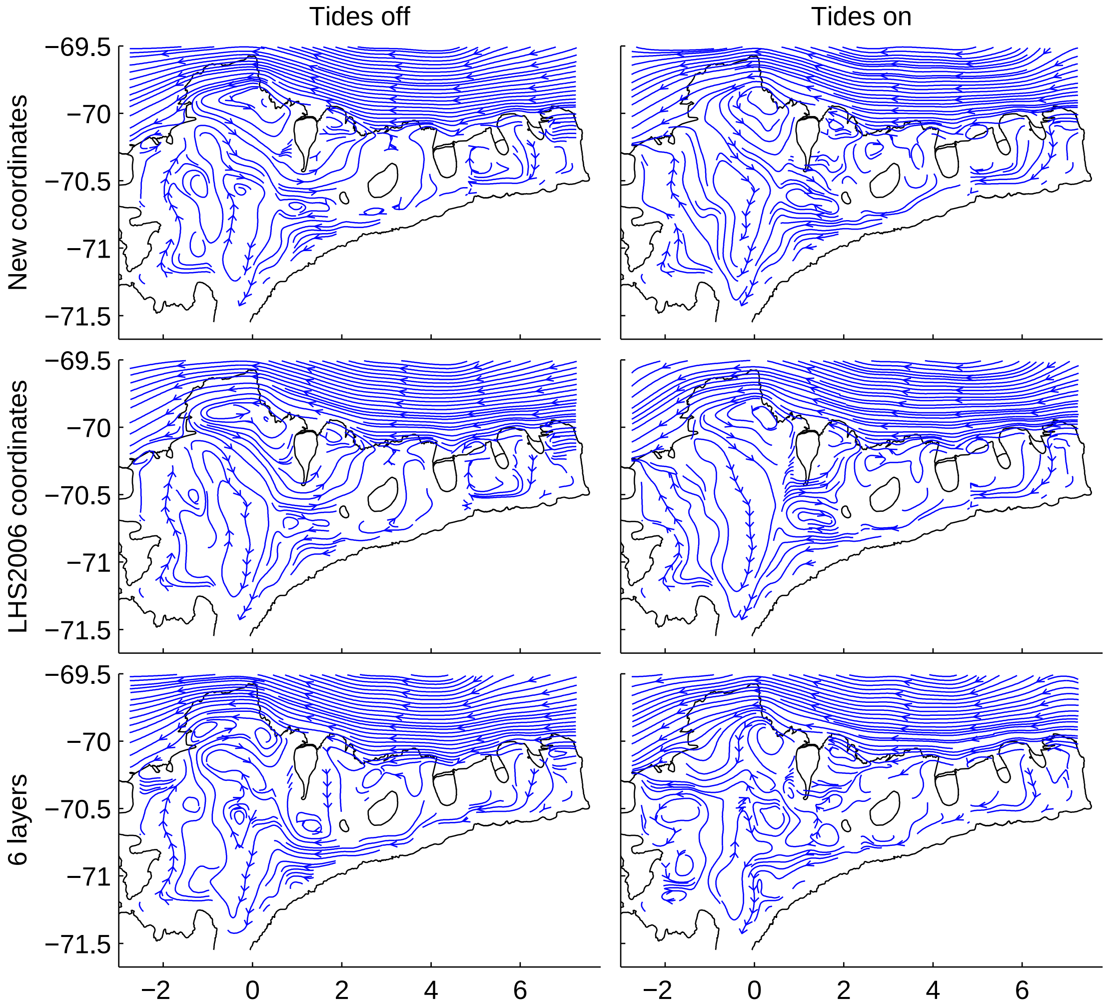

Figure 4.14: Vertically integrated circulation beneath the ice shelf, averaged over the ten years following spin-up.

4.4 Modeling discussion

4.4.1 What influences the melt rate?

One of the key questions that remains to be answered about ice shelves is what determines the melt rate. Clearly it is not enough to determine the amount of available heat entering the ice shelf cavity; for example, at Pine Island Glacier the amount of available heat far exceeds the amount that actually melts the base of the ice shelf (Holland, talk at Royal Society, 17 Oct. 2005). In the course of this modeling study a bug was found, whereby the temperature of the water in the lower layers within the cavity was strongly reduced (see Section 4.1.5); when this was fixed, the effect on the melt rate was negligible — probably because the lower layers do not directly contact the base of the ice shelf, and the model has no diapycnal mixing between isopycnic layers. While some diapycnal mixing does take place in reality, observations indicate that it is much smaller than isopycnal mixing in this region (Leach *et al.*, 2011), and it is unlikely to significantly affect the overall results in this domain.

While the strong inflow of WDW through the main sill in May–June, shown in Figure 4.9c, probably is related to the strong outflow through the eastern sills in July–August, it is difficult to connect this inflow pattern to the corresponding annual cycle in melt rates in Figure 4.11 (a)–(b). Again, this is probably because of a lack of coupling between the deeper WDW layers and the mixed layer, except through direct entrainment/detrainment, which is unlikely to happen beneath the ice shelf, except very close to the grounding line (see Figure 4.5).

Since the model runs described in this thesis, several more have been performed, though they did not run stably. However, over the time when they did run, melt rates appear to be even lower than those shown here. The changes mainly concern the implementation of the advection scheme.

On small scales, the melt process is fairly well understood. Holland and Jenkins (1999) have described the interaction between a melting ice shelf and the boundary layer below. However, some discussion of how water reaches the base of the ice shelf in the model, and how realistic this treatment is, is needed here.

The only layer that is in direct contact with the base of the ice shelf is the mixed layer. When freezing occurs, the mixed layer will entrain water, decreasing its buoyancy; in contrast, when melting occurs, as is the case under most of Fimbul Ice Shelf, denser water is detrained to lower levels, and the mixed layer thins. If we assume that the mixed layer is the coldest layer, being in contact with the ice shelf, any cycle of entrainment and detrainment would lead to an overall warming of the mixed layer — and this would transport heat instantaneously from the base of the mixed layer to the top. In the case of tides, a twice daily cycle of melting and freezing could heat the mixed layer quite effectively. At some points near the ice rises and the grounding line fairly persistent entrainment can be found. At these points, where melting is occurring, entrainment takes place to keep the mixed layer above its minimum thickness of 10 m when advection otherwise would thin it beyond this point. So these points effectively ventilate the mixed layer drawing water up from the deep; this is also what is presumed to occur at the grounding line in reality (see, e.g., Robin, 1979). This also occurs along the keel of Jutulstraumen during late summer in the model.

The mixed layer entrainment cycles in the open ocean and beneath the ice shelf are almost exactly 180° out of phase: the highest rates of entrainment outside the ice shelf are found in May, with a minimum in November, while under the ice shelf the maximum occurs in December and the minimum in April. Outside the ice shelf, rates are highly variable, with changes of several hundred meters occurring in a day in the coastal current. While rapid entrainment certainly can occur because of the addition of TKE from winter storms, the speed of detrainment seems to be very high — perhaps unrealistically so. There is a net positive available TKE in the open ocean, stemming from wind mixing, and net negative available TKE under the ice shelf, because of melting.

When detrainment occurs beneath the ice shelf, the mixed layer is split into a lower part, which is added to an isopycnic layer, and an upper part, which is re-entrained into the mixed layer. This split is described in more detail by Holland and Jenkins (2001); however, the model does not follow this algorithm exactly as described in their paper. In their nomenclature, the mixed layer is split into a “Gaspar layer”, with a thickness and properties determined by the buoyancy forcing from above conserving TKE, and a “fossil layer” making up the rest of the prior thickness of the mixed layer. Then the fossil layer is split such that the lower part has the same density as the layer into which the detrainment occurs, while the upper part is added to the new mixed layer. The total heat and salt in the lower and upper fossil layers are conserved in this split. Beneath the ice shelves the fossil layer split does not occur orthogonal to isopycnals: it is forced to follow the slope of the line connecting the fossil and Gaspar layer properties. This means that the split could end up warming the layer into which water is detrained — and would cool the mixed layer, since heat has to be conserved. This process could lead to decreased melt rates. While this has not been observed directly in the model, some tests run by Keith Makinson on the FRIS domain have shown warming of up to 0.2 °C in lower layers, accompanied by supercooling of up to 0.1 °C in the mixed layer; this occurred around the ice front (Keith Makinson, pers. comm., 2007–2008). While this is an extreme example, it clearly shows that the parameterization used in the model may need more scrutiny. Although it is useful to compare relative melt rates from the model, the absolute melt rates, both in this study and in LHS2006, may be suspect, mostly because of the uncertainties in the mixed layer model.

4.4.2 Level of “warm” water in cavity vs. reality

Clearly the model hydrography differs markedly from actual conditions beneath the ice shelf; the warmest water observed beneath the ice shelf was $-1.75\,^{\circ}\mathrm{C}$ (at Jutulgryta, 371 m depth; see Figure 2.3b). However, the model lets “unmodified” WDW with temperatures above $0.5\,^{\circ}\mathrm{C}$ enter the cavity. While this is not realistic, one characteristic feature of the Autosub dataset is evident in the model. The warmest water was observed in the deepest part of Autosub’s track, and the AUV crossed the surface freezing point almost exactly at the maximum depth of the main sill, around 570 m. This corresponds very well to the model levels shown in Figure 4.5.

4.4.2.1 Response of the model to changes in wind forcing

To investigate the response of the model to changes in wind forcing, the model was run with LHS2006 forcing, alternating the wind forcing between weak and strong every three years, using both constant and varying SSS restoration, and with tides off. The resulting level of WDW beneath the ice shelf is shown in Figure 4.15. During the initial ten years of spin-up, the varying SSS scenario clearly brings more WDW beneath the ice shelf. However, once a fairly steady state is achieved (after approximately 30 years) the difference between the two scenarios narrows considerably in the periods of strong wind. While changes to the fraction of WDW under the ice shelf appear to begin almost instantaneously after the wind forcing changes, the model does not achieve equilibrium in the subsequent three years.

Even though the imposed forcing clearly is exaggerated — the wind does not suddenly go from a very strong state to a weaker state — it does show that adjustments to more subtle variations in wind patterns may take longer to manifest themselves in the depths of the ice shelf cavity. Referring back to Figure 4.13, the fast response and large initial falls in WDW fractions could imply that the annual cycle probably can be largely attributed to changes in wind between summer and winter, with sharp falls in the WDW level occurring in autumn. This effect is probably much larger than that of the buoyancy forcing imposed by the annual salinity cycle, although this clearly also does play a role.

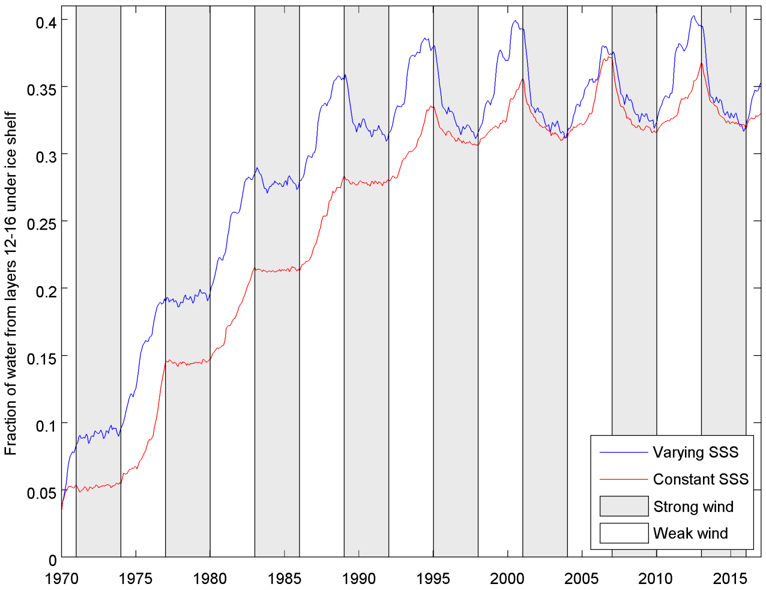

Figure 4.15: Response of model to variations in wind forcing. The shaded areas show when strong wind was applied, the white areas have weak wind forcing.

4.4.3 Outflow pathways of ISW

According to Holland and Feltham (2006), ice shelf water flows will stay in near-geostrophic balance, except when they are constrained by topography. The obvious topographic features at the base of the ice shelf that could affect the outflow of ISW are the keel of ice emanating from Jutulstraumen and the rifts that are formed near the ice shelf front.

Seen "upside-down" the case of flow of meltwater along a keel of ice is similar to the flow of dense water along a submarine ridge. This scenario was described by Darelius and Wåhlin (2007), who applied it to the case of the ISW plume flowing down the continental slope at Filchner Sill. If we assume that the "height" of our keel is 150 m, its width is 25 km, our ice shelf slope is approximately 1.25×10^{-3}, and the reduced gravity of our ISW is 3.6×10^{-4} $\mathrm{m\,s^{-2}}$, we find that γ (the ratio of the flow across the keel to the Ekman drainage along it) is 330. For a cosine-shaped ridge, this would give a maximum theoretical transport capacity along the keel of 224 $\mathrm{m^3\,s^{-1}}$, which we can consider to be negligible. This agrees with the model results, which do not show any overall tendency for meltwater to flow along the keel. It is therefore more likely that the outflow of meltwater follows the overall circulation within the cavity, rather than forming a plume "leaning" on the under-ice topography.

Similar calculations could be done for the rifts near the ice shelf front. However, the slope of the ice shelf and of the fast ice within the rifts is very small, and the lengths are short compared with the size of the ice shelf, so the model proposed by Wåhlin (2004) for dense water flow in a corrugation is probably not applicable, as the flow would be highly ageostrophic. However, apart from this consideration, it seems likely that the effect of steering through rifts also is negligible. Since rifts take up a small fraction of the surface area of Fimbul Ice Shelf, the freezing that takes place there (Khazendar and Jenkins, 2003) probably does not play a major role in the mass balance of the ice shelf.

4.4.4 Is Fimbul Ice Shelf melting?

Past modeling studies have indicated extremely large melt rates beneath Fimbul Ice Shelf. As the modeling results in Chapter 4 indicate that melt rates are lower than these previous estimates, we must look to glaciological studies to evaluate these numbers. While direct studies of the mass balance of Fimbul Ice Shelf have not been done, there are studies on nearby ice shelves, which may have similar properties. Horwath *et al.* (2006) investigated Nivlisen, slightly east of Fimbul Ice Shelf, using SAR, GPS and other in-situ measurements. Their conclusion is that the average basal melt rate over a large part of Nivlisen is 654 ± 170 $\mathrm{kg\,m^{-2}\,a^{-1}}$; this assumes that the ice shelf is in steady-state (i.e. its thickness is not changing).

Similar studies have not been performed for Fimbul Ice Shelf. However, we do have some information about the local conditions. Jutulstraumen transports 13.4 ± 1 $\mathrm{km^3\,a^{-1}}$ of ice into Fimbul Ice Shelf (Rignot and Thomas, 2002). One estimate of the basal melt rate near the grounding line, where Jutulstraumen flows into Fimbul Ice Shelf, is 4 ± 3 $\mathrm{m\,a^{-1}}$ (Rignot and Jacobs, 2002); however, this value may have significant uncertainties because of the way in which it has been calculated (P. R. Holland, pers. comm., 2008) — and it is only for the area directly north of the grounding line, where melting would be at its highest.

Measurements of precipitation on Fimbul Ice Shelf itself range from 244–451 $\mathrm{kg\,m^{-2}\,a^{-1}}$, with an average of 317 $\mathrm{kg\,m^{-2}\,a^{-1}}$ (Rotschky *et al.*, 2007). This is comparable to Horwath *et al.*'s (2006) value of 300 ± 100 $\mathrm{kg\,m^{-2}\,a^{-1}}$ for the accumulation zone of Nivlisen. Melvold *et al.* (1998) performed a study of accumulation rates on Jutulstraumen, and found large variations in precipitation rates within very small areas, caused by local variations in topography and surface slope; this implies that measurements based solely on in-situ observations may have very large uncertainties; the

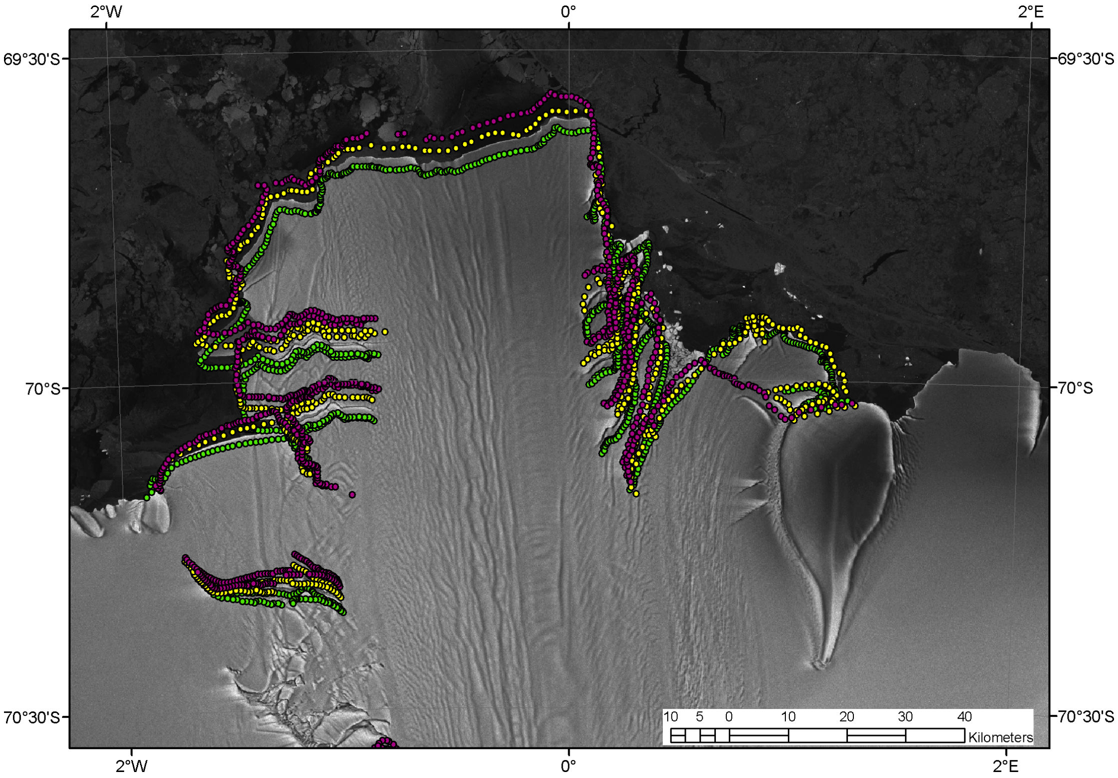

Figure 4.16: Position of the ice front at various years. Green points are from 1997, yellow from 2003, and magenta from 2006. The background image is from Radarsat (MAMM), in 2000. Some of the ice front positions were digitized by Angelika Humbert; the satellite data were provided by the Alaska Satellite Facility, UAF, and processed by Andrew Fleming, at BAS.

values also vary with elevation and distance toward the coast, so measurements from Jutulstraumen cannot be used on the ice shelf. But even if we knew the inflow from glaciers, and basal melt rate, and the surface accumulation, we still do not know the rate of iceberg calving, in order to estimate the mass balance.

There are no direct measurements of the iceberg calving rate from Fimbul Ice Shelf; however, some idea of the mass balance at the front can be obtained from looking at satellite images of the ice shelf. Figure 4.16 shows a Radarsat image of the ice shelf from 2000, with ice front positions from 1997, 2003, and 2006 superimposed. The ice front is moving around 0.67 $\mathrm{km\,a^{-1}}$ at the fastest point, reducing to 0 at the ice rises to the east and the west; it is very clear that there is significant shear across the rift around $70^\circ\,15'\,\mathrm{S}\ 1^\circ\,30'\,\mathrm{W}$; the western edge appears almost stationary, while the eastern edge has moved significantly over the nine years shown. If we assume, rather simplistically, that the velocity increases linearly from the ice rises to the center of the ice shelf and then decreases linearly toward the ice rises on the other side, and that the width of the section between the ice rises is 100 km, this gives an area change of

33.5 $\mathrm{km}^2\,\mathrm{a}^{-1}$; if we assume that the ice thickness is around 225 m near the ice front (consistent with the data from Nøst, 2004), this would correspond to a volume increase of 7.54 $\mathrm{km}^3\,\mathrm{a}^{-1}$. To put this into a budget for the central section of Fimbul Ice Shelf (in $\mathrm{km}^3\,\mathrm{a}^{-1}$ ice equivalent):

$$\begin{array}{ccccccc} 13.4 & + & \begin{array}{c}\dfrac{317\ \mathrm{kg\,a^{-1}\,m^{-2}}/900\ \mathrm{kg\,m^{-3}}\ /}{1000\ \mathrm{m\,km^{-1}} \times 17500\ \mathrm{km^{2}}} \\ = 6.2\end{array} & - & ? & = & 7.5 \\ \text{Jutulstraumen} & + & \text{Precipitation} & - & \text{Basal melting} & = & \text{Volume increase at front} \end{array}$$

This would indicate that the basal melting in this simplified balance is approximately 12.1 $\mathrm{km}^3\,\mathrm{a}^{-1}$ melt, equivalent to 69 $\mathrm{cm\,a}^{-1}$ ice equivalent, or roughly 620 $\mathrm{kg\,a}^{-1}\,\mathrm{m}^{-2}$.

4.4.4.1 LHS2006 runs

Comparing the melt rates from Table 4.1 to Figure 8 of LHS2006, we see that the values from this study are smaller by a factor of 10–15. It appears that this is partly because of the changes in the domain: the smaller ice shelves near the eastern and western boundaries were subject to very large melt rates in the LHS2006 model runs, and this severely skewed their overall average melt rate. Clearly the change from AWI atlas forcing has also made a difference, resulting in an average reduction in melt rates of around 36% in this study.

The conclusion therefore is that the choice of boundary forcing in LHS2006 contributed significantly to the overestimate of melt rates, although the choice of closed boundary conditions probably was more important.

4.4.4.2 NCEP forcing runs

The melt rates for the runs with variable forcing, with tides enabled, are around 88 cm/year. This is comparable both with the estimated steady-state melt rate derived above, and with the 1 m/year calculated from a salinity budget by Nøst *et al.* (2011). It also agrees well with the modeled melt rates from Humbert (2010) for much of the ice shelf. The error limits in all of these sources are sufficiently large that we cannot conclude within any certainty whether the mass balance of the ice shelf is slightly negative or positive, but it appears to be roughly in balance.

4.5 Modeling conclusions

The model runs shown here indicate large seasonal variability in the sub-ice shelf circulation. While this has not been directly observed beneath the ice shelf, it does qualitatively agree with many of the results in Chapter 3. Seasonally varying inflows to the ice shelf cavity could help explain the differences between the CTD profiles in Jutulgryta in 1990 and 1991 (Figure 2.2b), and also help explain the apparently varying sources of the water observed by Autosub beneath the ice shelf (Figure 3.6).

In the Autosub dataset, all the water above the lowest sill depth was at or below the surface freezing point, while the lower water was warmer. In the model runs, roughly the same is true, although the water below sill depth is significantly warmer than observed in reality. However, since there is no diapycnal diffusion in the model, the water masses below should not be able to affect the properties of the water masses above, except if they are entrained into the mixed layer. However, this only occurs during freezing, a process that only takes place in very limited areas of Fimbul Ice Shelf. This limitation on vertical heat fluxes within the ocean model can also explain why our melt rates are lower than the estimates from Humbert (2010) in the areas of the ice shelf nearer the grounding line, while our melt rates near the ice front (where the surface water masses can lose heat to the ice shelf) are higher. However, the overall melt rates appear to be closer to reality and to Humbert's (2010) results than previous efforts.

The reduction in melt rates can be attributed to several changes made, both to the boundary conditions (the choice of cyclic boundary conditions and the use of more realistic, higher-resolution, climatology) and to the code itself.

Unfortunately the resolution of this model (8.6–10.9 km) is too coarse to resolve eddies. This does mean that we cannot reproduce the fine-scale patterns of MWDW inflow directly caused by eddies and described by Nøst *et al.* (2011). The weak layer thickness diffusion used here is probably inadequate to recreate the effect of baroclinic instability near the slope front. Instead, it is possible that the relaxation of water mass properties near the boundary could be helping to stabilize the slope front in this case.

Chapter 5

Conclusions

The data from Jutulgryta (Chapter 2) in 1990–1991 show larger-than-expected temperature variability near the bottom. Pulses of warm water can be seen in several episodes, even at a site close to the grounding line. The CTD data from the site are consistent with measurements from Autosub in 2005, and much of the variability must stem from changes in the inflowing water masses, resulting from either seasonal or inter-annual variability in wind forcing.

During JR097 comprehensive hydrographic sections were made around the ice front, and Autosub was sent on a mission beneath the ice shelf, where it measured hydrographic conditions, as well as mapping out the base of the ice shelf above. The base of the ice shelf is surprisingly rough in places. The rough areas correspond to flow traces visible on satellite images of the ice shelf. While these features cover a relatively small fraction of the ice shelf area, the increased roughness may nevertheless be important for mixing near the base of the ice shelf. Comparing the water masses measured by Autosub with those measured around the ice front, the most likely sources of the water found farthest beneath the ice shelf were observed on the eastern side of the ice tongue, while much of the rest of the water observed is more similar to water masses found in the west. This is consistent with model results, which show the eastern sills as inflow regions for much of the year, with seasonal variability in the cavity circulation. However, seasonal variability in the properties of the water masses on the shelf may also account for some of these differences.

The modeling using POLAIR has provided results that are much closer to observations than previous efforts. In particular, lower melt rates are found, and circulation patterns outside the ice shelf are more realistic. These improvements can be attributed both to changes in boundary conditions and the chosen model domain, and to the climatology used to force the model along the boundaries. In addition, changes were made so atmospheric reanalysis data could be used to force the model, allowing more realistic multi-year runs. While there still are some problems with the model results, they are nevertheless an improvement, and provide useful information to help interpret data from the ice shelf.

Appendix A

Bathymetry around and beneath Fimbul Ice Shelf

During JR097, the Kongsberg Simrad EM120 multibeam echo sounder was running almost continuously, and collected data from a large part of the continental shelf west of the ice tongue. These data were cleaned during the cruise by Carol Pudsey and Martin Stott; however, all but one of the files containing their edits have not been located on the data tapes returned to BAS. Therefore I re-cleaned most of these files using MBedit (Caress and Chayes, 2003, 2005, accessed 2006), and recalculated the depths with sound velocity profiles from the CTD casts (using the station closest to the midpoint of each one-hour data file).

To extend these data beneath the ice shelf, I attempted to create a similar set of "multibeam" measurements using the four beam target ranges from the downward-looking ADCP, and deriving a target range from the sub-bottom profiler. Neither of these instruments was designed with this purpose in mind, and they are more limited than a dedicated multibeam echo sounder. The DW-216 transducer on the sub-bottom profiler clearly has a nominal beam width of 15–25° with a resolution of 6–10 cm (Edgetech, 2007, accessed 2009), so the footprint diameter at a range of 150 m is of order 60 m. In contrast, the beam width of a 150-kHz ADCP is around 4°, and the resolution can be up to 20 cm (Visbeck and Fischer, 1995).

To derive a target depth from the sub-bottom profiler data, the complete profiles of the signal envelope were loaded into Matlab with times corrected to match the other data from Autosub. Then a time-variable gain of $-40\,\mathrm{dB} + 170\,\mathrm{dB/s}$ was applied to each profile, and the first point beyond sample 3000 above a threshold of 40

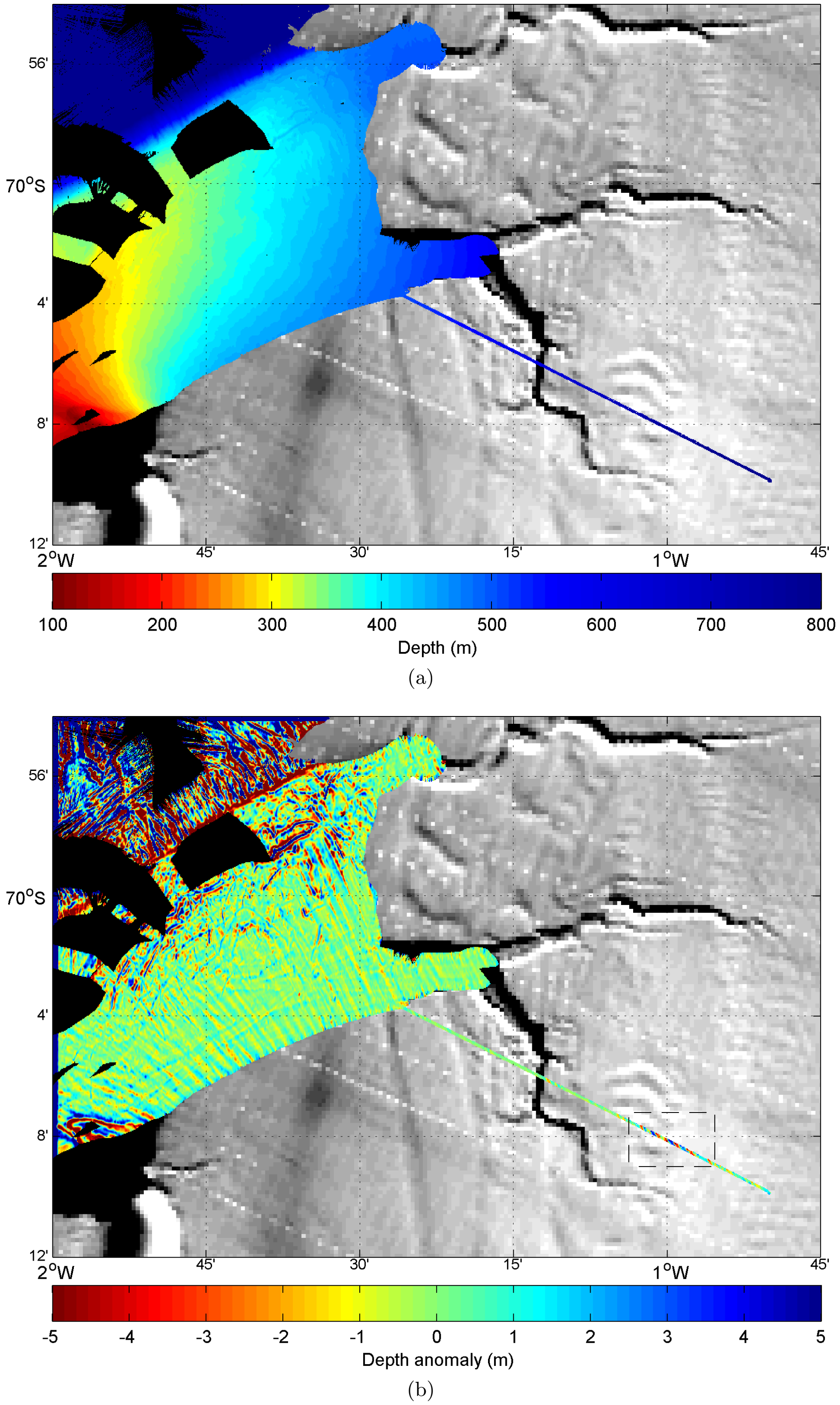

(a)

(b)

Figure A.1: (a) Bathymetry west of the ice tongue from the EM120 multibeam echo sounder (on the continental shelf) and Autosub (under the ice shelf). (b) High-pass filtered data, with the area from panel (c) shown with dashed black lines. Continued overleaf.

was flagged as the bottom. These were converted to depths using a constant speed of sound of 1447 m/s, and beam targets (in geographical coordinates) were calculated using the attitude data, corrected positions, and vehicle depths from the processed ADCP files.

To match the ADCP and sub-bottom profiler depths to the swath data, an offset of 7.75 m was applied to the ADCP data, and an offset of 4.75 m was applied to the sub-bottom profiler data. Then the soundings from all three instruments were gridded on a 50-meter grid. The resulting data are shown in Figure A.1a. While the initial plot does not show much detail, we can observe that the depth increases toward the ice tongue, with a minimum depth north of the Apollo Ice Rises. The continental shelf break is extremely sharp.

When a high-pass filter is applied to the data, a very different pattern emerges. In Figure A.1b a 400-m high-pass filter was used; this was done by repeating the gridding step in mbgrid, but using splines to extrapolate the data 12 grid cells (550 m) in each direction. This extrapolated dataset was then filtered with a two-way (symmetric) 8-cell wide boxcar filter across both dimensions, and these values were subtracted from the original data grid.

The resulting image shows a series of lineations going in a roughly NW/SE direction, apparently fanning out from the ice shelf. Several iceberg scours perpendicular to these lineations can also be seen on the shelf, as well as larger-amplitude gullies on the shelf break. These lineations probably show the direction of flow of the ice shelf during the last glacial maximum, when the ice shelf was grounded out to the shelf

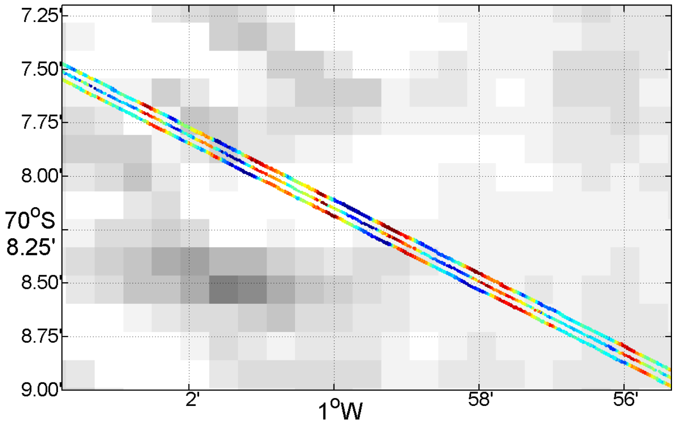

(c)

Figure A.1: (c) High-pass filtered data from Autosub in the area marked with dashed black lines in panel (b). Plotted using the same color scale as panel (b).

break. Beneath the ice shelf, the data from the ADCP and sub-bottom profiler also show these lineations, with slightly deeper features visible near 1° W. These are magnified in Figure A.1c. The direction of the features can also be clearly seen from these data. This indicates that if downward-looking multibeam data are not available from these sorts of missions beneath ice shelves in the future, this technique can be used to discern the orientation and amplitude of glacial scours.

Appendix B

Details of modeling work

This appendix gives more technical details of the model runs described in Chapter 4. The parameters used in the model runs are given in Table B.1 and the density coordinates are listed in Table B.2. A list of the various runs that have been performed (and their lengths) are outlined in Table B.4. The numbers in the first column are those of the spin-up run, which lasts ten years, starting in 1970, but using the forcing for 1980 repeated ten times. The numbering scheme for subsequent runs is shown in Table B.3. I have not referred to these experiment numbers in this thesis, but am including them here for completeness and for future reference. The main runs that are referred to in this thesis are runs 710 and 720. Table B.5 lists the modifications that were made to the model code over the course of this study.

Table B.1: Parameters used in model runs

Parameter	Value
Timesteps:	
Coupler timestep	3600 s
Baroclinic ocean timestep	600 s
Barotropic ocean timestep	27.27 s
Sea ice timestep	1800 s
Boundary conditions:	
North	Free slip (Neuman)
West	Cyclic
East	Cyclic
South	No slip (Dirichlet)

Table B.1: Parameters used in model runs (continued)

Parameter	Value
Boundary relaxation:	
Area	5 grid cells from northern, eastern, and western boundaries
Ocean temperature & salinity	10–30 days
Elevation (in tidal runs)	.01–.05 days (14:24–72:00 minutes)
Sea ice concentration	1–5 days
Drag coefficients:	
Air–Ocean & Air–Sea Ice	$1.5 * 10^{-3}$
Sea Ice–Ocean	$5.5 * 10^{-3}$
Ice Shelf–Ocean & Sea Bed–Ocean	$2.5 * 10^{-3}$
Within ocean (between layers)	$1.0 * 10^{-5}$
Albedos:	
Ocean	0.1
Sea Ice	0.7
Snow[1]	0.8
Melt pond bias	-0.3
Thickness constraints:	
Minimum ocean thickness	40 m
Maximum ocean depth	2500 m
Minimum mixed layer thickness	10 m
Misc. ocean parameters:	
Diapycnal fluxes	off
Background Viscosity Velocity[2]	$1 * 10^{-3}$ m/s
Smagorinsky Viscosity ratio	0.2
Layer Thickness Diffusion[2]	$1 * 10^{-3}$ m/s
Tracer Diffusion[2]	$1 * 10^{-3}$ m/s

---

[1] Actual albedo used depends on snow thickness

[2] The velocity is multiplied by the grid cell width to obtain the diffusivity.

Table B.1: Parameters used in model runs (continued)

Parameter	Value
Misc. atmosphere parameters:	
PBL angle[3]	25°
PBL slowdown factor[3]	0.8
Misc. sea ice parameters:	
Maximum number of iterations for pressure/velocity calculation	2000
Minimum concentration	0.001
Maximum concentration	1.0
Lead opening parameter[4]	1.5
Lead closing parameter[5]	3.0
Pressure decay coefficient[6]	20
Linear strength parameter[6]	27500 Pa
Minimum strain rate	$0.1 * 10^{-9}$
Supercooling required for frazil formation	0.2°C
Timescale for frazil formation	4.8 hours[7]

In LHS2006 runs with constant SSS, the restoration SSS is 34.3, with a timescale of 30 days. Varying SSS is 33.9 - 0.25 sin(month * 2 pi / 12) — peaking in September, with a minimum in March. Restoration SST is the surface freezing point calculated from the restoration SSS.

---

[3] The geostrophic wind (computed from sea-level pressure) is rotated by the PBL angle and multiplied by the slowdown factor to get the surface wind

[4] Causes thermodynamic melting to lead to lower ice concentration.

[5] Causes thermodynamic freezing to lead to higher ice concentration.

[6] Maximum pressure for rheology is calculated as strength parameter * exp(-decay coefficient * (1-ice concentration))

[7] Actually 0.2 days (4.8 hours) or 2 coupler timesteps (2 hours), whichever is greater. The heat required to remove the supercooling is converted into frazil over this time period.

Table B.2: Density coordinates used in model runs

Layer	Target density (kg/m^3)		
	LHS2006	New	6 layers
1	Variable (mixed layer)		
2	27.2000	27.2000	27.2500
3	27.2857	27.2857	27.4500
4	27.3714	27.3714	27.6500
5	27.4571	27.4571	27.8100
6	27.5214	27.5429	27.8500
7	27.5643	27.6286	—
8	27.6071	27.7143	—
9	27.6500	27.8000	—
10	27.6929	27.8071	—
11	27.7357	27.8143	—
12	27.7786	27.8214	—
13	27.8071	27.8286	—
14	27.8214	27.8357	—
15	27.8357	27.8429	—
16	27.8500	27.8500	—

Table B.3: Numbering scheme for model runs. X is the base number of the run (column 1 of Table B.4)

Run no.	NCEP forcing			LHS2006 forcing		
	Duration (years)	Output frequency	Years	Duration (years)	Output frequency	Years
X	10	monthly	1970–1979[a]	10	monthly	1970–1979
X+1	10	monthly	1980–1989	2	monthly	1980–1981
X+2	2	daily	1990–1991			
X+5	15[b]	monthly	1990–2004			

---

[a] using 1980 forcing repeated

[b] restarted from run X+1

Table B.4: Model runs in the FIMBUL_CYCLIC domain using POLAIR.

Run no.	σ coords.	Tides	Forcing	Run length
600	LHS2006	Off	NCEP & ice	10+10+2/15 years
610	LHS2006	On	NCEP & ice	10+10+2/15 years
620	LHS2006	Surface restoring	NCEP & ice	10+10+2/15 years
710	New	Off	NCEP & ice	10+10+2/15 years
720	New	On	NCEP & ice	10+10+2/15 years
950	6 layers	Off	NCEP & ice	10+10 years
960	6 layers	On	NCEP & ice	10+10 years
800	New	Off	Strong wind, constant SSS	10+2 years
805	New	On	Strong wind, constant SSS	10+2 years
810	New	Off	Strong wind, varying SSS	10+2 years
815	New	On	Strong wind, varying SSS	10+2 years
820	New	Off	Weak wind, constant SSS	10+2 years
825	New	On	Weak wind, constant SSS	10+2 years
830	New	Off	Weak wind, varying SSS	10+2 years
835	New	On	Weak wind, varying SSS	10+2 years
850–885	As 800–835, but with 6 layers			
900–935	As 800–835, but with AWI atlas used as initial conditions and for restoring on boundaries.			
840	New	Off	Alternating wind, varying SSS	15+9+16+7 years
845	New	Off	Alternating wind, constant SSS	15+10+15+7 years

Table B.5: Partial list of corrections, observations, and additions to the model code.

Description	Status
Switch for selecting Bleck code rather than Higdon causes uninitialized scratch fields to be used in calculations.	Not corrected
Masks for output of ocean variables were based on whether layers were inflated at the time of writing — not if they had been inflated over the previous accumulation time window. This caused errors in layer thicknesses, the longer the output time step. The fix was to mask accumulated fields (only) based on the accumulated thickness, rather than the instantaneous thickness.	Implemented Aug. 2006
Misplaced parentheses in the equations for the surface Ekman currents lead to incorrect (and significantly reduced) meridional currents. This affects the forcing that is transferred to the ice model.	Fixed Sept. 2006
The results are somewhat dependent on choice of time steps. Choosing a CFL fraction of 0.5 appears to give results close to those with CFL=0.25 while giving a significant savings in CPU time. However, using CFL=0.8 gives a 20% increase in melt rates.	Changed my namelists to use CFL=0.5 in Dec. 2006
A filter to remove isolated extrema from 2-D fields actually set both maxima and minima to use the maximum value of neighboring cells.	Fixed March 2007
Multi-year NCEP forcing was implemented in the model, with some inspiration from previous work by Malte Thoma. The next year's atmosphere forcing is generated at the first time step following 12:00 noon on Jan. 1st of each year. A compiler bug was discovered, causing the wrong year's data to be loaded on leap years! This was fixed with an update of the Intel Fortran Compiler (from v. 9.0.33 to 9.1.041)	Implemented March 2007; compiler updated Apr. 2007

Table B.5: Partial list of corrections, observations, and additions to the model code. (continued)

Description	Status
Velocities were previously averaged, without taking the varying thickness of layers into account; this meant that volume conservation is not very good in the output fields (but is correct in the calculations). The fix was to accumulate the flux through the sides of each grid cell, and then divide by the accumulated thickness to get the weighted average velocity. This is not 100% conservative because of the conversion from u/v-points to p-points on the C-grid, and the subsequent masking, but it's a large improvement.	Implemented May 2007
Wrote utilities to compare namelists between different runs and check the status of current runs. Ported the "pbstop" utility to the Hades cluster.	Written May 2007
Because some lines had been commented out (at an unidentified time in the past) fields of salinities and conductivities were used instead of surface velocities to force the baroclinic ocean model.	Fixed June 2007
Fixed implementation of periodic restart output, so restart files can be written at regular intervals. Implemented varying intervals (e.g. for months of varying length), and corrected the output so restarts are identical to continuous runs.	Fixed May–July 2007
Modified shell scripts to enable restarts if the model has crashed because a disk has filled up. Previously output files would have been deleted in this case. Also changed output on instability crash, to make diagnosing crashes easier.	Modified May–June & Oct. 2007
Found corrupt NCEP forcing files in repository; fixed and checked in files from 2002–2006.	Fixed June 2007

Table B.5: Partial list of corrections, observations, and additions to the model code. (continued)

Description	Status
Updated tide routines to include correct phase and nodal corrections. Implemented new elevation restoring scheme.	Modified July 2007
Ocean–sea ice and ocean–ice shelf drag coefficients were both present in code, but only the sea ice coefficient was used. This has been fixed so appropriate drag coefficients are used, depending on whether or not an ice shelf is present.	Fixed Aug. 2007
Detrainment occurred to the layer having the closest actual density to the mixed layer rather than the closest target density. This bug was identified by Adrian Jenkins. However, an additional bug occurs several places in the code if the difference between target densities is not constant.	Fixed Sept. 2007
Fixed cyclic boundary conditions, so they are applied consistently in all sub-models.	Fixed Sept. 2007
Paul Holland identified two severe bugs in the model code: before advection was performed, the velocity fields are smoothed. In a worst-case scenario, single-point channels have their transports reduced by 50%. In addition, the higher-order advection scheme (MPDATA) is not implemented correctly, and should be disabled until it is fixed.	Temporary modifications implemented Jan. 2008
Wrote Matlab routines to load Grads data files into Matlab and plot output from POLAIR.	Ongoing: 2006–present

References

AADI. Data storage unit 2990. Technical Report D174, Aanderaa Data Instruments, April 2010. URL `http://www.aadi.no/Aanderaa/Document%20Library/1/Data%20Sheets/Data%20Storage%20Unit%20%28DSU%29.pdf`.

Aanderaa Instruments. Operating manual, recording current meter models 7 & 8. Technical Report TD159, Aanderaa Instruments, September 1993.

Bleck, R. and L. T. Smith. A wind-driven isopycnic coordinate model of the north and equatorial Atlantic Ocean. 1. Model development and supporting experiments. *J. Geophys. Res.*, 95(C3):3273–3285, 1990. doi:10.1029/JC095iC03p03273.

Boyer, T. P., J. I. Antonov, H. E. Garcia, D. R. Johnson, R. A. Locarnini, A. V. Mishonov, M. T. Pitcher, O. K. Baranova, and I. V. Smolyar. World Ocean Database 2005. volume 60 of *NOAA Atlas NESDIS*. U. S. Government Printing Office, Washington, D. C., 2006. URL `http://www.nodc.noaa.gov/OC5/SELECT/dbsearch/dbsearch.html`. DVDs.

Broecker, W. S., S. L. Peacock, S. Walker, R. Weiss, E. Fahrbach, M. Schroeder, U. Mikolajewicz, C. Heinze, R. Key, T. H. Peng, and S. Rubin. How much deep water is formed in the Southern Ocean? *J. Geophys. Res.*, 103(C8):15833–15843, 1998. doi:10.1029/98JC00248.

Bu, X. and M. J. Warner. Solubility of chlorofluorocarbon-113 in water and seawater. *Deep-Sea Res. Part I*, 42(7):1151–1161, 1995. doi:10.1016/0967-0637(95)00052-8.

Budillon, G., G. Fusco, and G. Spezie. A study of surface heat fluxes in the Ross Sea Antarctica. *Antarct. Sci.*, 12(2):243–254, 2000. doi:10.1017/S0954102000000298.

Caress, D. W. and D. N. Chayes. MB-System version 5. Open source software distributed from the MBARI and LDEO websites, MBARI, 2003, 2005, accessed 2006. URL `http://www.ldeo.columbia.edu/res/pi/MB-System/`.

Carmack, E. C. Water characteristics of the Southern Ocean south of the Polar Front. In Angel, M., editor, *A Voyage of Discovery*, pages 15–41. Pergamon Press, Oxford, 1977.

Chavanne, C. P., K. J. Heywood, K. W. Nicholls, and I. Fer. Observations of the Antarctic Slope Undercurrent in the southeastern Weddell Sea. *Geophys. Res. Lett.*, 37 (13):L13601, 2010. doi:10.1029/2010GL043603.

Christian Michelsen Research. IFIX oceanographic sensor chain. Website, 2006. accessed Feb. 1 2006; now available from the Internet Archive at `http://web.archive.org/web/20061028141702/http://www.cmr.no/avd10/product-sensorkjede.shtml`.

Clough, J. W. and B. L. Hansen. Ross Ice Shelf Project. *Science*, 203(4379):433–434, 1979. doi:10.1126/science.203.4379.433.

Comiso, J. C. DMSP SSM/I daily and monthly polar gridded sea ice concentrations, 1987-1995. Technical report, National Snow and Ice Data Center, 1990, updated 1995. URL `http://nsidc.org/data/nsidc-0002.html`.

Daae, K. L., I. Fer, and E. P. Abrahamsen. Mixing on the continental slope of the southern Weddell Sea. *J. Geophys. Res.*, 114(C9):C09018, 2009. doi:10.1029/2008JC005259.

Danabasoglu, G. and J. C. McWilliams. Sensitivity of the global ocean circulation to parameterizations of meroscale tracer transports. *J. Climate*, 8(12):2967–2987, 1995. doi:10.1175/1520-0442(1995)008<2967:SOTGOC>2.0.CO;2.

Darelius, E. and A. K. Wåhlin. Downward flow of dense water leaning on a submarine ridge. *Deep-Sea Res. Part I*, 54(7):1173–1188, 2007. doi:10.1016/j.dsr.2007.04.007.

Darelius, E., L. H. Smedsrud, S. Østerhus, A. Foldvik, and T. Gammelsrød. Structure and variability of the Filchner overflow plume. *Tellus A*, 61(3):446–464, 2009. doi:10.1111/j.1600-0870.2009.00391.x.

Dinniman, M. S., J. M. Klinck, and Jr. Smith, W. O. Influence of sea ice cover and icebergs on circulation and water mass formation in a numerical circulation model of the Ross Sea, Antarctica. *J. Geophys. Res.*, 112(C11):C11013, 2007. doi:10.1029/2006JC004036.

Domack, E. W. Continental shelves and slopes. In Riffenburgh, B., editor, *Encyclopedia of the Antarctic*, pages 286–290. Routledge, 2007.

Dowdeswell, J. A. and N. F. McIntyre. The saturation of LANDSAT MSS detectors over large ice masses. *Int. J. Remote Sens.*, 7(1):151–164, 1986. doi:10.1080/01431168608954667.

Dowdeswell, J. A., J. Evans, R. I. Mugford, G. Griffiths, S. McPhail, N. Millard, P. Stevenson, M. A. Brandon, C. Banks, K. J. Heywood, M. R. Price, P. A. Dodd, A. Jenkins, K. W. Nicholls, D. Hayes, E. P. Abrahamsen, P. Tyler, B. Bett, D. Jones, P. Wadhams, J. P. Wilkinson, K. Stansfield, and S. Ackley. Autonomous underwater vehicles (AUVs) and investigations of the ice-ocean interface in Antarctic and Arctic waters. *J. Glaciol.*, 54(187):661–672, 2008. doi:10.3189/002214308786570773.

Dupont, T. K. and R. B. Alley. Assessment of the importance of ice-shelf buttressing to ice-sheet flow. *Geophys. Res. Lett.*, 32(4):L04503, 2005. doi:10.1029/2004GL022024.

Edgetech. 2400-DSS integrated deep sonar system, EdgeTech, 2007, accessed 2009. URL `http://www.edgetech.com/brochureMarine/2400-DSS%20Brochure%20082107.pdf`.

Egbert, G. D. and S. Y. Erofeeva. Efficient inverse modeling of barotropic ocean tides. *J. Atmos. Ocean. Technol.*, 19(2):183–204, 2002. doi:10.1175/1520-0426(2002)019<0183:EIMOBO>2.0.CO;2.

Erofeeva, S. Y., L. Padman, and G. D. Egbert. Assimilation of ship-mounted ADCP data for barotropic tides: Application to the Ross Sea. *J. Atmos. Ocean. Technol.*, 22(6):721–734, 2005. doi:10.1175/JTECH1735.1.

Fahnestock, M. A., T. A. Scambos, R. A. Bindschadler, and G. Kvaran. A millennium of variable ice flow recorded by the Ross Ice Shelf, Antarctica. *J. Glaciol.*, 46(155): 652–664, 2000. doi:10.3189/172756500781832693.

Fahrbach, E., G. Rohardt, and G. Krause. The Antarctic coastal current in the southeastern Weddell Sea. *Polar Biol.*, 12(2):171–182, 1992. doi:10.1007/BF00238257.

Fahrbach, E., R. G. Peterson, G. Rohardt, P. Schlosser, and R. Bayer. Suppression of bottom water formation in the southeastern Weddell Sea. *Deep-Sea Res. Part I*, 41 (2):389–411, 1994. doi:10.1016/0967-0637(94)90010-8.

Fiedler, E. K. Ocean–atmosphere heat fluxes at the Ronne Polynya, Antarctica. *Weather*, 65(1):16–21, 2010. doi:10.1002/wea.436.

Flato, G. M. and W. D. Hibler. Modeling pack ice as a cavitating fluid. *J. Phys. Oceanogr.*, 22(6):626–651, 1992. doi:10.1175/1520-0485(1992)022<0626:MPIAAC>2.0.CO;2.

Fofonoff, N. P. Some properties of sea water influencing the formation of Antarctic bottom water. *Deep-Sea Res.*, 4:32–35, 1956. doi:10.1016/0146-6313(56)90029-6.

Foldvik, A. and T. Kvinge. Conditional instability of sea water at the freezing point. *Deep-Sea Res.*, 21(3):169–174, 1974. doi:10.1016/0011-7471(74)90056-4.

Foldvik, A., T. Gammelsrød, and T. Tørresen. Circulation and water masses on the Southern Weddell Sea Shelf. In Jacobs, S. S., editor, *Oceanology of the Antarctic Continental Shelf*, volume 43 of *Antarct. Res. Ser.*, pages 5–20. American Geophysical Union, Washington, D.C., 1985a. doi:10.1029/AR043p0005.

Foldvik, A., T. Gammelsrød, and T. Tørresen. Physical oceanography studies in the Weddell Sea during the Norwegian Antarctic Research Expedition 1978/1979. *Polar Res.*, 3(2):195–207, 1985b. doi:10.1111/j.1751-8369.1985.tb00507.x.

Foldvik, A., T. Gammelsrød, S. Østerhus, E. Fahrbach, G. Rohardt, M. Schröder, K. W. Nicholls, L. Padman, and R. A. Woodgate. Ice shelf water overflow and bottom water formation in the southern Weddell Sea. *J. Geophys. Res.*, 109(C2): C02015, 2004. doi:10.1029/2003JC002008.

Foster, T. D. and E. C. Carmack. Frontal zone mixing and Antarctic Bottom Water formation in the southern Weddell Sea. *Deep-Sea Res.*, 23(4):301–317, 1976. doi:10.1016/0011-7471(76)90872-X.

Gade, H. G. Melting of ice in sea water: A primitive model with application to the Antarctic ice shelf and icebergs. *J. Phys. Oceanogr.*, 9(1):189–198, 1979. doi:10.1175/1520-0485(1979)009<0189:MOIISW>2.0.CO;2.

Gammelsrød, T., A. Foldvik, O. A. Nøst, Ø. Skagseth, L. G. Anderson, E. Fogelqvist, K. Olsson, T. Tanhua, E. P. Jones, and S. Østerhus. Distribution of water masses on the continental shelf in the southern Weddell Sea. In Johannesen, O. M., R. D. Muench, and J. E. Overland, editors, *The polar oceans and their role in shaping the global environment*, volume 85 of *Geophysical Monograph*, pages 159–176. American Geophysical Union, Washington DC, 1994. doi:10.1029/GM085p0159.

Gent, P. R. The Gent–McWilliams parameterization: 20/20 hindsight. *Ocean Modelling*, 39(1–2):2–9, 2011. doi:10.1016/j.ocemod.2010.08.002.

Gent, P. R. and J. C. McWilliams. Isopycnal mixing in ocean circulation models. *J. Phys. Oceanogr.*, 20(1):150–155, 1990. doi:10.1175/1520-0485(1990)020<0150:IMIOCM>2.0.CO;2.

Gill, A. E. Circulation and bottom water production in the Weddell Sea. *Deep-Sea Res.*, 20(2):111–140, 1973. doi:10.1016/0011-7471(73)90048-X.

Glasser, N. F., B. Kulessa, A. Luckman, D. Jansen, E. C. King, P. R. Sammonds, T. A. Scambos, and K. C. Jezek. Surface structure and stability of the Larsen C ice shelf, Antarctic Peninsula. *J. Glaciol.*, 55(191):400–410, 2009. doi:10.3189/002214309788816597.

Hellmer, H. H. Impact of Antarctic ice shelf basal melting on sea ice and deep ocean properties. *Geophys. Res. Lett.*, 31(10):L10307, 2004. doi:10.1029/2004GL019506.

Heywood, K. J., R. A. Locarnini, R. D. Frew, P. F. Dennis, and B. A. King. Transport and water masses of the Antarctic Slope Front system in the eastern Weddell Sea. In Jacobs, S. S. and R. F. Weiss, editors, *Ocean, Ice, and Atmosphere: Interactions at the Antarctic Continental Margin*, volume 75 of *Antarct. Res. Ser.*, pages 203–214. AGU, Washington D.C., 1998. doi:10.1029/AR075p0203.

Higdon, R. L. Implementation of a barotropic-baroclinic time splitting for isopycnic coordinate ocean modeling. *J. Comp. Phys.*, 148(2):579–604, 1999. doi:10.1006/jcph.1998.6130.

Holland, D. M. An impact of subgrid-scale ice-ocean dynamics on sea-ice cover. *J. Climate*, 14(7):1585–1601, 2001a. doi:10.1175/1520-0442(2001)014<1585:AIOSSI>2.0.CO;2.

Holland, D. M. Transient sea-ice polynya forced by oceanic flow variability. *Prog. Oceanogr.*, 48(4):403–460, 2001b. doi:10.1016/S0079-6611(01)00010-6.

Holland, D. M. and A. Jenkins. Modeling thermodynamic ice-ocean interactions at the base of an ice shelf. *J. Phys. Oceanogr.*, 29(8):1787–1800, 1999. doi:10.1175/1520-0485(1999)029<1787:MTIOIA>2.0.CO;2.

Holland, D. M. and A. Jenkins. Adaptation of an isopycnic coordinate ocean model for the study of circulation beneath ice shelves. *Mon. Weather Rev.*, 129(8):1905–1927, 2001. doi:10.1175/1520-0493(2001)129<1905:AOAICO>2.0.CO;2.

Holland, D. M., S. S. Jacobs, and A. Jenkins. Modelling the ocean circulation beneath the Ross Ice Shelf. *Antarct. Sci.*, 15(1):13–23, 2003. doi:10.1017/S0954102003001019.

Holland, P. R. and D. L. Feltham. Frazil dynamics and precipitation in a water column with depth-dependent supercooling. *J. Fluid Mech.*, 530:101–124, 2005. doi:10.1017/S002211200400285X.

Holland, P. R. and D. L. Feltham. The effects of rotation and ice shelf topography on frazil-laden ice shelf water plumes. *J. Phys. Oceanogr.*, 36(12):2312–2327, 2006. doi:10.1175/JPO2970.1.

Horwath, M., R. Dietrich, M. Baessler, U. Nixdorf, D. Steinhage, D. Fritzsche, V. Damm, and G. Reitmayr. Nivlisen, an Antarctic ice shelf in Dronning Maud Land: geodetic-glaciological results from a combined analysis of ice thickness, ice surface height and ice-flow observations. *J. Glaciol.*, 52(176):17–30, 2006. doi:10.3189/172756506781828953.

Hughes, T. J. The weak underbelly of the West Antarctic Ice-Sheet. *J. Glaciol.*, 27 (97):518–525, 1981.

Humbert, A. Numerical simulations of the ice flow dynamics of Fimbulisen. *FRISP Report*, 17, 2006. URL `http://folk.uib.no/ngfso/FRISP/Rep17/humbert05.pdf`.

Humbert, A. The temperature regime of Fimbulisen, Antarctica. *Ann. Glaciol.*, 51 (55):56–64, 2010. doi:10.3189/172756410791392673.

IOC, IHO, and BODC. Centenary Edition of the GEBCO Digital Atlas, published on CD-ROM on behalf of the Intergovernmental Oceanographic Commission and the

International Hydrographic Organization as part of the General Bathymetric Chart of the Oceans. CD-ROM, British Oceanographic Data Centre, 2003.

Jacobs, S. S., editor. *NBP09-01 cruise report*. 2009. URL `https://www.bodc.ac.uk/data/information_and_inventories/cruise_inventory/report/9460/`.

Jacobs, S. S., A. F. Amos, and P. M. Bruchhausen. Ross Sea oceanography and Antarctic Bottom Water formation. *Deep-Sea Res.*, 17(6):935–962, 1970. doi:10.1016/0011-7471(70)90046-X.

Jacobs, S. S., A. L. Gordon, and Jr. Ardai, A. L. Circulation and melting beneath the Ross Ice Shelf. *Science*, 203(4379):439–443, 1979. doi:10.1126/science.203.4379.439.

Jenkins, A. The impact of melting ice on ocean waters. *J. Phys. Oceanogr.*, 29(9): 2370–2381, 1999. doi:10.1175/1520-0485(1999)029<2370:TIOMIO>2.0.CO;2.

Jenkins, A. and D. M. Holland. A model study of ocean circulation beneath Filchner-Ronne Ice Shelf, Antarctica: Implications for bottom water formation. *Geophys. Res. Lett.*, 29(8):1193, 2002. doi:10.1029/2001GL014589.

Jenkins, A., D. M. Holland, K. W. Nicholls, M. Schröder, and S. Østerhus. Seasonal ventilation of the cavity beneath Filchner-Ronne Ice Shelf simulated with an isopycnic coordinate ocean model. *J. Geophys. Res.*, 109(C1):C01024, 2004. doi:10.1029/2001JC001086.

Jenkins, A., P. Dutrieux, S. S. Jacobs, S. D. McPhail, J. R. Perrett, A. T. Webb, and D. White. Observations beneath Pine Island Glacier in West Antarctica and implications for its retreat. *Nature Geosci.*, 3:468–472, 2010. doi:10.1038/ngeo890.

Jones, D. O. B., B. J. Bett, and P. A. Tyler. Depth-related changes to density, diversity and structure of benthic megafaunal assemblages in the Fimbul ice shelf region, Weddell Sea, Antarctica. *Polar Biol.*, 30(12):1579–1592, 2007. doi:10.1007/s00300-007-0319-6.

Joughin, I., E. Rignot, C. E. Rosanova, B. K. Lucchitta, and J. Bohlander. Timing of recent accelerations of Pine Island Glacier, Antarctica. *Geophys. Res. Lett.*, 30(13): 1706, 2003. doi:10.1029/2003GL017609.

Joughin, I., B. E. Smith, and D. M. Holland. Sensitivity of 21st century sea level to ocean-induced thinning of Pine Island Glacier, Antarctica. *Geophys. Res. Lett.*, 37 (20):L20502, 2010. doi:10.1029/2010GL044819.

Kalnay, E., M. Kanamitsu, R. Kistler, W. Collins, D. Deaven, L. Gandin, M. Iredell, S. Saha, G. White, J. Woollen, Y. Zhu, A. Leetmaa, B. Reynolds, M. Chelliah, W. Ebisuzaki, W. Higgins, J. Janowiak, K. C. Mo, C. Ropelewski, J. Wang, R. Jenne, and D. Joseph. The NCEP/NCAR 40-year reanalysis project. *Bull. Amer. Meteorol. Soc.*, 77(3):437–471, 1996. doi:10.1175/1520-0477(1996)077<0437:TNYRP>2.0.CO;2.

Khazendar, A. and A. Jenkins. A model of marine ice formation within Antarctic ice shelf rifts. *J. Geophys. Res.*, 108(C7):3235, 2003. doi:10.1029/2002JC001673.

King, M. A. and L. Padman. Accuracy assessment of ocean tide models around Antarctica. *Geophys. Res. Lett.*, 32(23):L23608, 2005. doi:10.1029/2005GL023901.

Klatt, O., W. Roether, M. Hoppema, K. Bulsiewicz, U. Fleischmann, C. Rodehacke, E. Fahrbach, R. F. Weiss, and J. L. Bullister. Repeated CFC sections at the Greenwich Meridian in the Weddell Sea. *J. Geophys. Res.*, 107(C4):3030, 2002. doi:10.1029/2000JC000731.

Klatt, O., E. Fahrbach, M. Hoppema, and G. Rohardt. The transport of the Weddell Gyre across the Prime Meridian. *Deep-Sea Res. Part II*, 52(3–4):513–528, 2005. doi:10.1016/j.dsr2.2004.12.015.

Large, W.G. and S.G. Yeager. Diurnal to decadal global forcing for ocean and sea-ice models: the data sets and flux climatologies. NCAR Technical Note TN-460+STR, National Center for Atmospheric Research, 2004.

Leach, H., V. Strass, and B. Cisewski. Modification by lateral mixing of the warm deep water entering the weddell sea in the maud rise region. *Ocean Dynamics*, 61 (1):51–68, 2011. doi:10.1007/s10236-010-0342-y.

Lemke, P., editor. *The Expedition Antarktis X/4 of RV "Polarstern" in 1992*, volume 140 of *Berichte zur Polarforschung*. AWI, Bremerhaven, 1994. hdl:10013/epic.10141.d001.

Lewis, E. L. and R. G. Perkin. Ice pumps and their rates. *J. Geophys. Res.*, 91(C10): 11756–11762, 1986. doi:10.1029/JC091iC10p11756.

Lythe, M. B. and D. G. Vaughan. BEDMAP: A new ice thickness and subglacial topographic model of Antarctica. *J. Geophys. Res.*, 106(B6):11335–11351, 2001. doi:10.1029/2000JB900449.

Makinson, K. and K. W. Nicholls. Modeling tidal currents beneath Filchner-Ronne Ice Shelf and on the adjacent continental shelf: their effect on mixing and transport. *J. Geophys. Res.*, 104(C6):13449–13465, 1999. doi:10.1029/1999JC900008.

Markus, T., C. Kottmeier, and E. Fahrbach. Ice formation in coastal polynyas in the Weddell Sea and their impact on oceanic salinity. In Jeffries, M. O., editor, *Antarctic Sea Ice: Physical Processes, Interactions and Variability*, volume 74 of *Antarct. Res. Ser.*, pages 273–292. American Geophysical Union, Washington, D.C., 1998. doi:10.1029/AR074p0273.

Melvold, K. and C. E. Rolstad. Subglacial topography of Jutulstraumen outlet glacier, East Antarctica, mapped from ground-penetrating radar, optical and interferometric synthetic aperture radar satellite data. *Norsk Geogr. Tidsskr.*, 54(4):169–181, 2000. doi:10.1080/002919500448549.

Melvold, K., J.O. Hagen, J. F. Pinglot, and N. Gundestrup. Large spatial variation in accumulation rate in Jutulstraumen ice stream, Dronning Maud Land, Antarctica. *Ann. Glaciol.*, 27:231–238, 1998.

Middleton, J. H., T. D. Foster, and A. Foldvik. Low-frequency currents and continental shelf waves in the Southern Weddell Sea. *J. Phys. Oceanogr.*, 12(7):618–634, 1982. doi:10.1175/1520-0485(1982)012<0618:LFCACS>2.0.CO;2.

Millero, F. J. Freezing point of sea water, eighth report of the Joint Panel of Oceanographic Tables and Standards, appendix 6. *UNESCO Tech. Pap. Mar. Sci.*, 28: 29–31, 1978.

Neethling, D. C. Snow accumulation on the Fimbul Ice Shelf, western Dronning Maud Land, Antarctica. In Gow, A. J., C. Keeler, C. C. Lanway, and W. F. Weeks, editors, *International Symposium on Antarctic Glaciological Exploration (ISAGE)*, pages 390–404, Cambridge, 1970. IASH86 and SCAR.

Nicholls, K. W., editor. *JR097 cruise report.* British Antarctic Survey, Cambridge, 2005. URL `http://www.antarctica.ac.uk/documents/cruise/JR097-CruiseReport.pdf`.

Nicholls, K. W. and K. Makinson. Ocean circulation beneath the western Ronne Ice Shelf, as derived from in situ measurements of water currents and properties. In Jacobs, S. S. and R. F. Weiss, editors, *Ocean, Ice, and Atmosphere: Interactions at the Antarctic Continental Margin*, volume 75 of *Antarct. Res. Ser.*, pages 301–318. American Geophysical Union, Washington, D.C., 1998. doi:10.1029/AR075p0301.

Nicholls, K. W. and S. Østerhus. Interannual variability and ventilation timescales in the ocean cavity beneath Filchner-Ronne Ice Shelf, Antarctica. *J. Geophys. Res.*, 109(C4):C04014, 2004. doi:10.1029/2003JC002149.

Nicholls, K. W., S. Østerhus, K. Makinson, and M. R. Johnson. Oceanographic conditions south of Berkner Island, beneath Filchner-Ronne Ice Shelf, Antarctica. *J. Geophys. Res.*, 106(C6):11481–11492, 2001. doi:10.1029/2000JC000350.

Nicholls, K. W., L. Padman, M. Schröder, R. A. Woodgate, A. Jenkins, and S. Østerhus. Water mass modification over the continental shelf north of Ronne Ice Shelf, Antarctica. *J. Geophys. Res.*, 108(C8):3260, 2003. doi:10.1029/2002JC001713.

Nicholls, K. W., E. P. Abrahamsen, J. J. H. Buck, P. A. Dodd, C. Goldblatt, G. Griffiths, K. J. Heywood, N. E. Hughes, A. Kaletzky, G. F. Lane-Serff, S. D. McPhail, N. W. Millard, K. I. C. Oliver, J. Perrett, M. R. Price, C. J. Pudsey, K. Saw, K. Stansfield, M. J. Stott, P. Wadhams, A. T. Webb, and J. P. Wilkinson. Measurements beneath an Antarctic ice shelf using an autonomous underwater vehicle. *Geophys. Res. Lett.*, 33(8):L08612, 2006. doi:10.1029/2006GL025998.

Nicholls, K. W., E. P. Abrahamsen, K. J. Heywood, K. Stansfield, and S. Østerhus. High-latitude oceanography using the Autosub autonomous underwater vehicle. *Limnol. Oceanogr.*, 53(5, part 2):2309–2320, 2008. doi:10.4319/lo.2008.53.5_part_2.2309.

Nicolaus, M. and K. Grosfeld. Ice–ocean interactions underneath the Antarctic ice shelf Ekströmisen. *Polarforschung*, 72(1):17–29, 2004. hdl:10013/epic.29880.d001.

Nøst, O. A. Measurements of ice thickness and seabed topography under the Fimbul Ice Shelf, Dronning Maud Land, Antarctica. *J. Geophys. Res.*, 109(C10):C10010, 2004. doi:10.1029/2004JC002277.

Nøst, O. A. and A. Foldvik. A model of ice-shelf ocean interaction with application to the Filcher-Ronne and Ross Ice Shelves. *J. Geophys. Res.*, 99(C7):14243–14254, 1994. doi:10.1029/94JC00769.

Nøst, O. A., E. Isaksson, T. Hattermann, H. Anschütz, K. Langley, and A. Sinisalo. Fimbul Ice Shelf — Top to Bottom: Glaciological and oceanographic results constrains mass balance. In *IPY Oslo Science Conference*, Oslo, June 2010a. URL `http://ipy-osc.no/abstract/379368`.

Nøst, O. A., L. H. Smedsrud, and T. Hattermann. Ocean properties below the Fimbul Ice Shelf. In *IPY Oslo Science Conference*, Oslo, June 2010b. URL `http://ipy-osc.no/abstract/381658`.

Nøst, O. A., M. Biuw, V. Tverberg, C. Lydersen, T. Hattermann, Q. Zhou, L. H. Smedsrud, and K. M. Kovacs. Eddy overturning of the Antarctic Slope Front controls glacial melting in the Eastern Weddell Sea. *J. Geophys. Res.*, 116(C11): C11014, 2011. doi:10.1029/2011JC006965.

Núñez-Riboni, I. and E. Fahrbach. An observation of the banded structure of the Antarctic Coastal Current at the prime meridian. *Polar Res.*, 29(3):322–329, 2010. doi:10.1111/j.1751-8369.2010.00166.x.

O'Dwyer, J., O. A. Nøst, T. I. Karlsen, J. Søreide, G. Jensen, A. Fransson, and V. Savinov. Oceanographic measurements near Fimbulisen ice shelf. In Winther, J.-G., editor, *Norwegian Antarctic Research Expedition 2000–2001*, volume 120 of *Norsk Polarinstitutt Rapportserie*, pages 38–42. Norwegian Polar Institute, Tromsø, 2002. URL `http://idtjeneste.nb.no/URN:NBN:no-bibsys_brage_7421`.

Olbers, D., V. Gouretski, G. Seiß, and J. Schröter. Hydrographic atlas of the Southern Ocean, Alfred Wegener Institut für Polar- und Meeresforschung, 1992. hdl:10013/epic.12913.

Orheim, O., J. O. Hagen, S. Østerhus, and A.C. Sætrang. Studies on, and underneath, the ice shelf Fimbulisen. In Orheim, O., editor, *Report of the Norwegian*

Antarctic Research Expedition (NARE) 1989/90, volume 113 of *Norsk Polarinstitutt Meddelelser*, pages 59–73. Norwegian Polar Institute, Tromsø, 1990. URL `http://idtjeneste.nb.no/URN:NBN:no-bibsys_brage_11570`.

Orsi, A. H., G. C. Johnson, and J. L. Bullister. Circulation, mixing, and production of Antarctic Bottom Water. *Prog. Oceanogr.*, 43:55–109, 1999. doi:10.1016/S0079-6611(99)00004-X.

Østerhus, S. and O. Orheim. Oceanographic and glaciologic investigations through Jutulgryta, Fimbulisen in the 1991/92 season. In Østerhus, S., editor, *Report of the Norwegian Antarctic Research Expedition (NARE) 1991/92*, volume 124 of *Norsk Polarinstitutt Meddelelser*, pages 21–28. Norwegian Polar Institute, Tromsø, 1994. URL `http://idtjeneste.nb.no/URN:NBN:no-bibsys_brage_11619`.

Padman, L., H. A. Fricker, R. Coleman, S. Howard, and S. Y. Erofeeva. A new tide model for the Antarctic ice shelves and seas. *Ann. Glaciol.*, 34:247–254, 2002. doi:10.3189/172756402781817752.

Price, M. R., K. H. Heywood, and K. W. Nicholls. Ice-shelf–ocean interactions at Fimbul Ice Shelf, Antarctica from oxygen isotope ratio measurements. *Ocean Sci.*, 4(1): 89–98, 2008. doi:10.5194/os-4-89-2008.

Rignot, E. and S. S. Jacobs. Rapid bottom melting widespread near Antarctic ice sheet grounding lines. *Science*, 296(5575):2020–2023, 2002. doi:10.1126/science.1070942.

Rignot, E. and R. H. Thomas. Mass balance of polar ice sheets. *Science*, 297(5586): 1502–1506, 2002. doi:10.1126/science.1073888.

Robertson, R., L. Padman, and G. D. Egbert. Tides in the Weddell Sea. In Jacobs, S. S. and R. F. Weiss, editors, *Ocean, Ice, and Atmosphere: Interactions at the Antarctic Continental Margin*, volume 75 of *Antarct. Res. Ser.*, pages 341–369. AGU, Washington D.C., 1998. doi:10.1029/AR075p0341.

Robin, G. de Q. Formation, flow, and disintegration of ice shelves. *J. Glaciol.*, 24(90): 259–271, 1979.

Robinson, N. J. An oceanographic study of the cavity beneath the McMurdo Ice Shelf, Antarctica. Master's thesis, Victoria University of Wellington, New Zealand, November 2004. hdl:10063/48.

Robinson, N. J., M. J. M. Williams, P. J. Barrett, and A. R. Pyne. Observations of flow and ice–ocean interactions beneath the McMurdo Ice Shelf, Antarctica. *J. Geophys. Res.*, 115(C3):C03025, 2010. doi:10.1029/2008JC005255.

Rotschky, G., P. Holmlund, E. Isaksson, R. Mulvaney, H. Oerter, M. R. Van Den Broeke, and J.-G. Winther. A new surface accumulation map for western Dronning Maud Land, Antarctica, from interpolation of point measurements. *J. Glaciol.*, 53(182):385–398, 2007. doi:10.3189/002214307783258459.

Schlosser, P., R. Bayer, A. Foldvik, T. Gammelsrød, G. Rohardt, and K. O. Munnich. Oxygen 18 and helium as tracers of ice shelf water and water ice interaction in the Weddell Sea. *J. Geophys. Res.*, 95(C3):3253–3263, 1990. doi:10.1029/JC095iC03p03253.

Schweitzer, P. N. Monthly average polar sea-ice concentration. Technical Report DDS-27, U. S. Geological Survey, 1995. URL `http://geochange.er.usgs.gov/data/sea_ice/`.

Scientific Committee on Antarctic Research. Antarctic digital database, SCAR & British Antarctic Survey, 2000. URL `http://www.add.scar.org`.

Shepherd, A., D. Wingham, and E. Rignot. Warm ocean is eroding West Antarctic Ice Sheet. *Geophys. Res. Lett.*, 31(23):L23402, 2004. doi:10.1029/2004GL021106.

Skogseth, R., A. D. Sandvik, and L. Asplin. Wind and tidal forcing on the meso-scale circulation in Storfjorden, Svalbard. *Cont. Shelf Res.*, 27(2):208–227, 2007. doi:10.1016/j.csr.2006.10.001.

Smedsrud, L. H. and A. Jenkins. Frazil ice formation in an ice shelf water plume. *J. Geophys. Res.*, 109(C3):C03025, 2004. doi:10.1029/2003JC001851.

Smedsrud, L. H., A. Jenkins, D. M. Holland, and O. A. Nøst. Modeling ocean processes below Fimbulisen, Antarctica. *J. Geophys. Res.*, 111(C1):C01007, 2006. doi:10.1029/2005JC002915.

Smethie, W. M. and S. S. Jacobs. Circulation and melting under the Ross Ice Shelf: estimates from evolving CFC, salinity and temperature fields in the Ross Sea. *Deep-Sea Res. Part I*, 52(6):959–978, 2005. doi:10.1016/j.dsr.2004.11.016.

Smethie, W. M., P. Schlosser, G. Bonisch, and T. S. Hopkins. Renewal and circulation of intermediate waters in the Canadian Basin observed on the SCICEX 96 cruise. *J. Geophys. Res.*, 105(C1):1105–1121, 2000. doi:10.1029/1999JC900233.

Stansfield, K. and G. F. Lane-Serff. Mixed layer deepening during an Antarctic gale. In *Autosub Under Ice Science Workshop*, the Open University, Milton Keynes, 2005.

Steinhage, D., U. Nixdorf, U. Meyer, and H. Miller. New maps of the ice thickness and subglacial topography in Dronning Maud Land, Antarctica, determined by means of radio-echo sounding. *Ann. Glaciol.*, 29:267–272, 1999. doi:10.3189/172756499781821409.

Strutt, J. E. Report of the inquiry into the loss of Autosub2 under the Fimbulisen. Technical Report 12, National Oceanography Centre Southampton, Southampton, 2006. URL `http://eprints.soton.ac.uk/41098/`.

Sun, S., R. Bleck, C. Rooth, J. Dukowicz, E. Chassignet, and P. Killworth. Inclusion of thermobaricity in isopycnic-coordinate ocean models. *J. Phys. Oceanogr.*, 29(10): 2719–2729, 1999. doi:10.1175/1520-0485(1999)029<2719:IOTIIC>2.0.CO;2.

Sverdrup, H. U. The currents off the coast of Queen Maud Land. *Norsk Geogr. Tidsskr.*, 14(1–4):239–249, 1953. doi:10.1080/00291955308542731.

Swithinbank, C., P. McClain, and P. Little. Drift tracks of Antarctic icebergs. *Polar Record*, 18(116):495–501, 1977. doi:10.1017/S0032247400000991.

Thoma, M., K. Grosfeld, and M. A. Lange. Impact of the Eastern Weddell Ice Shelves on water masses in the eastern Weddell Sea. *J. Geophys. Res.*, 111(C12):C12010, 2006. doi:10.1029/2005JC003212.

Visbeck, M. and J. Fischer. Sea surface conditions remotely sensed by upward-looking ADCPs. *J. Atmos. Ocean. Technol.*, 12(1):141–149, 1995. doi:10.1175/1520-0426(1995)012<0141:SSCRSB>2.0.CO;2.

Wåhlin, A. K. Downward channeling of dense water in topographic corrugations. *Deep-Sea Res. Part I*, 51(4):577–590, 2004. doi:10.1016/j.dsr.2003.11.002.

Walkden, G. J., K. J. Heywood, K. W. Nicholls, and P. Abrahamsen. Freshwater transport at Fimbulisen, Antarctica. *J. Geophys. Res.*, 114(C8):C08014, 2009. doi:10.1029/2008JC005028.

Walker, S. J., R. F. Weiss, and P. K. Salameh. Reconstructed histories of the annual mean atmospheric mole fractions for the halocarbons CFC-11, CFC-12, CFC-113, and carbon tetrachloride. *J. Geophys. Res.*, 105(C6):14285–14296, 2000. doi:10.1029/1999JC900273.

Warner, M. J. and R. F. Weiss. Solubilities of chlorofluorocarbon-11 and chlorofluorocarbon-12 in water and seawater. *Deep-Sea Res. Part A*, 32(12):1485–1497, 1985. doi:10.1016/0198-0149(85)90099-8.

Wingham, D. J., D. W. Wallis, and A. Shepherd. Spatial and temporal evolution of Pine Island Glacier thinning, 1995-2006. *Geophys. Res. Lett.*, 36(17):L17501, 2009. doi:10.1029/2009GL039126.